UNIVERSITÀ DEGLI STUDI DI PADOVA

Dipartimento di Fisica e Astronomia "Galileo Galilei"

Master Degree in Physics

Final Dissertation

Droplet-based optofluidics sensing of micro plastics in aqueous solutions

Thesis supervisor

Prof.ssa Cinzia Sada

Thesis co-supervisor

Dott. Giovanni Bragato

Candidate

Emanuele Perfetti

Academic Year 2022/2023

Contents

Introduction

The Greek word "plastikos", which means "suitable for moulding", suggests the reason why plastic has become an essential element of human life. The malleability or plasticity ensured by this material during production and processing allows plastics to be cast, pressed or extruded into a wide variety of shapes such as films, fibres, sheets, tubes, bottles and boxes, thus finding use in different industries. The *Plastics - the Facts 2022* report, presenting an analysis of the 2021 data related to plastics production, demand, conversion and end-of-life management in Europe, shows that, after a stagnation in 2020 due to the Covid-19 pandemic, the global plastics production increased to 390.7 million tonnes in 2021 with a rise of 4%, proving the strong and continuing demand for plastics [1].

Despite the current policy of good practice and awareness raising for the reuse and recycling of waste at least in the more developed countries, the presence of plastic accumulations in particular in our oceans is still large and extremely alarming with repercussions on tourism, shipping, fishing and aquaculture. Considering that the global cumulative production of plastic is expected to reach 34 billion metric tons by 2050 [2], the around 10,000 tons of plastic waste ending up nowadays in the surface waters or on the ocean floors is destined to increase [3]. The propensity of plastic products to absorb solar ultraviolet (UV) radiation and undergo photolytic, photo-oxidative, and thermo-oxidative reactions results in their degradation, which, though, is not complete. As a consequence, these synthetic polymers are fragmented into smaller and smaller debris of sub-millimetric dimension, called microplastics (MP) [4]. A study by the International Union for Conservation of Nature (IUCN) [5] identified synthetic textiles (35%), tires (28%) and city dust (24%) as the principal sources of microplastics, i.e. particles with a size ranging from 1 nm to 5 mm (according to GESAMP[1] [6]), in addition to fibres with a length between 3 nm and 15 mm and a length-to-diameter ratio that must be greater than 3, made mainly of polypropylene (PP), polystyrene (PS), polyamides (PA), polyethylene terephthalate (PET), polyvinyl chloride (PVC), polyacrylonitrile (PAN) and polymethylacrylate (PMA) [7].

The widely documented contamination of marine and freshwater environments by MPs represents a serious concern not only for aquatic organisms, which ingesting them undergo impaired reproduction, malnutrition, internal abrasions, and blockages [8], but also for human health, since the presence of microplastics has been revealed even in drinking water and foodstuff, such as fish and mussels, table salt, sugar, honey and milk [9]. Although ingestion is considered the principal pathway of exposure for humans, the detection of MPs in lung tissues confirms that inhalation is an other exposure route [10] as well as dermal absorption. Particles smaller than 100 nanometers can pass the dermal barrier exposing the immune system to toxic and dangerous chemicals, metals and pathogenic organisms. As a concecuence, microplastics can be considered highly risky because they have been demonstrated to be a courier for them at concentration several orders of magnitude higher respect to the levels in the surrounding environment.

The capability to identify and quantify MPs plays a fundamental role in the attempt to limit and reduce the impact they have, both on aquatic and terrestrial ecosystems, as fearsome pollution source. The separation, manipulation and characterization of microplastic particles, however, is a very challenging process due to their extremely small particle size, almost invisible to the naked eye, and complex chemical composition, cross-contamination and inhomogeneous nature. Indeed, the lack of standardized procedures of sampling, sample preparation, and detection represents the major obstacle to define

---

[1]Joint Group of Experts on the Scientific Aspects of Marine Environmental Protection

a validated methodology for MPs sorting [11]. Consequently, MPs measurements are performed with different protocols, depending on the research questions and objectives of the study. Nevertheless, all methods follow an analysis workflow based on three common steps: sample extraction, preliminary filtration (i.e. separation of microplastics from sediments) and isolation, identification [12].

Up to now, a variety of methodological approaches for the microplastics quantification is available, but their application depends on the dimension and shape of the particles and/or fibres to be investigated as well as on the processing aim. The most commonly used technique providing MPs visual sorting relies on their morphological classification and characterisation by light microscopy, assuming shape, degradation stage, and color as criteria. However, this approach underestimates small fragments (< 50 μm) and creates false positive results for long fibres (< 200 μm) [13] which, instead, are clearly identified by employing the scanning electron microscope (SEM), providing extremely clear, high-magnification images of microplastics up to 10-20 μm. The elemental chemical composition of polymers can be derived relating SEM measurements to EDS (energy dispersive X-ray spectroscopy) microanalysis, while, complete information on plastics molecular and bond structure is provided by advanced spectroscopy techniques such as FTIR and μFTIR, Raman and μRaman microscopy which allow the characterization of plastic particles with spatial resolution below 50 μm and 1 μm respectively [13]. To sort millemeter-size MPs, instead, some destructive analytical techniques - such as differential scanning calorimetry (DSC) and thermogravimetric analysis (TGA) - based on the measurements of changes in the polymers physical and chemical properties, are proposed in literature together with gas/liquid chromatography in combination with mass spectrometry [7].

It is worth noting that, at the moment, in the framework of plastic particles investigation, there are no effective techniques allowing the detection and investigation of sub-micrometric MPs, having a diameter ranging from 100 nm and 10 μm [14].

In this thesis project, a preliminary study has been performed on the development of new reliable procedures for the detection and identification of MP materials dispersed in water. The aim is to overcome the limitations of the technologies not suitable to characterize micrometer sized plastics and, in perspective, to provide cheap and compact MPs analysis tools that would be easily marketable *Plug-and-Play* devices.

The idea is to exploit an opto-microfluidic platform integrated in a lithium niobate (LiNbO$_3$, LN) substrate to generate and detect MilliQ water (dispersed phase) droplets dispersed in hexadecane (continuous phase), containing microplastics. The droplet generation is provided by setting up a laminar regime in a microfluidic circuit engraved on the LN substrate designed in a cross-junction configuration. The main microchannel, where droplets flow, cuts perpendicularly the device's optical stage composed by Ti-indiffused optical waveguides, realized on the same substrate in a Mach-Zehnder interferometer (MZI) configuration. A proper coupling of a laser beam (λ=532 nm) at the waveguide input allows a real time monitoring of the droplet, which is illuminated passing across the two MZ branches, triggering an optical transmission (OT) signal collected at the guide output. The performances of this Lab-On-a-Chip platform has been already tested with the mentioned opto-fluidic configuration in previous works ([15][16]) where, however, pure water droplets have been considered. In this study, instead, aqueous solutions with different concentrations of spherical plastic microparticles have been produced to generate sequences of droplets exploited then to evaluate and verify, also on the basis of the results obtained in [14], the ability of the chip to detect the content of such solutions. This analysis will be performed by the acquisition of a voltage signal describing the interaction between the droplets flowing in the channel and the laser coupled in the waveguide. The passage of a droplet in front of the MZ arms induces a transmission variation of the detected light which is then converted by a suitable electronics in a modulation of the voltage signal providing information on the dispersed phase content. This work is therefore a pioneering feasibility study that to be validated, required microplastics standards. As a consequence in order to have the better possible control on MPs dimension and composition, it has been decided to employ plastic microparticles of industrial manufacturing. In this work we mainly focused on polystyrene (PS), being one of the most diffused plastics both for industrial and everyday applications.

Table 1 reports the *Research Particles* (microParticles GmbH, Berlin, Germany) micro and nano

spheres used in this thesis project.

The experimental activity, as mentioned, was mainly centered around PS microparticles investigation, while PMMA spheres has been introduced only in a later test aimed to evaluate the device performance by considering plastic materials diverse from polystyrene. Each type of PS microplastic (in the following called: PS-340 nm, PS-617 nm, PS-1050 nm, PS-2500 nm and PMMA-2500 nm respectively) has been diluted in MilliQ solutions at different concentrations and adopted as dispersed phases to generate sequence of droplets. After defining a measurement and analysis protocol, the responses of the opto-microfluidic chip have been examined as a function both of the spheres diameter and of the MPs solutions concentration, investigating also the frequency content brought by a droplet signal. Experimental data have been explained in terms of a theoretical model. Finally some applications of the findings deduced by the data analysis are explored by setting different experimental conditions, such as the aforementioned test with the PMMA-2500 nm particles and the effect of the electric field exposition on the microplastics enriched droplets is presented as future perspective to increase the microplastics detectivity. In this case a new approach has been implemented that combines virtual electrodes written by suitable illumination of LN and the exploitation of its photovoltaic effect. The consequent building up of a local space-charge electric field designed to interact with the flowing droplets has been used to compare the water droplet response with and without microplastics.

Batch No.	Mean diameter (μm)	Standard-Deviation (μm)	W/V solids content
PS-R-KM303	0.34	0.01	5%
PS-R-B1155	0.617	0.02	5%
PS-R-KM612	1.05	0.03	10%
PS-R-KM595	2.5	0.03	10%
PMMA-R-L2835	2.5	0.06	10%

Table 1: Research Particles microspheres.

This thesis is composed of 5 chapters:

- in *Chapter 1* the mechanism generating droplets is discussed by resorting to the specific dynamic characterizing the geometry of the microfluidic circuit exploited. The optofluidic platform adopted is then introduced by presenting the main lithium niobate properties followed by a detailed description of the microchannels engraving technique employed and the realization process of the integrated MZI waveguides. The chapter ends with the experimental setup description;

- in *Chapter 2*, the initial discussion about the optical sensing capabilities provided by the platform will be discussed with special attention of the role of optical triggering that the platform allow to achieve. The optical response of the device in presence of MPs in a dispersed phase is therfore presented. Then, the measurement and analysis protocols are defined on the basis on preliminary trials. The brief section at the end of the chapter, instead, concerns the investigation of the frequency content of the OT signals acquired, based on power spectrum computation. The main results of this analysis are reported in *Appendix A*;

- in *Chapter 3* the experimental results obtained in this work are shown, with special care devote to evaluate the behaviour of the two analysis parameters defined in the analysis protocol in *Chapter 2*, as a function of the different solutions concentrations and diameter microparticles;

- *Chapter 4* proposes some hypothetical models fitting the experimental data describing the trends of the reference estimator parameter, defined in the analysis protocol, in terms of the MPs concentrations;

- in *Chapter 5* the findings derived in *Chapter 3* are initially exploited to discuss the results obtained by testing as dispersed phase the solutions with PMMA-2500 nm particles. Then, the same is done by mixing two solutions containing spheres of different dimension. Finally, at the end of the chapter, a space-charge electric field is induced in the lithium niobate substrate of

the optofluidic platform to explore its effects on MPs solutions, given the known results from a previous work [15] on pure water droplets.

<div align="right">

Chapter 1

</div>

Lithium niobate Lab-on-a-Chip platform: microfluidics and fabrication

---

In this chapter, a description of the working regime generating droplets is provided in section 1.1, by focusing on the dynamic of the exploited microfluidic circuit geometry (T-junction). In section 1.2 the opto-microfluidic platform employed to produce and detect droplets is presented. Since the device substrate is made of Lithium Niobate, the main properties of this material are briefly summarised and the fabrication process of a Ti in-diffused optical waveguide is therefore illustrated, with special attention to Mach Zehnder-based configuration of (MZI) waveguides exploited in this project. Finally, the process of integration of the microfluidic channels is discussed providing a description on how they are, engraved in the same substrate where the optical guides are realized. In this thesis a closed microfluidic geometry has been exploited as a consequence some details will be given the chip sealing procedure and LN functionalization. The experimental setup, instead, is depicted in section 1.3.

1.1 Microfluidics

Since the early 1960s, the society has witnessed the most rapid technological development of its history: the miniaturization of electronic devices. This progress in miniaturizing, down to sub-micrometric sizes, involved microelectronics as well as many other fields and several kinds of systems - such as mechanical, thermal or electromechanical - giving rise in the 1980s to a new field known as MEMS (*microelectro-mechanical systems*). Later, in the 1990s, this domain became extremely diversified with MEMS devices being fabricated for chemical, biological and biomedical applications, where fluid flows operating under unusual and unexplored conditions.
This led to a strong cross-fertilization among different fields paving the way to new disciplines such as microfluidics, i.e the science and engineering of systems in which fluid behavior differs from conventional flow theory primarily due to the small length scale of the system [17][18].
In particular, microfluidic technology processes or manipulates amounts of fluids ranging from μL to pL and relies on channels with dimensions of 10 to 500 μm [19] As a consequence, microfluidic channels operate in a laminar flow regime characterized by Reynolds number R_e such that

$$R_e = \frac{\rho d v}{\mu} < 100 \tag{1.1}$$

where ρ and v are the fluid's density and average velocity respectively, d is the characteristic linear dimension of the flow and μ the dynamic viscosity of the fluid [20].
Since a turbulent flow regime is never experienced (R_e<100 is well below $R_e \sim 2000$ that Reynolds demonstrated to be the value at or near which the transition from laminar to turbulent flow occurs [21]), under these conditions no mixing happens between different phases, making microfluidics to be suitable for producing controlled emulsions of two or more immiscible fluids. Consequently, the possibility to achieve dispersed phases in a continuous one has been seen as a high potential not only for applications in physics but also in the biological, chemistry and medical fields [22].

1.1.1   Droplet generation

The advantage provided by the laminar regime, combined with the high resolution and sensitivity in detections, low cost and fast analysis [19], is widely exploited in droplet microfluidics, where small volumes of fluids are produced with high precision manipulation.

Droplets of one phase (such as water), can be spontaneously produced if combined with another phase, that being immiscible, plays the role of a continuous phase (typically oil) where the droplets are dispersed in. For this reason normally we use the term of dispersed and continuous phases.

Several droplet generator configurations have been developed and studied since microfluidic's birth, with the common aim to ensure high reproducibility but also low dispersion in volume of droplets and high range of droplets frequency. In general, they can be divided in two main categories: active and passive. Both of them require external pumps to inject both phases in the microchannels. However, the former makes use of additional energy input - by applying additional forces either from electrical and magnetic fields or mechanical controls - to promote the interfacial instabilities needed for droplet generation (i.e droplet break-up). The latter, instead, acts without external actuation by relying on the circuit's geometry as well as the inertial and viscous properties of the fluids. [23]

This thesis' project exploited a passive droplet generator based on a T-junction geometry, one of the most employed because of its simplicity and ability to produce monodisperse droplets. It is directly obtained from the cross-junction configuration, where the continuous and dispersed phase fluids, labeled in the following with the subscription c and d respectively, flow in two microfluidic channels that cross each other orthogonally, shaping a crosswise junction. By closing one extremity of the secondary channel where the flux Q_d is injected, perpendicular to the main one where Q_c flows, the T-shape junction is formed.

The droplets production can differ varying the fluxes Q_d and Q_c, besides being strictly dependent on the physical parameters characterizing the fluids injected, such as the viscosity (μ_c,μ_c), the density (ρ_c,ρ_d) and the surface tension in combination with wettability properties, which affect the phases' contact angle with the channel surfaces.

In general, in order to explain the physical mechanisms of droplets generation, it has been demonstrated that regardless the working conditions, droplet shearing off is induced by the forces exerted by the continuous phase on the dispersed one entering the main channel. Therefore, depending on the competition of the capillary, viscous, and inertial forces involved, three different regimes can be distinguished [24][23][15]:

- **co-flow**: in this regime, fluids have similar viscosities; the interfacial tension between them is high as well as their wettability on channel surfaces. No droplets are formed since the two phases flow parallel to each other undisturbed with small velocities;

- **jetting**: this working condition occurs when the sum of viscous forces exerted by continuous-fluid and dispersed-fluid inertia overcomes interfacial tension forces; due to its intrinsic instability, this regime allows high frequency generation of small droplets but with a wider dispersion in the droplets volumes;

- **dripping**: unlike the jetting, this regime produces highly monodispersed droplets at a high but steady rate. The breakup of the droplet is dominated by the viscous force exerted by the continuous phase on the dispersed one and occurs at the junction and not after a small portion of the main channel, as in the previous case.

Among the regimes described in figure 1.1, the dripping, thanks to its stability, is the most studied regime and the one most devices are designed on.

In the case of cross-flowing geometries, including such as T-junctions, another regime is feasible, called *squeezing*. In this case the dispersed phase completely obstructs the main channel before that the break-up occurs, generating larger droplets that completely fill the main channel, as represented in figure 1.2. This behavior is led by a balance between the shear forces proportional to the continuous phase velocity, higher at the junction since the channel is partially obstructed by the dispersed phase, and the force driven by the pressure drop across the emerging droplet that acts differently on dripping and squeezing regime [24]. The latter is the working condition of choice for this work.
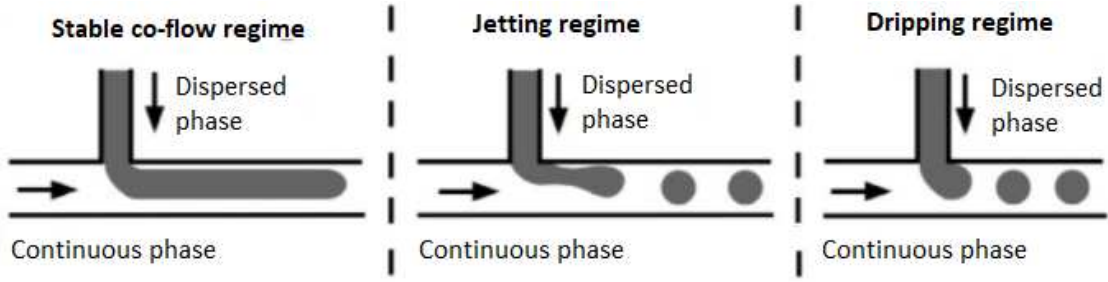
Figure 1.1: Sketch of the three typical working regimes in a T-junction droplet generator. Image taken from [15].

The first detailed theoretical model describing the production of droplets in the T-junction geometry
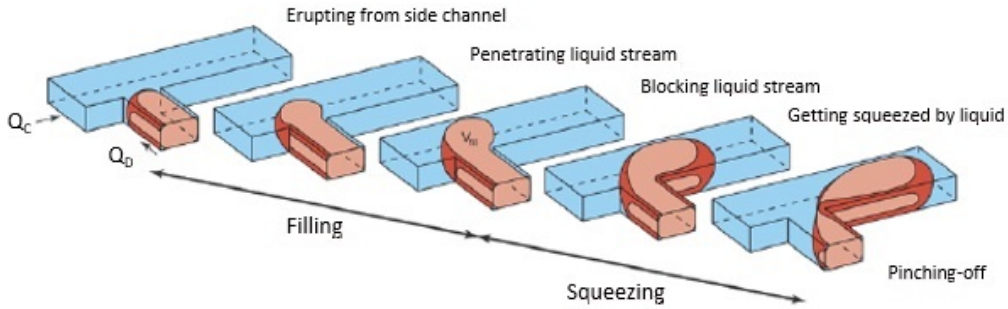

Figure 1.2: The different stages of droplet generation in a microfluidic circuit with a T-junction configuration operating in squeezing regime is depicted. The dispersed phase, emerging from the secondary channel, progressively fills the main channel as long as the continuous phase flowing in it is blocked; the pressure build-up squeezes the dispersed phase upstream, shrinking the neck until break-up of the droplet takes place [24]

.

was proposed by Garstecki et al. [25]. They identified, in addition to the shear stress force and the surface tension force analyzed by Throsen et al. [26], a third force acting on the dispersed phase tip growing at the fluid-fluid interface: the one arising from the pressure drop occurring at the junction. The balance among these forces is analytically described by the capillary number Ca, expressed by

$$Ca = \frac{\mu_c v_c}{\gamma}, \tag{1.2}$$

which Garstecki's work indicated as the parameter to distinguish between the dripping and squeezing regimes. At higher Ca values, the droplet break-up is dominated by the viscous shear forces, which are provided by the continuous phase viscosity μ_c and average velocity v_c and produce the small droplets distinctive of the dripping regime; on the contrary, at lower Ca, the capillary pressure given by the interfacial tension γ is dominant, promoting the formation of droplets that occupy the entire width of the channel, giving rise to the squeezing regime.

The same authors obtained also that the droplet's length is strictly dependent on the ratio of the volumetric rates of flow Q_d/Q_c, according to the law:

$$\frac{L}{w_c} = 1 + \alpha \frac{Q_d}{Q_c}, \tag{1.3}$$

where $\alpha \approx w_d/w_c$ is a constant of order one (since w_d and w_c are of the same order of magnitude) depending on the geometry of the T-junction, w_d and w_c are the widths of the secondary channel and main channel respectively.

However, the scaling law expressed by the equation 1.3 has proved to be valid only in squeezing working condition and in a small range of Ca values. An extension to an intermediate squeezing-to-dripping

regime was justified by the model proposed by Christopher and co-workers [27], which provides a detailed analytical evaluation of the forces involved in the droplet breakup. Their study was based on a spherical shape description of the dispersed phase tip emerging at the intersection of the channels, as illustrated in figure 1.3, where the sphere's radius b is connected to the dispersed phase by a neck of width s, equal to w_d.

The dynamic of the droplet process generation is governed by the relation

$$F_\sigma + F_\tau + F_P = 0 \tag{1.4}$$

where the balance among the capillary force F_σ, the drag force F_τ and the squeezing pressure one F_P, according to Christopher et. al hypothesis, determines the instant at which the break-up starts. These three forces are given by the expressions:

- **Capillary force**

$$F_\sigma \sim \left[-\sigma \left(\frac{2}{b} + \frac{2}{h} \right) + \sigma \left(\frac{1}{b} + \frac{2}{h} \right) \right] bh = -\sigma h \tag{1.5}$$

  that describes the difference between Laplace pressures $\sigma \left(\frac{1}{b} + \frac{2}{h} \right)$ and $-\sigma \left(\frac{2}{b} + \frac{2}{h} \right)$ acting respectively upstream and downstream with respect to the droplet (curvatures are approximated), multiplied by the projected area of the emerging interface bh, where h is the depth of the channel

- **Drag force**

$$F_\tau \sim \mu_c \frac{v_c}{w_c - b} bh \sim \mu_c \frac{Q_c}{(w_c - b)^2} b \tag{1.6}$$

  describing the force due to the viscous shear stress applied on the emerging dispersed phase droplet by the continuous phase flowing in the main channel. The shear rate is approximated by taking the ratio of the Q_c average velocity v_c, evaluated in the gap between the phases' interface and the wall of the channel, divided by the gap $(w_c - b)$;

- **Squeezing pressure force**

$$F_P \sim \Delta p_c bh \sim \mu_c \frac{v_c}{w_c - b} \frac{b}{w_c - b} bh \sim \mu_c \frac{Q_c b^2}{(w_c - b)^3} \tag{1.7}$$

  which is obtained from a lubrication analysis, as studied by Stone [28], for the pressure during the flow in a thin gap with aspect ratio $(w_c - b)/b$
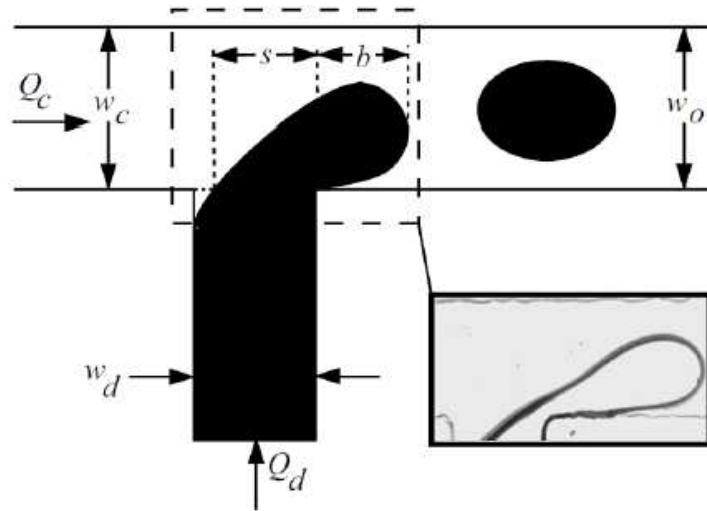

Figure 1.3: In this sketch the droplet emerges right before the break-up instant as discussed in the model proposed by Christopher and co-workers [27].

The shrinking process, leading to droplet generation, takes place when F_τ and F_P overcomes the capillary force F_σ opposing the droplet pinch-off. By comparing equation 1.4 to equations 1.5, 1.6

and 1.7 it is possible to derive the neck length b reached in the shrinking. It confines the Q_d volume connecting the dispersed phase still flowing in the inlet microchannel and the emerging droplet within Q_c.

The time required for the break up is estimated with the quantity $t_{squeeze} \approx w_d/v_c \approx w_d w_c h/Q_c$ that provides the additional contribution to the droplet's length due to the shrinking process when it is multiplied by the droplet speed $v_{growth} = Q_d/bh$ during its growth. Therefore, the total length of the generated droplet is given by the law:

$$\frac{L}{w_c} = \bar{b} + \frac{\Lambda}{\bar{b}} \frac{Q_d}{Q_c} \tag{1.8}$$

where $\bar{b} = b/w_c$ and $\Lambda = w_d/w_c$. As a consequence of the fact that the parameter Λ coincides with α parameter introduced by Garstecki and co-workers, the result obtained in 1.8 is traced back to equation 1.3 with $\bar{b} \to 1$. this condition is verified in the squeezing regime, since b is close to the channel width w_c during the droplet detachment.

In addition to the droplet length, another relevant quantity to be considered in the droplet generation process is the droplet production frequency. Christopher et al. derived it from experimental observations defining

$$\bar{f} = \frac{\mu_c w_c}{\gamma} f \propto Ca^{1-\delta}, \tag{1.9}$$

a power law valid for constant values of $\phi = Q_d/Q_c$, where $1 - \delta$ is experimentally determined to be 1.31 ± 0.03 and independent of the fluids viscosity as well as on the parameter Λ. The mentioned frequency $\bar{f}$ directly affects the rescaled volume $\bar{V} = V/w_c^2 h = \bar{L}\bar{b}$ of the single droplet, since it is provided by the power law

$$\bar{V} = \frac{\phi Ca}{\bar{f}} \propto Ca^\delta. \tag{1.10}$$

with $\delta = -0.31 \pm 0.03$.

In this work, the liquids used as continuous phase and dispersed phase are hexadecane[1] with SPAN® 80[2] surfactant at 3 % (w/w) (in the following: hexadecane) and Milli-Q® water (in the following: MilliQ), respectively. The latter is employed to produce the solutions containing plastic microparticles, which are also adopted as dispersed phases.

1.2 Opto-fluidics platform

In this thesis, the generation and detection of droplets have been provided by employing a Lab-on-a-Chip prototype entirely made on lithium niobate (LiNbO$_3$) crystals, able to detect the single droplet passage and estimate its size without the need of any imaging processing. It is an opto-microfluidics platform based on the coupling of a self-aligned integrated optical stage to a micrfluidic one. The optical stage is, made of an array of optical waveguides realized by exploiting the Titanium in-diffusion approach. The mirofluidic one, instead, is made of a cross-junction (or T-junction) geometry engraved in the same monolithic substrate by means of a mechanical micromachining process [29][30].

1.2.1 Lithium niobate

Lithium niobate (LiNbO$_3$) is a crystalline dielectric material with very interesting properties and characteristics that make possible to tailor its behavior for several different applications, incliuding microfluidics technology. This compound is colorless, chemically stable and insoluble in water and organic solvents. Due to its physical and optical properties, such as electro-optic effect, birefringence and piezoelectricity, lithium niobate is widely exploited in the fields of integrated optics and photonics as well as in the control of light beams through the generation of surface acoustic ultrasonic waves (SAW). As a consequence, it is ideal for the development of integrated waveguides, Pockels cells, electro-optical and acousto-optical modulators and switches, non-linear optical frequency converters and diffraction gratings, making this material very appealing in the telecommunication industry [31][32][33].

---

[1]Hexadecane: $CH_3(CH_2)_{14}CH_3$, CAS number: 544-76-3, molar mass MM = 226.44 g mol^{-1}, density ρ = 0.77 g cm^{-3}

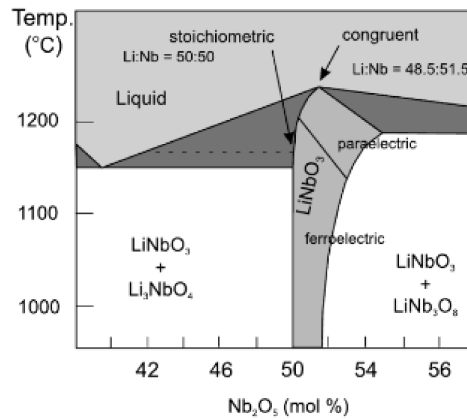[2]SPAN® 80: $C_{24}H_{44}O_6$, CAS number: 1338-43-8, molar mass MM = 428.62 g mol^{-1}

Figure 1.4: Phase diagram of pseudo-binary compound class Li_2O-Nb_2O_5, which lithium niobate $LiNbO_3$ belongs to. Sketch taken from [15].

Lithium niobate is a synthetic material grown by the Czochralski technique in crystals boules, in very homogeneous compositions and more that three inches (i.e 7.62 cm) in diameter [34]. This technique allows the growth of the crystal in the so called *congruent* composition, characterized by a lithium deficiency (48.45% of Li_2O) that provides a maximum in the liquid-solid curve, as illustrated in figure 1.4. Since the congruent composition is got when both the melt and the growing crystals have the same composition, in this case the highest uniformity in their chemical and physical properties can be achieved. For this reason, other growing techniques, such as stoichiometric crystals, are not considered since, in those cases, the composition of the melt and the crystal differ slightly during growth, making therefore the crystal non-uniform, especially along the growth axis [24]

Furthermore, it is worth mentioning that the ratio between the concentration of lithium and that of niobium affects several physical and optical properties, like the phase transition temperature, the photovoltaic effect and UV band absorption edge [31]. This is why congruent wafers are preferred and those available in commerce.
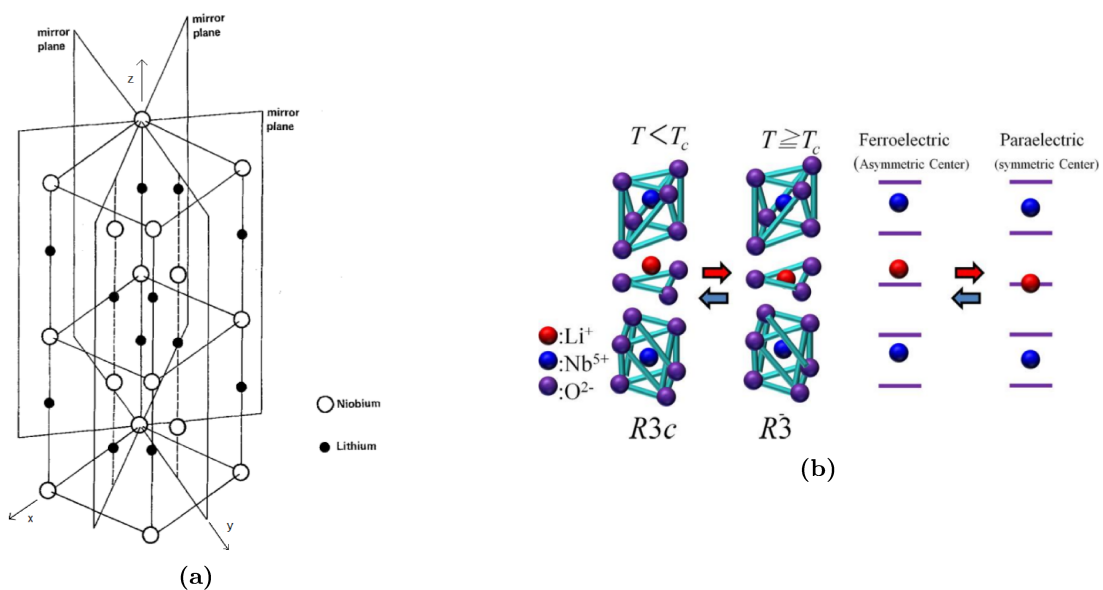
Crystal structure

(a)

(b)

Figure 1.5: In figure 1.5a the orthohexagonal cell of $LiNbO_3$ and symmetry planes are sketched [35], while figure 1.5b illustrates the lithium niobate structure in the ferroelectric and paraelectric phases with the horizontal purple segments representing the oxygen planes [36].

$LiNbO_3$ crystals are ferroelectric with a Curie temperature $T_C \approx 1140°C$.

At room temperature, the crystal exhibits a mirror symmetry about three planes that are 60° apart, whose intersection identifies a three-fold (120°) rotational symmetry axis. These symmetries properties classify $LiNbO_3$ as a member of the R3c space group. Since in the trigonal system the definition of the crystallographic axes is not unique, it is possible to consider three different conventional cells (hexagonal, rhombohedral or orthohexagonal) with the orthohexagonal one that is the most functioning in the description of this material physical properties by means the tensorial formalism.

The lithium niobate structure consists of oxygen atoms arranged in planar sheets in a slightly distorted hexagonal close-packed configuration. The octahedral interstices formed by oxygens disposition are one-third filled by lithium atoms, one third by niobium atoms and one third are vacant, following the order Li-Nb-vacancy along the z axis.

For temperatures above T_C, in the paraelectric phase where the material does not display polarity, lithium atoms lie in the oxygen planes filling the previous mentioned interstices, while niobium ions are located at the center of the octahedral structures.

At T<T_C instead, a spontaneous polarization is established by the shifts of the Li ions and Nb ions with respect the atoms' positions in the paraelectric phase. Both of them move along the z-axis, with the former by about 44pm from O planes and the latter by 27pm from the center of the octahedra. [35][15]

Physical properties

The main physical properties characterizing the $LiNbO_3$ are [35]:

- birefringence;

- electro-optic effect that produces a refractive index variation due to electric field application, inducing in the lithium niobate the Pockels and the Kerr effect;

- piezoelectricity, the effect inducing a polarization in response to an applied mechanical stress;

- pyroelectricity that generates a variation of the spontaneous polarization as a function of temperature;

- bulk photovoltaic effect, with the production of a current established by the electrons excited by uniform light illumination;

- photorefractive effect, which accounts for a refractive index change of a material when it is irradiated by a non-uniform light.

Below, the properties of major interest are set out in more detail.

Birefringence and optical properties

Lithium niobate is a transparent crystal, with high optical transmissivity in the range $\lambda = 350 \div 3500$ nm. Its characteristic birefringence is led by the crystallographic structure and symmetry properties which set the anisotropy of the permittivity tensor. The latter, in the orthohexanogal cell reference framework, is represented by a 3x3 matrix:

$$\bar{\epsilon} = \begin{bmatrix} \epsilon_{11} & 0 & 0 \\ 0 & \epsilon_{11} & 0 \\ 0 & 0 & \epsilon_{33} \end{bmatrix} \tag{1.11}$$

The ordinary refractive index, experienced by electromagnetic waves polarized in the direction parallel to the xy plane and perpendicular to the optical axis (z-axis), is expressed by the quantity $n_o = \sqrt{\epsilon_{11}/\epsilon_0}$ while the extraordinary one is defined by $n_e = \sqrt{\epsilon_{33}/\epsilon_0}$ and it is seen by light polarized parallel to the optical axis z and propagating in the xy plane.

These indices depend on light wavelength λ, on the composition of the crystal as well as on the presence of extrinsic impurities in the latter. In the wavelength range $\lambda = 400 \div 3000$nm and for a compositions of Li $C_{Li} = 47 \div 50$mol%, the generalized Sellmeier equation [37],

$$n_i^2 = \frac{A_{0,i} + A_{1,i}(50 - C_{Li})}{(\lambda_{0,i} - \lambda^{-2})} + A_{UV,i} - A_{IR,i}\lambda^2 \tag{1.12}$$

interpolates the mentioned refractive indices dependence, with an accuracy of 0.002 on n_i, $i = \{o, e\}$. Here, the intensity factors A express contributions to the refractive indices in the visible, the near visible and the near infrared region. In particular, the coefficients $A_{0,i}$ and $A_{1,i}$ account for the contribution given by Nb on Nb sites and Li sites respectively; A_{UV} and A_{IR}, instead, refer respectively to UV contribution due to plasmons and IR region contribution given by phonons.

In the case of λ=632.8 nm the ordinary and extraordinary refractive indices are:

$$\boldsymbol{n_o = 2.287 \pm 0.002 \qquad n_e = 2.203 \pm 0.002} \tag{1.13}$$

	Ordinary	Extraordinary
A_0	$4.5312 \cdot 10^{-5}$	$3.9466 \cdot 10^{-5}$
A_1	$2.7322 \cdot 10^{-5}$	$8.3140 \cdot 10^{-5}$
λ_0	223.219	218.203
A_{UV}	2.6613	2.6613
A_{IR}	$3.6340 \cdot 10^{-8}$	$3.0998 \cdot 10^{-8}$
n	**2.2866**	**2.2028**

Table 1.1: Fitted parameters for the Sellmeier equation 1.12 [37]. The refractive indices values are obtained for room temperature and a wavelength $\lambda = 632.8$ nm.

Pyroelectric effect

This effect, that influences material's spontaneous polarization according to the temperature, is present in lithium niobate in the ferroelectric phase and it is caused by the shifts of lithium and niobium ions with respect to the oxygen sheets.

It is possible to define the spontaneous variation of the polarization $\Delta\mathbf{P}$ as a linear function of the temperature variation $\Delta\mathbf{T}$, according to the expression:

$$\Delta P = p\Delta T \tag{1.14}$$

where $p = (0, 0, p_3)$, $p_3 = -4 \cdot 10^{-5}$ C m^{-2} K^{-1}, is the pyroelectric tensor whose form is because Li and Nb position shifts occur only along the z-axis. Note that the negative value of p_3 indicates, that upon cooling, the +z crystal face will become more positively charged as previously discussed.

Bulk photovoltaic effect

The bulk photovoltaic effect is manifested as a short circuit current induced by an uniform illumination of the material and arises typically in non-centrosymmetric crystals [31]. In the case of lithium niobate, it was discovered in 1974 by Glass and co-workers [38]. The photo-excited electrons are generated in the light's absorbing center by means of optical interactions; they move along a preferential direction with a current that can be expressed as:

$$j_{phv,i} = \beta_{ijk}e_j e_k^* I = \alpha k_{G,ijk}e_j e_k^* I \tag{1.15}$$

where β_{ijk} is the photovoltaic tensor, e_j and e_k are the unit vectors describing the polarization of the incident light, while I is the intensity. Introducing the light absorption coefficient α of the material, it is possible to evaluate the so-called Gauss coefficients tensor $k_{G,ijk} = \beta_{ijk}/\alpha$.

According to experimental values reported in the literature, the current mainly drifts in the direction parallel to the z-axis [39].

The combination of the electro-optic and photovoltaic effects generate the photorefractive phenomena. It relies on the presence of intrinsic or extrinsic impurities with two valence states. These impurities, in fact, add intermediate levels in-between the valence and conduction bands of the pure crystal acting both as donors or acceptors depending on their valence state. As a consequence, when a non-uniform light pattern interacts with the material, the induced non-uniform charge distribution in the crystal triggers an internal space-charge electric field, which modulates the material refractive index by means of the electro-optic effect.

In the case of lithium niobate, this double role of donor and acceptor state is fulfilled by the niobate antisite, since Nb^{4+} acts as a donor state while Nb^{5+} as an acceptor one. Furthermore, the photore-fractive effect is highly enhanced if the crystal is conveniently doped. The most common choice for doping is iron, which provides the two valence states Fe^{2+}, acting as a donor, and Fe^{3+}, acting as an acceptor.

1.2.2 Optical waveguides

Optical waveguides, also known as "dielectric" waveguides, are regions where light is confined and guided in optical circuits. They can come in a wide variety of shapes and sizes, and the miniaturization of such systems, in the form of thin film waveguides, has been proven to minimize the effects of ambient conditions and optical signals' loss of information, while possessing high power densities [24]. The simplest dielectric guide is the planar slab guide shown in figure 1.6, where a planar film of refractive index n_f is sandwiched between a substrate and a cover material with lower refractive indices n_s and n_c ($n_f > n_s \geq n_c$).
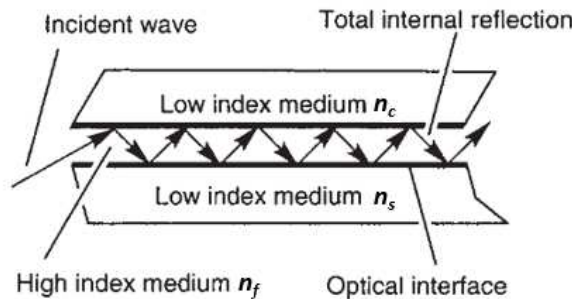

Figure 1.6: Sketch, taken from [40], of the propagation of a wave in a planar slab guide.

Typical differences between the indices of the film and the substrate range from 10^{-3} to 10^{-1}, and a typical film thickness is 1 μm. The light is confined by total internal reflection at the film-substrate and film-cover interfaces [41].

Lithium niobate, as before mentioned, is widely used not only in photonics but also in the telecommunication industry, being one of the best materials for the realization of optical waveguides thanks to its very low optical absorption (~ 0.1 dB/cm) in the typical employed telecom wavelengths ranging from 1260 nm to 1675 nm. Since the mid-70's, the most common integrated optical waveguide-based devices in lithium niobate crystals have been realized by exploiting Ti in-diffusion. For this reason, this technique is one of the most widespread and studied of all the LN technology. Although other techniques allow achieving higher optical confinement, Ti-in-diffusion is advantageous for the production of devices since it maintains the electro-optic properties of $LiNbO_3$ and ensures good light confinement on both ordinary and extraordinary refractive indices, allowing both TE and TM propagation modes [42].

State of the art

An overview of the other most employed fabrication techniques for integrated optical waveguides in lithium niobate is provided.

Proton exchange It is based on the substitution of lithium ions Li^+ in the crystal matrix with hydrogen ions H^+ by submerging the lithium niobate substrate in a liquid substance rich of hydrogen ions, usually benzoic or toluic acid, at high temperature (150÷400°C). This process is followed by a subsequent annealing in a controlled atmosphere, leading to the so-called Annealed Proton Exchange (APE) that ensures a better resistance of the material to optical damage.

The advantage of this technique is a high variation of the extraordinary refractive index of the order $\Delta n_e \sim 0.1$, with the ordinary one, on the contrary, that remains unchanged. The main drawback, instead, is that the proton exchange inflicts on the lithium niobate the loss of its electro-optical properties.

Ion implantation This method consists of bombarding ions at fixed energy and incidence angle with respect to the normal of the material surface. Depending on the ion energy - between a few MeV and more than 20 MeV [43] - and mass, both electronic excitations and nuclear interactions can contribute to the crystal modification and, as a consequence of this, to a refractive index change, up to an order of 0.1.

A subsequent thermal annealing process allows the recovery of the optical transparency characterizing the $LiNbO_3$ as well as the elimination of the damage induced by the ion implantation. If the high refractive index variation obtainable in both the ordinary and extraordinary directions represents a clear benefit, the cost and the dimension of the facilities to accelerate ions limit this technique's use.

Laser writing The main advantage of this approach is that three-dimensional waveguide structures can be fabricated in the bulk of a sample without any further processing. The writing of the optical guides on the substrate is realized either by exploiting the photorefractive effect of lithium niobate or by irreversible structural modification of the crystal. In both cases, the change of the refractive index is obtained by scanning the material with a focused laser beam. The difference between them lies in the applied processing parameters, like pulse energy and pulse duration. In particular, the technique based on the photorefractive effect relies on a continuous laser with tens of mW power. This leads to a considerable increase in n_e of the order of 10^{-3}. The re-design of the guide structure is allowed, if needed, thanks to the reversibility nature of photorefractivity which optofluidic applications take great advantage of.

The optical damage, instead, is generated by focusing a high-power femtoseconds laser on the region where the waveguide needs to be realized, which is scanned by moving the sample through a computer-controlled step motor [44]. In this way, varying the energy, it is possible either decrease only n_e or both n_e and n_o, with the latter case allowed at higher pulse energies.

Overall, the limited time durability of the waveguides is the main drawback of the laser writing technique.

Ridge waveguides This waveguide configuration provides high lateral optical confinement thanks to the significant refractive index contrast achieved between the lithium niobate and the protruding microscopic structures of a different material that are realized on the substrate to build the optical guides up. The fabrication of the latter is mainly obtained either by mechanical micromachining, exploiting micro-saws or micro-mills able to produce optical grade surfaces, or by chemical etching that, instead, relies on a mixture of HF and HNO_3 acting as an etchant and on the use of chromium (Cr) stripes as masks.

Ridge waveguides produce stronger scattering compared to diffused ones, resulting in a lower efficiency: this is due to their surface's roughness and to the presence of defects which, moreover, represent an obstacle to the sealing of an optofluidic platform, making this kind of waveguide not suitable for close optofluidic devices.

Titanium In-diffused waveguides

Titanium in-diffusion, as previously stated, is the most widely used and studied technique of waveguide fabrication in lithium niobate. It consists of a refractive index change by local doping of the substrate, achieved by Ti ions diffusion inside the material. This method, combined with standard photolithographic lift-off techniques and thermal treatments, is flexible and simple, allowing the realization of Ti-strips having a width ranging from 5 μm for visible spectral application to 8–10 μm for telecom wavelengths. Moreover, the versatility in the waveguides geometry design makes possible to obtain optical circuit configurations more complicated than a planar slab guide, keeping unaltered the flatness of the substrate. This feature, which is very useful in particular for optofluidic applications, has been exploited to realize the waveguide, integrated in the lithium niobate sample used as a substrate for the microfluidic platform, in a Mach-Zehnder interferometer (MZI) configuration.

Furthermore, the choice of this fabrication process was favored by: its high reproducibility, as already demonstrated by its commercial use in GHz optical modulators, the intention to produce a waveguide able to support only the fundamental mode, preserving the profile of the gaussian light beam propagating in it, and, last but not least, the availability of all the needed instruments and facilities required for its implementation even at a academic lab level (clean room, collimated UV lamp, magnetron sputtering, oven).

Fabrication

The main steps of the procedure to realize an optical waveguide on a lithium niobate substrate by Ti in-diffusion are the following:
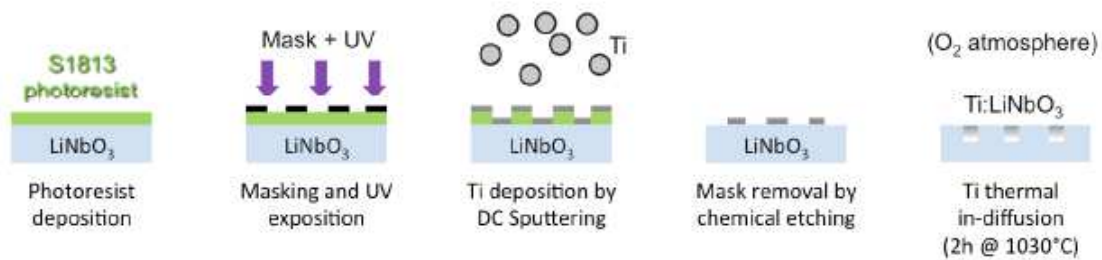

Figure 1.7: Sketch of the main steps of the Ti-indiffused channel waveguides fabrication

0) **Sample cutting** A commercial wafer of congruent lithium niobate (Crystal Technology) is cut orthogonally to the x-axes into samples 1 mm thickness of the desired size, by a means of a South Bay 540 cutting machine, equipped with a diamond-coated Cu-alloy blade. A graduated protractor is used to align the wafer along the crystallographic axes. Each sample, once it has undergone three separate 15-minute sonicating baths in soap and distilled water, isopropanol and acetone respectively, is labeled indicating on its x-surface the crystallographic axis orientation.

1) **Photolithography** This step is preceded by a further cleaning surface treatment, realized by generating a plasma discharge in oxygen atmosphere with medium-vacuum condition (P$\sim$ 0.6 mbar). After that, the surface of the sample is covered with a primer based on hexamethyl-disilizane (HDMS) to favor the adhesion of the photoresist to lithium niobate surface. The deposition of a positive photoresist [3] mask on the LiNbO$_3$ substrate, with the desired waveguide pattern (MZI geometry in this work), is then performed. The process is completed by exposing the sample with the mask to UV light and developing it with a bath in a basic solvent that removes the degraded photoresist.

2) **Titanium sputtering** The titanium film is deposited on the substrate coupled to the photoresist mask usually by exploiting sputtering techniques, heated evaporation, or E-beam methods. In

---

[3] The photoresist employed was the S1813 from the Microposit S1800 G2 series which is usually used in microlithography on silicon and showed to be suitable also on lithium niobate.

this thesis, a magnetron sputtering process is applied: the sample is placed in a vacuum chamber facing the titanium target, with the surface to be coated in the direction perpendicular to the trajectory followed by Ti-atoms that are removed after bombardment by the ions of the plasma. The latter is generated by setting a working pressure of $\sim 5 \cdot 10^{-3}$ mbar, achieved by employing a rotary vacuum and a turbomolecular pump and by a subsequent injection of Argon gas to feed the plasma. The discharge is provided by applying a ~ 300 V voltage difference between the chamber and the titanium target, with the presence of permanent magnets, which better confine the plasma in the proximity of the target, that increases the sputtering rate. At the end of the deposition process, a (41 ± 5) nm (SIMS measurements performed in [45]) Ti-layer on the surface of the sample is produced.

3) **Lift-off** The photoresist mask, as well as the titanium layer deposited over it, are removed by means of a lift-off process, a chemical etching technique. In particular, the sample is immersed in a SVC(TM)-14 photoresist stripper at 60°C.

4) **Annealing** The thermal diffusion in the lithium niobate of the Ti-stripes remained on the substrate after the lift-off is usually performed inside a furnace, in a wet oxygen atmosphere, at a temperature between 980 °C and 1050 °C, for a time ranging from 4 up to 12 hours, depending on the desired diffusion depth. This step, for the sample used in this thesis, occurred in a tubular furnace at a temperature of 1030 °C/h for 2h, adopting a heating and cooling rate of 300 °C/h and 400 °C/h respectively. In this way, excessive thermal stresses to the crystal are avoided. Moreover, to prevent contaminations, the sample is laid on a platinum foil before positioning it on a quartz rod in the furnace.

5) **Lapping and Polishing** The cutting of the LiNbO$_3$ wafer causes damages and defects on the lateral sample's surfaces. To remove them, and obtain thereby a roughness of the surfaces suitable for the presence of an optical waveguide, a lapping treatment followed by a polishing one is needed. Both are scraping processes that are performed by employing a rotating disk put in contact with the surface and wet with an aqueous solution containing alumina particles. The difference between the two procedures lies in the dimension of the latter: the lapping is applied by using 1-10 μm particles, while the polishing is realized with nanometric ones.

As far as the annealing treatment is concerned, it is worth focusing on the mechanism whereby titanium ions diffuse in the substrate.
The presence of a wet oxygen atmosphere plays a fundamental role: in fact, oxygen allows, at high temperatures, the oxidation of Ti layer in TiO$_2$ promoting the occupation of vacant Nb and Li sites by Ti^{4+} ions migrating inside the material; wet condition, on the other hand, avoids the out-diffusion of Li inside the TiO$_2$ layer, by neutralizing Li+ ions into a LiOH layer on the surface.
From an analytical point of view, the diffusion process can be described by the well-known Fick's law:

$$\frac{\partial C(x,t)}{\partial t} = \frac{\partial}{\partial x}\left(D \frac{\partial C(x,t)}{\partial x} \right) \tag{1.16}$$

where $C(x;t)$ is the concentration of titanium at time t along the direction of the Ti-ions diffusion x and D is the diffusion coefficient, which can be dependent on both dopant concentration and temperature.
The solution of equation 1.16 and, as a consequence, the waveguides diffusion profile inside the substrate, are strictly related to the level of dependence of D on the concentration. In case C was high an analytical solution is allowed only in specific configurations of boundary conditions. On the contrary, if the dopant concentration is almost constant, D results to be weakly dependent on C and can be estimated as an effective diffusion coefficient (at fixed temperature) as predicted by Arrhenius law $D = D_0 \exp(-Q_D/k_B T)$. In particular, the activation energy needed to titanium ions to start the diffusion is expressed by Q_D.
When C is constant, instead, the condition of independence of D provides two distinct solutions according to whether the titanium film is completely diffused in the substrate or not. The latter case is not treated, because the correspondent solution does not describe all the cases which involve real

diffusion. The former, on the contrary, depicts a situation that can be modeled by a titanium layer with negligible width since titanium ions, after a certain amount of time, are completely diffused in the LiNbO$_3$. Thereby, applying reflection boundary conditions at the interface between lithium niobate and the titanium layer, whose concentration can be considered to be $C(x; t = 0) \neq 0$ only if x = 0, the solution of the Fick's law [46] is:

$$C(x, t) = \frac{C_{tot}}{2(\pi D t)^2} \, e^{-\frac{x^2}{4Dt}}, \tag{1.17}$$

where $C_{tot}(t)$ is the total amount of titanium deposited on the surface film.

The diffusion process, thus, at the end of the thermal annealing, generates a semi-gaussian profile of the titanium concentration inside the sample, in the direction perpendicular to the substrate's interface. This leads to dielectric waveguide layers with graded refractive index profiles directly linked to $C(x, t)$ [47] and having the shape of an ellipsoid in the plane orthogonal to the light propagation direction (z crystallographic axes) that is squeezed in the proximity of the sample's surface.
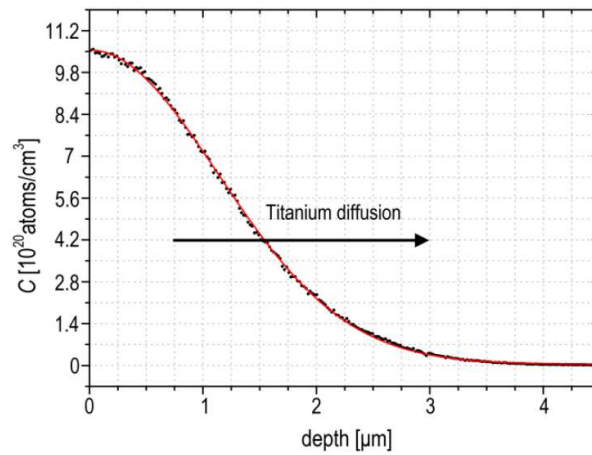

Figure 1.8: Graphical representation of the concentration profile of titanium inside a lithium niobate substrate in the direction orthogonal to the surface [45].

Figure 1.8 reports an example of the Ti-indiffused waveguides obtained at the Physics and Astronomy Department of the University of Padova, and used in this thesis. A semi-gaussian function can interpolate the Titanium profile inside lithium niobate: the illustrated graph has been obtained by a SIMS (Secondary Ions Mass Spectrometry) characterization allowing, through the fit, the estimation of the titanium penetration depth, which can be expressed as $\sigma = \sqrt{4Dt}$. As a consequence, by [45], analyzing the diffusion process for these Ti-indiffused waveguides not only with SIMS measurements but also with a RBS (Rutherford Back Scattering) characterization, the UNIPD group was able to estimate the diffusion coefficient $D = \sigma^2/2t$: for an initial deposited Ti layer of thickness 41±5 nm and thermal annealing of 2h at 1030°C/h, he obtained $D = 89 \pm 2$ nm^2 s^{-1}, corresponding to a $\sigma \approx 1.1$ μm and with a titanium concentration at the substrate surface $C_0 = (1.06 \pm 0.04) \cdot 10^{21}$ atoms $\cdot$ cm^{-3}.

Mach-Zehnder interferometer (MZI) waveguide configuration

Once known how titanium in-diffusion fabrication procedure has been carried out, as well as the physical and chemical mechanism that promotes the diffusion of Ti-ions in the lithium niobate substrate, the optical waveguide in MZI configuration adopted in this study is here presented.
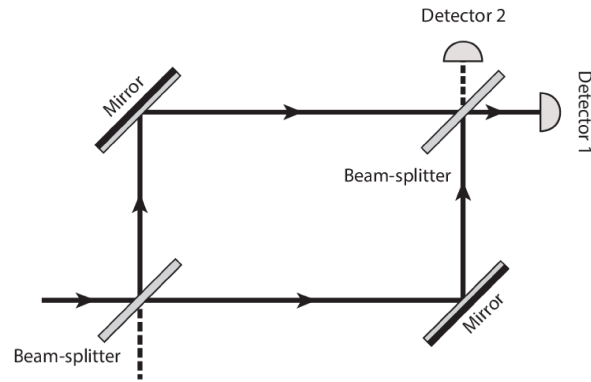
Figure 1.9: Scheme of a Mach-Zehnder interferometer: the incoming beam is divided by a beam-splitter in two distinct beams that, after traveling along the respective optical paths only once, are then recombined.

The well-known Mach-Zehnder interferometer (figure 1.9) is widely exploited to realize integrated devices in lithium niobate substrates, such as modulators and optical switches, for many electro-optical applications, including fiber-optic communication and signal processing. In the case of switches manufacturing, symmetric MZI geometry has been demonstrated to be very efficient due to their compact size, thermal stability and low-power operation [48]. In this kind of devices, the incoming signal is split in two beams, which experience phase difference passing through the interferometric arms. This phase difference is due to voltage variations across electrodes covering the arms that in turn, thanks to the LiNbO$_3$ electro-optic effect, changes refractive indices.

A representation of the MZI interferometer integrated in the employed waveguide structure is illustrated in figure 1.10. The Y junction at the input provides for the split of the incoming laser into two beams, which, following the respective S-shaped and straight sections, recombine at the output junction.

A deep analysis and investigation of the experimental validation of a waveguide MZI is presented in [49], where the optimization of the four main elements (y-junction, tapered transition, angle of the y-branch and bending loss) to be considered to limit as much as possible light losses is also discussed.
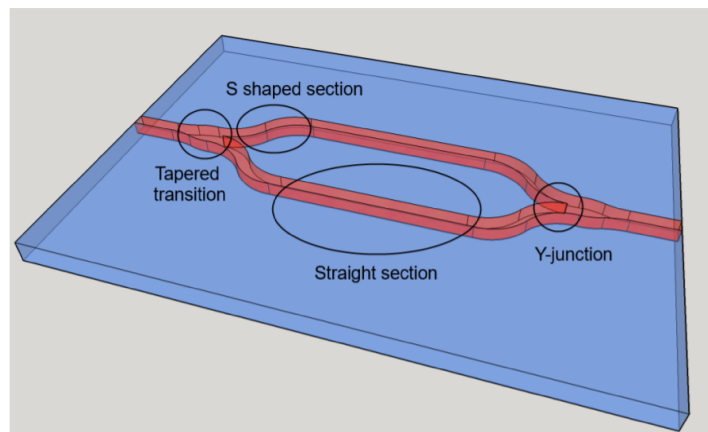

Figure 1.10: Example of Mach Zehnder interferometer integrated in a waveguide structure. Image taken from [49].

1.2.3 Microfluidic Channels Fabrication in Lithium Niobate

Fabrication of microchannels has always been a tough task: a number of methods are exploited to realize different types of microstructures, including both conventional and nonconventional fabrication techniques such as micro-milling, lithography, embossing processes and laser ablation processing. Moreover, depending on the applications of microchannel-based devices, different types of materials

are required: polymers and glass substrates are used in the biomedical and chemical field while silicon-based substrates and metallic ones are employed for electronics and mechanical engineering–related applications [50].

In the case of lithium niobate, the micromachining demands extra efforts due to the chemical resistance, anisotropy and high pyroelectricity of the crystal in addition to the low thickness of the sample. However, the aim of exploiting the superior physical and optical properties of LiNbO$_3$ leads to the development of several techniques for the realization of engraved structures on this substrate. According to the type of microstructure to be realized - microfluidic channels, optical waveguides, optoelectronics devices - and its characteristics (depth, width or roughness) the available fabrication techniques are: chemical etching, reactive ion etching, focused beam lithography, laser ablation and mechanical micromachining.

The microfluidic circuit with a cross-junction (or T-junction) geometry exploited in this thesis has been fabricated by means of mechanical micromachining. In order to justify this choice the other mentioned techniques are briefly presented, focusing on their advantages and drawbacks:

- **Chemical etching**: it is widely used on LiNbO$_3$ substrates for the realization of ridge waveguides, employing a HF solution to etch the surface. This technique allows obtaining optical quality surfaces but the etching rate is very low - till a few nm/min depending on the surface crystallographic orientation - making very long the fabrication of micrometrical structures.

- **Reactive ion etching**: RIE is based on a plasma discharge that, creating reactive free radicals and ions, etches the surface of a wafer. In the case of LiNbO$_3$, for instance, a mixture of CF$_4$, Ar and H$_2$ can be used to generate the plasma [51][52]. Although this technique allows to engrave microchannels with high-quality surface manufacturing, several hours are needed to fabricate a 100 μm deep channel.

- **Focused Beam Lithography**: FIB is mainly adopted for the fabrication of LN structures with a depth scale of tens of nanometers or below. It is a well-known method to produce LN-based nano-structures like photonic crystals and nanograting metasurfaces as well as to create smooth sidewalls on nanocrystalline microresonators. Due to the very low material removal rate, which has been proven to decrease as a function of aspect ratio of the milled structures [53], FBI allows to obtain an incredibly low roughness of the channel surface. In [54], for the first time a surface roughness of 0.9 nm was shown on LN surface for etching depth of 6.4 nm, with 7nm gold (Au) coating, paving the way to access the feasibility of FIB milling on ultra-shallow and ultra-smooth LN nano-structures.

- **Laser ablation**: thanks to its flexibility, this technique is widely exploited for designing structures with finely resolved features. In fact, it allows basically the realization of any kind of three-dimensional structure, finding applications both in microfluidics [55] and photonics [56], guaranteeing an accurate control of their dimensions. This leads to a easier microfluidic design allowing the realization of channels that can be shrunk or enlarged, tailoring their depth with no added complexity. The laser ablation on lithium niobate, which have been developed by using micro, nano and femtoseconds pulsed laser, often needs an additional HF bath to remove the imperfections on the treated surfaces. This drawback compromises any possible optofluidic coupling with microchannels, preventing the use of this method to the realization of microfluidic devices with integrated optical stages. In addition to this, a low removal rate characterizes structures' fabrication procedure.

Although the mentioned techniques demonstrated to be effective in several applications, their drawbacks make them not suitable for engraving microfluidic channels with dimensions of the order of 100 μm. These dimensional scales are only allowed by employing **mechanical micromachining**. This technique, commonly used to fabricate microstructures in silicon for optoelectronics devices, is successfully exploited also in optofluidic applications on lithium niobate, providing good quality channel surfaces in a short fabrication time. In particular, the optimal method for the realization of microchannels is microcutting [55], which is preferred to microdrilling and microengraving, that are other two exploited techniques for the milling of lithium niobate substrates.

As a consequence of the aforementioned considerations, after the fabrication of the MZI waveguide, the channels composing the microfluidic stage of the LiNbO$_3$ sample used in this work have been engraved on its surface, resorting to microcutting through a CNC saw. The procedure has been realized in collaboration with Femto-St Institute and the University of Franche-Comté in Besançon. In this case a DISCO DAD 3350 precision saw (Disco Corporation, Tokyo, Japan), equipped with a polymeric blade of diameter 56 mm and thickness 200 μm coated with diamond particles, has been exploited at a rotation speed of 10000 rpm and a cutting speed of 0.2 mm/s. The latter parameters were previously optimized in order to get the lowest roughness on the side faces.

The channels obtained have been analyzed with both optical microscopy and atomic force microscope (AFM), to evaluate that the surface and edges quality was appropriate for a waveguide optical coupling. The measurements were performed by means of a Veeco CP-II atomic force microscope (AFM, Camarillo, CA, USA), estimating the roughness of the lateral and bottom surface of the channel by averaging the results derived sampling more than five $10x10\,\mu m$ areas. The values reported in table 1.2 show a marked improvement with respect to the laser ablation technique, since previous analysis showed a roughness of R = 65 ± 4 nm for the lateral surfaces.

Surface	Average roughness (nm)
Bottom	23 ± 7 nm
Lateral	8.5 ± 0.9 nm

Table 1.2: Average roughness of the bottom and lateral surfaces of the microchannel walls.

The bottom surface, as illustrated in the AFM analysis in figure 1.11a and in the micrographs in figure 1.12, displays along the channel length a striping pattern generated by the blade of the saw during the fabrication. The width and the depth of these strips have a dimensional scale of hundreds of micrometers, representing a "macroscopic" roughness that is much greater than the average ones in table 1.2. Nevertheless, this is not a problem neither for the production of microfluidic droplets nor for the coupling of the waveguide with the channel for two main reasons:

- between the droplet and the bottom surface of the channel there is always a continuous phase thin film of hundreds of nanometers thick that avoids the impact of the defects on the droplet shape;

- for the guide-channel coupling what matters is the roughness of the lateral walls, which are not affected by the aforementioned pattern (figure 1.11b) since they are further smoothed by the blade rubbing on their surfaces.
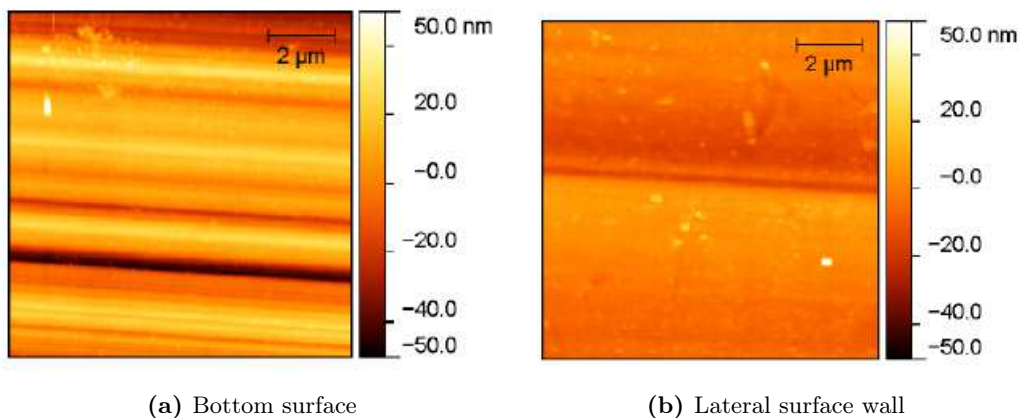

(a) Bottom surface   (b) Lateral surface wall

Figure 1.11: 10x10 μm^2 AFM images of the bottom surface (figure 1.11a) and lateral wall surface (figure 1.11b) of the microchannel analyzed.

<div align="center">(a)   (b)</div>
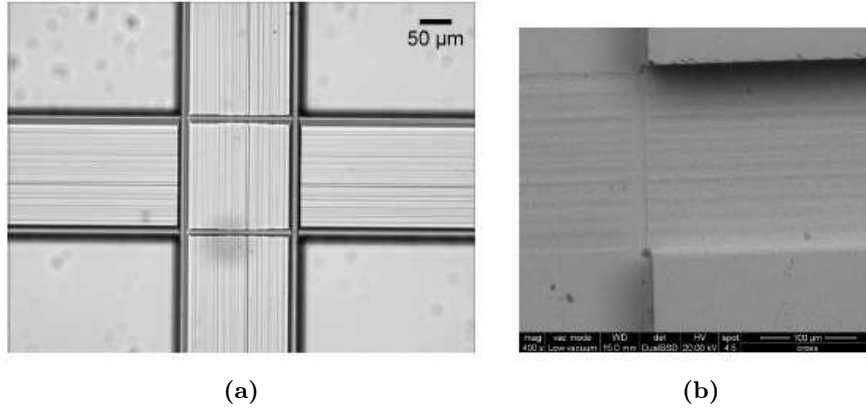
Figure 1.12: Micrographs of the bottom surface of the microfluidic channels realized by an optical microscope (figure 1.12a) and a Scanning Electron Microscope (SEM) (figure 1.12b).

The extremely low roughness of the lateral surfaces of the channel, therefore, proves that microcutting is able to achieve a precise enough cut to allow an effective waveguide coupling for the studied opto-fluidic applications.

Engraved microchannels, realized on the LiNbO$_3$ sample adopted, display an average width of $w_c = 213 \pm 1$ μm and height h $= 108 \pm 1$ μm: these results correspond to the average of 10 different profilometry measurements performed 6 along the main channel and 4 in the shorter one, by means of a surface profilometer P-10 (KLA Tencor, California, USA).
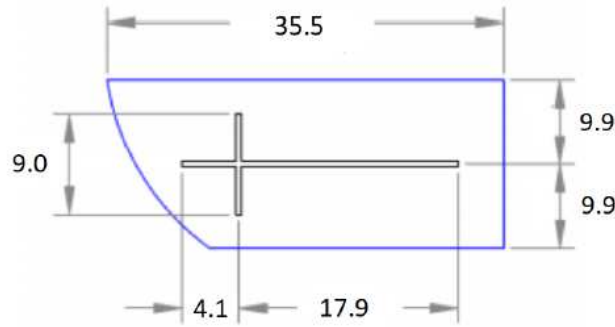

Figure 1.13: Sketch, taken from [15], of the lithium niobate sample employed in this experimental activity. The lengths reported are expressed in mm.

1.2.4 Chip sealing

Once the optical waveguide and the microfluidic circuit have been realized, the lithium niobate substrate needs to be sealed with a top cover (a glass one in this case) in order to get a solid and compact chip.

Before realizing the bonding with the LiNbO$_3$ substrate, the cover is cut with the same sample's dimension by using the available South Bay 540 cutting machine. Then, by means of a sandblaster, 4 holes are drilled on it: they match the extremities of the cross formed by the microchannels and represent inlets and outlets of the microfluidic junction which are completed gluing 4 Masterflex silicone tubing as connectors.

After that, the following bonding procedure occurs:

- both the sample and the top cover are accurately cleaned applying in sequence acetone, ethanol and isopropanol;

- after properly placing the glass cover on the substrate, the two are kept in tight contact by means of external compressive load, which is provided by two point clamps in this case;

- by using a syringe needle, the liquid photopolymer Norland Optical Adhesive 68 (NOA68,Norland Products Incorporation)[4] is placed all around the contact perimeter of the sample-cover sandwich. Via capillary-pressure driven flow, the glue fills the thin air gap between the two materials stucking its diffusion due to surface tension in proximity of the channel edges, having the NOA layer a few micrometers thickness. The process takes up to 24 hours. An analog bonding procedure is presented in [57].

- since NOA resine becomes solid if exposed to UV radiations, once it has completely substituted air in the thin gap, the bonding is completed by cross-linking the glue using a UV lamp, obtaining the final compact chip.
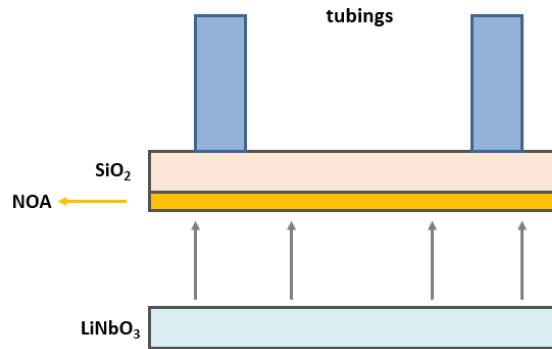

Figure 1.14: Schematic representation of the sealing procedure performed through NOA resine.

1.2.5 Functionalization of the lithium niobate

As described in 1.1.1, the generation of the droplets occurs by the interaction of immiscible continuous and dispersed phases, such as hexadecane and water. The functionalization of the sample is a process that aims to make hydrophobic the surfaces of the lateral walls of the microfluidic channels, including, in this case, also the upper surface created by the glass top-cover.
In droplet microfluidics circuits, in fact, it is always needed the presence of a thin layer of continuous phase between the droplet and the channel's walls, so that the dispersed phase never gets in contact with the latter. This yields more control on droplets production as well as on their shape and uniformity[58].
In absence of functionalization, wettability measurements with water droplets provides an average water contact angle with the lithium niobate surfaces of $62 \pm 1°$, proving that the moderate hydrophobicity of $LiNbO_3$, which instead is highly oleophilic having a contact angle with hexadecane always less than $10°$, is not enough for the generation of droplets.
Therefore, in order to increase water contact angle, the same method proposed in [39] is employed. The procedure provides for the fluxing, within the microchannels for 20 minutes, of a solution of octadecyltrichlorosilane (OTS) dissolved in toluene at a concentration of $100 \ \mu M$. OTS is a molecule with a long hydrophobic carbon chain and a polar head region made of $SiCl_3$ group, which binds to lithium niobate oxygen atoms forming siloxy-niobate (-Si-O-Nb-) bonds [59]. In this way, a self-assembled monolayer is produced on the surfaces of the channels making them hydrophobic [60]. In addition to this, thanks to the functionalization, also the wall of the glass cover becomes hydrophobic [61].
Finally, eventual residuals of OTS-toluene solution are cleaned by flowing pure toluene in the microfluidic circuit for 5 minutes and then by heating the device at 80 °C for 60 minutes.
After OTS treatment, the average contact angle water-lithium niobate is $101 \pm 1°$; in figure 1.15 a comparison of the droplet production in the microfluidic channel before and after the functionalization is illustrated. The improvement is evident.

---

[4]This resine is characterized by a high chemical resistance to the most common solvents and by a high viscosity; the latter feature avoids an eventual drop inside microchannels, making it an ideal choice for this application
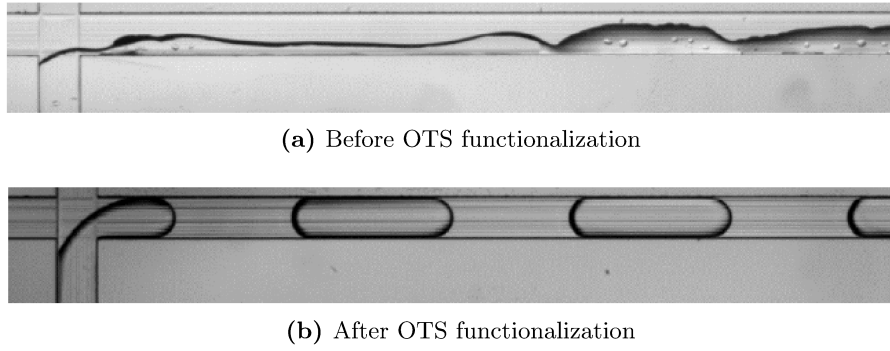
(a) Before OTS functionalization

(b) After OTS functionalization

Figure 1.15: Difference between droplets production efficiency before (1.15a) and after (1.15b) the OTS treatment applied to the microchannels, designed with a cross-junction geometry [39][15].

1.3   Experimental setup

The experimental setup adopted in this study can be split up in two main components: the microfluidic system, devoted to the injection of the continuous and dispersed phase in the optofluidic platform in order to generate the droplets, and the optical one, which provides for the coupling of a laser with the MZI waveguide and the subsequent collection of the the outgoing signal from the interferometer.
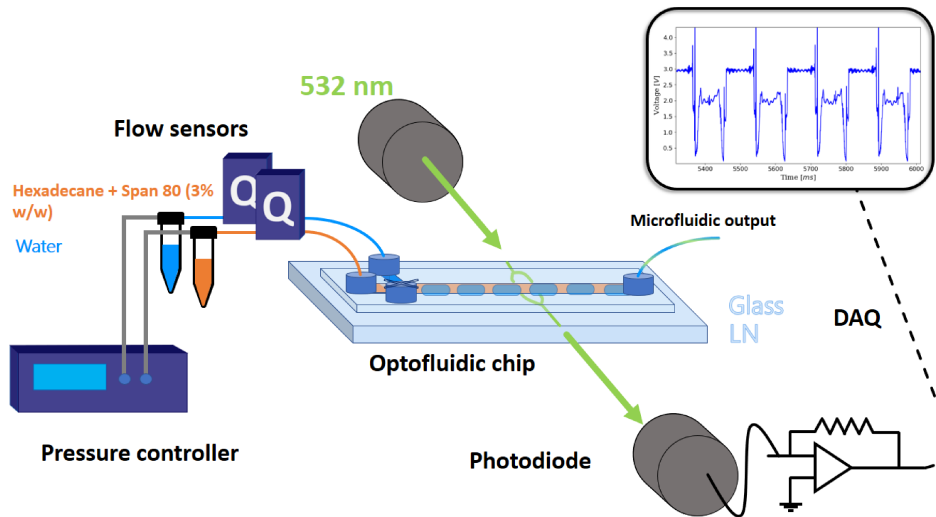

Figure 1.16: Experimental setup

Microfluidic component

The pump setup employed to inject the fluids in the microchannels is the Elveflow OB1 MK3 pressure driver pump (Elveflow, Paris, France). The experimental set-up can be equipped with three flowmeters BFS Coriolis10 (Bronkhorst, AK Ruurlo, Holland) providing a feedback system to control the flows: in this work we used just two flowmeters because a T-junction droplet generator was exploited. Since these fluxes are directly measured within the flowmeters, when microplastics were added to water droplets a self-assembled device (figure 1.17) has been used. Proposed by [62], it avoid to damage the micro-tubing circuit and the flowmeters due to the presence of solid microparticles. The continuous phase instead has been injected by directly connecting its flowmeter to the chip. This self-assembled device, which in the following will be called *buoy*, is installed in an upright position. In this way the upper and lower extremities are connected, by means of silicon tubes, to the outlet of the flowmeter appointed for the dispersed phase and to the inlet of the secondary microchannel, respectively.

The buoy acts as a reservoir and its working principle relies on the formation of an interface between two immiscible fluids that here are called "master" and "slave". The master fluid, which is injected in

the buoy first, is exposed to the pressure applied by the driver pump and, through the interface, forces the slave one to flow in the chip. Thus, the preliminary procedure repeated for every measurement to introduce the dispersed phase in the optofluidic platform - either in the case of MilliQ or solutions containing microplastics required initially to fill the buoy with hexadecane, playing the role of "master" fluid. Afterward, the outlet of the flowmeter, likewise filled with hexadecane, was connected to the upper extremity of the buoy, allowing the injection in the latter of the dispersed phase ("slave" fluid). Great care has been paid to prevent the insertion of air bubbles. Once the inlet of the secondary microchannel of the T-junction is joined to the lower extremity of the buoy, droplets were generated flowing in the main channel the continuous phase (hexadecane), directly injected in the chip by the pump through the second flowmeter.
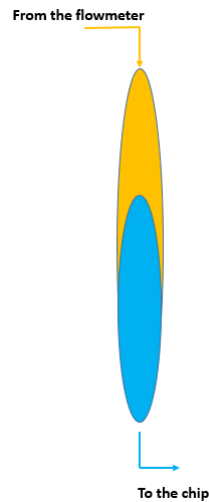

Figure 1.17: Sketch of a buoy realized by gluing with NOA resine two tips of a micropipette

Optical component

The optical coupling of the MZI waveguide is performed with a continuous diode laser with a power of 7.35 mW and a wavelength $\lambda = 532$ nm. The laser beam passes through a half plate and a polarizer so that, when it is focused to the input of the interferometer by means of a 20X Objective, both the TE and TM modes of the waveguide can be excited. The chip is located on a platform with 6 degrees of freedom, allowing both translation and rotation of the sample. Once light crosses the sample, perpendicularly to the droplet flowing direction, it is collected at the output of the guide by a 50X Objective and directed to a silicon photodiode. The outgoing signal is then amplified by exploiting a trans-impedance amplifier and digitalized by the acquisition fast card Ni 6023.
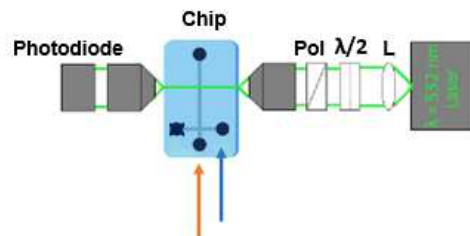
Figure 1.18: Schematic representation of the laser-waveguide coupling and light collection at the output of the optofluidic platform.

This optical configuration results be very flexible allowing freedom of action on the optofluidic platform. However, as it will be also mentioned in the following, the drawbacks are that this coupling is not "permanent". Recoupling procedures after each measurement are in fact needed, often influenced by

any mechanical stresses applied to the experimental setup.

A CCD camera, with a 10X objective, is placed below the chip in order to take screenshots of the droplets flowing in the main channel.

Measurement and analysis protocols

In this chapter, we discuss in 2.1 the performance of the employed optofluidic device in the detection of MilliQ droplets and solutions with microplastics droplets, as well as their identification. In sections 2.2 and 2.3 the measurement and analysis protocols are defined by identifying the best estimator for the optical signals evaluation and by setting the working conditions (combination of Q_c and Q_d) valid for all the acquisitions performed in the experiments. Finally, in section 2.4, the formulation of the power spectrum employed to investigate the frequency content of the oscillations characterizing the plateau of a single droplet signal is presented.

2.1 Optical trigger

A Mach-Zehnder optical circuit is crossed by a microfluidic channel so that the optical waveguides constituting the MZI branches are cut at 90 degrees (see figure 2.1). In this configuration the branches are de fact interrupted by the microfluidic channel but geometrically self-aligned. The light coupled into the MZ is in fact split into two branches each illuminating a microfluidic channel and the light transmitted detected by the opposite part of each branch. This system works as an optical probe since a dispersed phase passing across the MZ branches induces a transmission variation of the light detected at the opposite side of the microfluidic channel.
The versatility of the MZI waveguide geometry, in addition to its independence of any previous calibration procedures, makes the adopted optofluidic device a reliable optical trigger that provides several information on the matters flowing inside the channel through the transmitted optical signal.
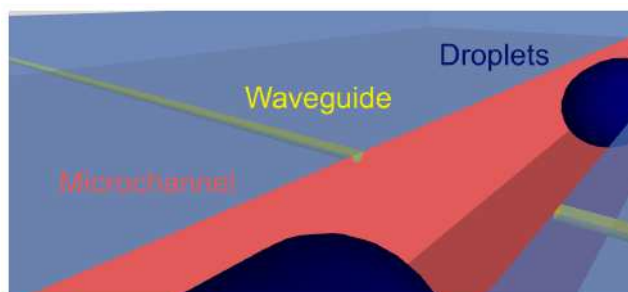
Figure 2.1: Schematic representation of the coupling between the main microchannel and the optical waveguide integrated in the lithium niobate optofluidic platform employed in this thesis

The optical transmission (OT) signal is collected by the photodiode and by a suitable electronics that amplifies by the trans-impedance amplifier and finally digitalized by the D/A converter is converted in a voltage signal $V(t)$ (V) as a function of time t (ms). The interaction between the droplets flowing inside the microfluidic channel and the light guided in the MZI waveguide is therefore measured.

The passage of a droplet in front of the two MZI branches drives a modulation of the output optical signal, providing four trigger times. The detection of these instants allows the droplet labeling as well as its length and velocity monitoring. Concerning the velocities measurements, the optofluidic platform has been successfully validated as a droplet velocimeter, working with a precision up to three times higher than the one guaranteed by a standard video camera microscope setup [45][63]. In this thesis, this feature will be exploited in the analysis of a droplets train, and the potentiality of the device in the detection of plastics microparticles contained in MilliQ solution will be shown.

The tracking of a single droplet, as well as its velocity characterization, can be extended to the case of a sequence of droplets. As a matter of fact the overall OT signal becomes, thus, a fingerprint of the flow inside the channel as proved by the resulting optical signal shown in figure 2.2. In this case the signal of a train od MilliQ water droplets has been produced and detected in the chip as the dispersed phase with hexadecane as the continuous one respectively.
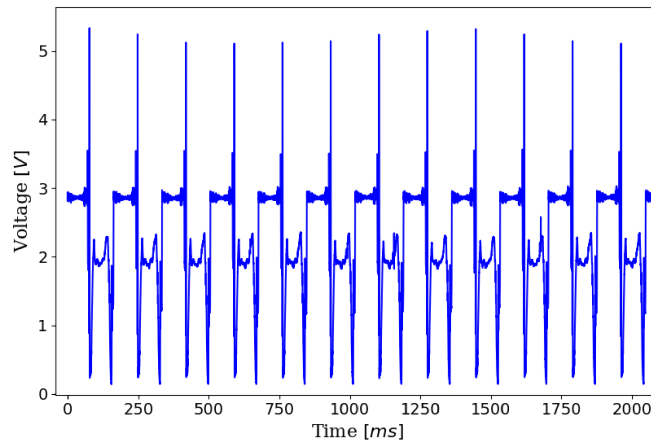
Figure 2.2: Signal of a sequence of water droplets acquired by the photodiode in about two second of acquisition adopting the fluxes $Q_C = 10$ μL/min and $Q_D = 8\mu$L/min

The droplets sequence here shown correspond to the passage of each droplet in front of the optical guide: the presence of the droplet is responsible of the light scattering of the transmitted light and results in a decrease in the transmitted signal. On the contrary the continuous phase (hexadecane) is detected as an homogeneous medium and,consequently, the detected signal is basically constant. This voltage level is directly linked to the coupling of the laser light to the MZI guide

It is worth mentioning that the signal acquired by every droplet in any train is extremely reproducible i.e the optical setup adopted ensures high accuracy of the droplets sensing.
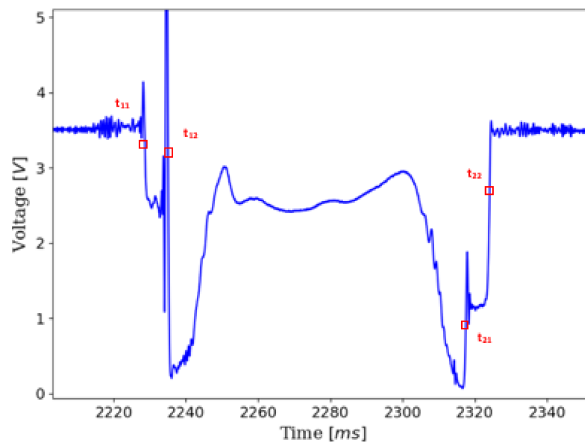
Figure 2.3: Signal of a single water droplet produced with $Q_C = 10$ μL/min and $Q_D = 8\mu$L/min

As far as the the detection of a single droplet is concerned, as it can be seen in Figure 2.3, the four

trigger times aforementioned are: t_{11} and t_{12}, corresponding to the interaction between the front droplet's meniscus with the first MZI arm and the second one, respectively; t_{21} and t_{22} representing, instead, the two instants of time at which the rear meniscus transits through the first arm and exits from the second one. The optical transmission changes at these times depend on the refraction of light on the interface between the droplet and the surrounding continuous phase. In particular, t_{11} and t_{12} are connected to a drop of the transmitted signal since the water droplet has a refractive index ($n = 1.33$) lower than hexadecane one ($n = 1.43$). The opposite holds for t_{21} and t_{22} which are associated with a rise of the collected light.
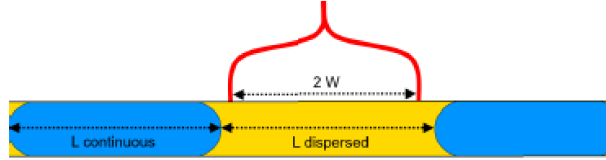
Figure 2.4: Sketch of the regime in terms of the acquired signal behaviour adopted in this study and determined by the condition $R = L/2W, \; 1$

It is important to clarify that the chronological sequence of the triggering times is related to the microfluidic regime in terms of acquired signal behavior. It depends on the ratio $R = L/2W$ where L is the droplet length and $2W$ identifies the distance between the two straight branches of the MZI guide. The only working conditions here employed, responsible for the OT signal behavior, are illustrated in figure 2.3 and schematically represented in figure 2.4 where $L/2W > 1$, with $2W = 40\mu m$. Different regimes determined by $L/2W < 1$ are characterized by different times and voltage levels. Their description is beyond the scope of this thesis, for a complete analysis [45] is recommended.

Therefore, considering a droplet with length $L/2W > 1$, the detection of t_{11} and t_{12} as well as t_{21} and t_{22} allows determining the front meniscus and rear meniscus velocity as follow:

$$v_{front} = \frac{2W}{t_{12} - t_{11}} \qquad v_{rear} = \frac{2W}{t_{22} - t_{21}} \tag{2.1}$$

Averaging these two values, an estimation of the single droplet's velocity v is obtained. With similar considerations, it is also possible to determine the length L, computed as an average of

$$L_1 = v_{front} \, (t_{21} - t_{11}) \qquad L_2 = v_{rear} \, (t_{22} - t_{12}) \tag{2.2}$$

.

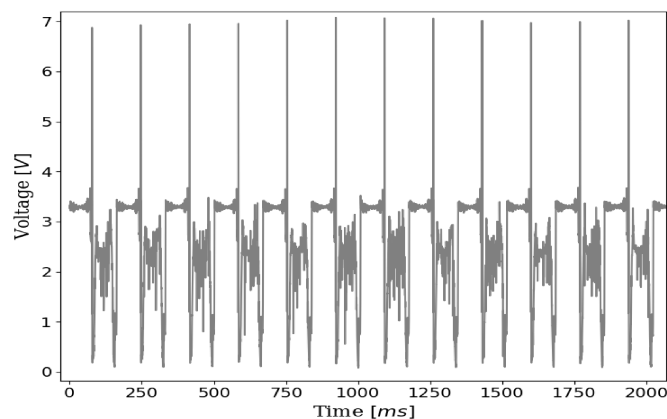**Figure 2.5:** Signal of a sequence of water with PS particles (2500 nm) droplets acquired by the photodiode in about two second of acquisition adopting the fluxes $Q_C = 10 \; \mu L/min$ and $Q_D = 8\mu L/min$

To evaluate the opto-microfluidic platform's capability of detecting microplastics, and therefore the effects of presence pf the plastic particles in the OT signal PS spherical microplastics with different

diameter have been dispersed in water. An example of a signal acquired in presence of these particles is shown in figure 2.5.

The flowing of a droplet sequence containing PS spheres in the channel provides a fingerprint of its passage across the MZI guide, characterized by a modulation of the light transmitted comparable to the one produced by water droplets. As a consequence, the reproducibility of the droplets sensing is ensured also in this case.

The presence of plastic particles in the dispersed phase is clearly recognisable by comparing the OT signal of a single water droplet (figure 2.3) to the one acquired given by a droplet with microplastics (figure 2.6).

The latter displays fluctuations that are completely absent in the case of the water droplet in the interval delimited by the two voltage absolute minima included in the range $[t_{12}; t_{21}]$ (in the following: droplet plateau). This visual evidence proves the presence of microplastics in the droplet whose interaction with the transmitted light is noticeably detectable.

The same physical considerations about the four trigger times t_{11}, t_{12}, t_{21} and t_{22}, as well as droplet's length L and velocity computations, hold also for water droplets with microplastics.
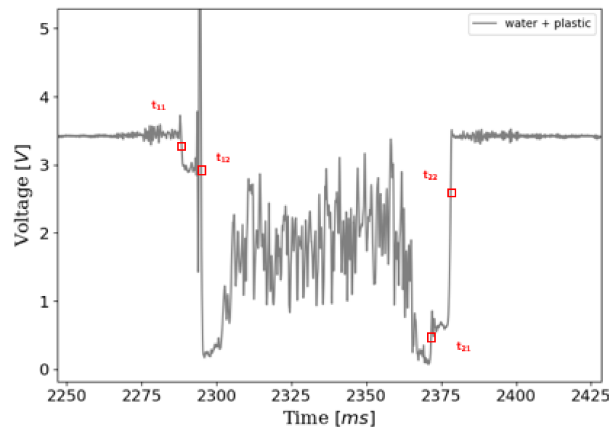
Figure 2.6: Signal of a single droplet containing PS particles (2500 nm) produced with $Q_C = 10$ μL/min and $Q_D = 8\mu$L/min

Further differences between the two signals can be deduced from figure 2.7. When PS microspheres are dispersed in water droplet the droplet length is $\sim 3\%$ shorter than observed in pure water droplets as well as the plateau of the signal is significantly lower, with respect the water case. Indeed, taking the voltage level of the hexadecane as a reference, the plateau of the droplet containing the microplastic spheres is $\sim 22\%$ lower than the water droplet one.
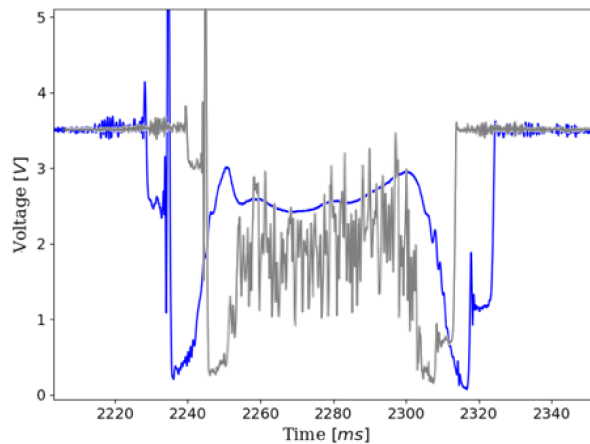
Figure 2.7: Superposition of the two single droplet signals illustrated in figures 2.3 and 2.6

This result has been plotted here for a ratio $\phi = Q_D/Q_C = 0.8$ and the same coupling of the laser to the optical guide being equal. These findings will be further discussed in the next sections.

2.2   Normalized integrals

In order to let this opto-microfluidic platform be a reliable sensing tool for identifying and quantifying microplastics in aqueous solutions it is mandatory to define a suitable protocol and implement an analysis technique that can distinguish in the OT signal between water-only and water with MP droplets. When identified, the second priority is to quantify the content of the latter in terms of particles dimension, concentration, composition respectively.

To achieve this goal an indicator i.e. an analytical parameter is needed. In particular, it has to be:

- simple to compute given the considerable number of data sets to analyse;

- independent of the coupling of the laser to the MZI guide - and therefore on the hexadecane's voltage signal -, since it varies for each data sets;

- independent of the shape of the signal which is affected not only by the content of the dispersed phase, as it is shown in section 2.1, but also by external factors such as instabilities of the experimental apparatus;

- sensitive not only to the MP particles' presence and to the different signal they can generate, but their concentration in the aqueous solution and dimension as well.

The indicator satisfying these requirements has been investigated by comparing several signal profiles depending on the experimental conditions for droplets generation, including microfluidic channels geometry as well as different Q_d/Q_c ration to have various droplets sizes. It has been evidenced that the most reliable parameter is given by the area under the plateau of each i-th droplet's signal which is defined as:

$$I_i(t)^1 = \frac{1}{\Delta t_i} \int_{t-\Delta t_i/2}^{t+\Delta t_i/2} V_i(t)\, dt \qquad (2.3)$$

where $V_i(t)$ describes the OT signal acquired in the interval Δt_i, representing the duration (namely the number of sampled points) of the droplet passage in between, referred to the two voltage absolute minima aforementioned. A sketch of the physical meaning of this choice is reported in figure 2.6 and figure 2.3. These minima, as well as the four trigger times, are a fingerprints of each droplet sequence signal, regardless of the dispersed phase content which affects the droplet plateau voltage trend as well as its length. For these reasons they are a well-defined reference in the computation of the integral $I_i(t)$.

The latter quantity, which is expressed in V, has been evaluated by applying three different normalization procedures, in order to find out the best estimator independently of the droplet generation conditions and possible size dispersion.

These estimators are evaluated for every i-th droplet belonging to a sequence signal. Three mean values I_N, $I_{N,cut}$, and $I_{N,avg}$ are then computed for the overall sequence sampled with the associated standard deviation.

I_N, dimensionless, is calculated according to the equation:

$$I_N = \frac{1}{n} \sum_{i=1}^{n} \frac{I_i(t)}{V_{C-hexa}^i} \qquad (2.4)$$

where n is the total number of droplets sampled in a sequence. Referring to the figures 2.8a and 2.8b, the i-th droplet integral $I_i(t)$ is normalized to the centroid V_{C-hexa}^i of the hexadecane's voltage level V_{hexa} detected immediately before the front droplet's meniscus intersects the first MZI arm (to the left of the plateau) and immediately after the passage of the rear meniscus across the second arm (to the right of the plateau).

---

[1]Since the signals acquired are sampled with a frequency of 50 kHz, $I_i(t)$ is actually a discrete integral which can be approximated to a continuous one, yet.
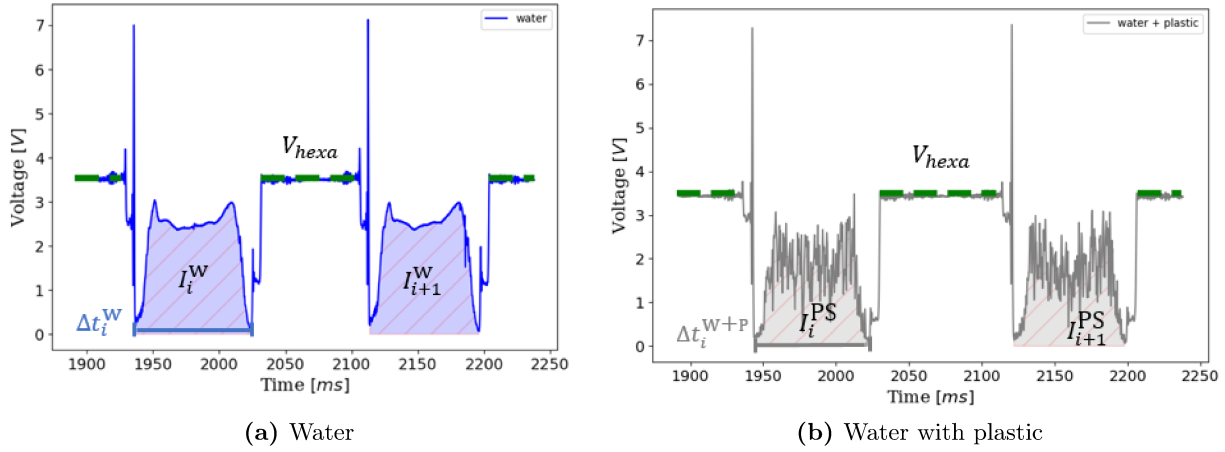
(a) Water

(b) Water with plastic

Figure 2.8: Representation of the area under the plateau of a single droplet signal computed with 2.3; they are delimited by the two voltage absolute minima, Δt_i^W apart from each other in the case of water (2.8a) and Δt_i^{W+P} in the case of water with plastic dispersed phase (2.8b). The green dashed line marks the hexadecane's voltage level V_{hexa} whose centroid is exploited to compute I_N.

The choice of the centroid V_{C-hexa}^i as normalizing factor arises from the need to take into account of systematic errors due to the coupling of the laser. In fact, since every measurement requires a suitable coupling procedure, the hexadecane voltage level of different signals acquired may change according to the coupling efficiencies of the laser into the input waveguide, hence affecting the voltage level of the plateau of a droplet signal as well.

The reason why $I(t)$ is not normalized to the area under V_{hexa} - which would be a priori the most reasonable choice - is due to the frequency variation of droplets production according to the microplastic spheres' concentration in the dispersed phase. Therefore, at fixed values of the ratio $\phi = Q_d/Q_c$, droplets having, according to equation 1.8, the same length but different concentrations exhibit different time intervals between each other (see figure 2.9), affecting the integral under the hexadecane signal but leaving V_{hexa} unchanged. Moreover the droplets production is also influenced by fluxes instabilities which, on the contrary, do not alter significantly the voltage of the continuous phase.
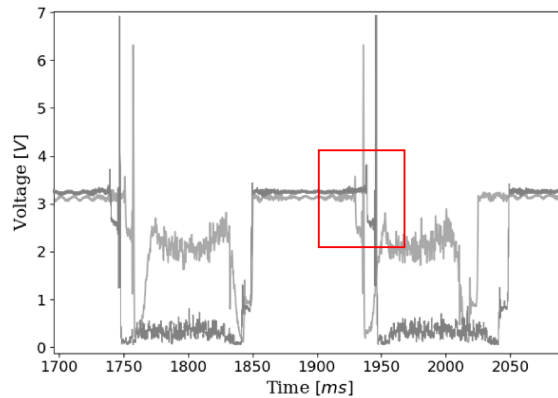
Figure 2.9: Representation of two signals obtained separately by flowing in the microfluidic circuit solutions of PS-617 nm particles at fixed ϕ=0.8 but with different concentrations, namely C= 0.14 $\pm$ 0.03 mg/g (light grey) and C=4.47 $\pm$ 0.03 mg/g [2] (dark grey). The focus is on the different time interval between two consecutive droplets, emphasized by matching up the signals of the two first droplets in correspondence of the respective rear meniscus passage across the second arm of the MZ guide.

---

[2]mg of PS particles over g of water (see chapter 3 and table 3.4).

The estimator $I_{N,cut}$ is computed as the previous one, except that only the 50% of the points describing the signal of each droplet plateau is considered. Therefore, it is derived from:

$$I_{N,cut} = I_N^{50\%} = \frac{1}{n} \sum_{i=1}^{n} \frac{I_i(t)^{50\%}}{V_{C-hexa}^i} \tag{2.5}$$

In this case, $I_i(t)$ selects the area centered around the time centroid t_C, as it is shown in figure 2.10b. As a consequence, the time length Δt_i and the corresponding voltage values are obtained referring to that restricted area and not to the whole droplet plateau, as for I_N. In this way, the diffraction effects caused by the interaction of the droplet's menisci with the laser light across the MZI guide, if they are present, are non included in the data analysis. More in detail, the origin of a diffractive pattern is due to the presence of a gap between the droplet top and the cover that act a slit. This gap is in our case filled by the continuous phase as a result of the functionalization procedure (see section 1.2.5). Therefore, when a droplet intersects the input waveguide, representing an obstacle put in the way of the laser beam, it creates the equivalent of a slit that gives rise to diffraction [64]. The influence of the latter on the droplet plateau signal, strictly related to the slit width since it varies with time according to the moving droplet shape, can be evaluated by comparing I_N and $I_{N,cut}$, as it will be done in section 2.3 through figure 2.11.

Finally, the normalized integral $I_{N,avg}$ (figure 2.10c) comes directly from $I_{N,cut}$ since it is obtained by dividing the i-th restricted area previously described by the voltage mean value V_{avg} of the corresponding droplet plateau. As a result $I_{N,avg}$, expressed in $(1/V)$, is computed as follow:

$$I_{N,avg} = \frac{1}{n} \sum_{i=1}^{n} \frac{I_i^{N,cut}}{(V_{max}^i + V_{min}^i)/2} = \frac{1}{n} \sum_{i=1}^{n} \frac{I_i^{N,cut}}{V_{avg}} \tag{2.6}$$

where n is once again the total number of the droplets considered, V_{max}^i and V_{min}^i are the maximum and the minimum V level of the i-th droplet signal plateau, limited at 50% around t_C, respectively. This further normalization allows to investigate the fluctuations V_{avg} depends on, thus characterizing the signal of the droplets containing plastic particles.

(a) I_N **(b)** $I_{N,cut}$ **(c)** $I_{N,avg}$
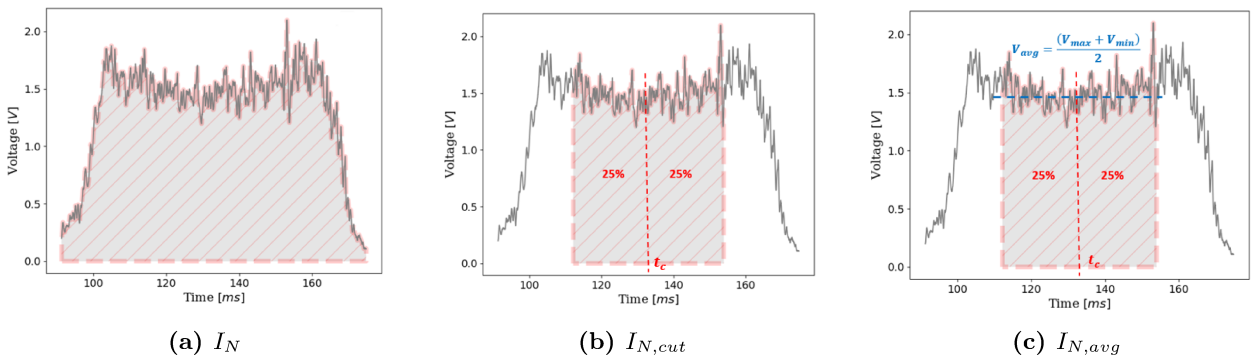
Figure 2.10: Examples of the area evaluated by each normalized integral for a single droplet containing PS-340 nm particles with concentration C7 (see table 3.2)

2.3 Preliminary results

In order to establish the best parameter between I_N, $I_{N,cut}$, and $I_{N,avg}$ for the data analysis, preliminary measurements have been performed by fixing the fluxes ratio $\phi = Q_D/Q_C = 0.8$ and the concentration C=0.65 mg/g of the PS spherical particles with a 340nm diameter introduced in the water-droplets. The experimental procedure relied on the following protocol:

a) acquisition, for each combination of fluxes Q_D and Q_C giving $\phi = 0.8$, of the signals produced by a 20-second-long water droplet sequence;

b) acquisition, for each combination of fluxes Q_D and Q_C giving ϕ=0.8, of the signals produced by a 20-second-long water droplet sequence containing the PS particles.

It is worth to clarify that, for the two employed dispersed phases (water and water with PS particles), the data collection proceeded from the lowest value of both Q_D and Q_C to the highest ones, as indicated in the table 2.2. In this way, gradually increasing the flows of both the dispersed and the continuous phase, the fluxes instabilities due to the pump system are limited.

The measure of the average velocity $\bar{v}_{avg}$ of each droplets sequence is reported in table 2.2. As expected, the higher the fluxes are the quicker the droplets flow.

$Q_D(\mu\mathrm{L/min})$	$Q_C(\mu\mathrm{L/min})$	$\bar{v}_{avg}$ (μm/ms)		γ
		water	PS	
4.8	6	3.78 ± 0.09	3.9 ± 0.1	
6.4	8	5.1 ± 0.2	5.12 ± 0.02	
8	10	6.47 ± 0.03	6.44 ± 0.02	0.8
8.8	11	7.09 ± 0.02	7.02 ± 0.03	1.9
10	12.5	8.09 ± 0.04	8.06 ± 0.05	0.5
12	15	9.82 ± 0.03	9.77 ± 0.05	0.9
14	17.5	11.37 ± 0.04	11.49 ± 0.04	2.1
16	20	13.10 ± 0.04	13.13 ± 0.05	0.5

Table 2.1: Combinations of the dispersed phase and continuous phase fluxes Q_D and Q_C, and comparison through the compatibility γ between the water droplets' average speed $\bar{v}_{average}$ and the one of the droplets containing the PS particles.

In figure 2.11, the three parameters I_N, $I_{N,cut}$ and $I_{N,mean}$ are presented as a function of $\bar{v}_{avg}$ for each combination of fluxes employed. These three parameters were obtained from the signals generated by the passage of droplets containing microplastics.
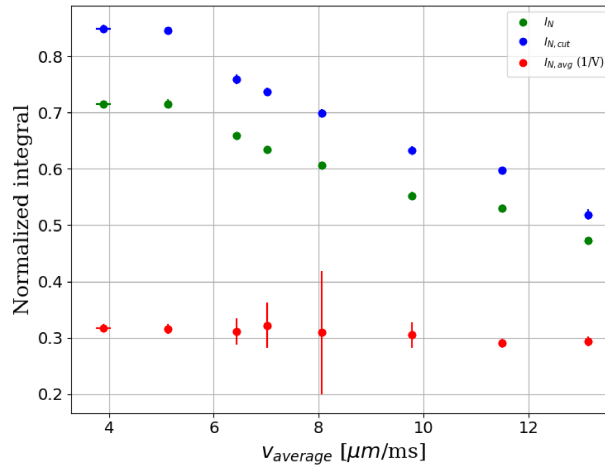
Figure 2.11: Trend of the normalized integrals I_N, $I_{N,cut}$ and $I_{N,avg}$, computed for each combination of fluxes Q_D and Q_C having ratio $\phi = Q_D/Q_C = 0.8$, related to the droplets containing PS particles with a diameter of 340 nm, as a function of the corresponding $\bar{v}_{avg}$ reported in table 2.2

It is evident how $I_{N,avg}$ is completely independent of $\bar{v}_{avg}$, making it unable to distinguish droplets with different speed. On the contrary, I_N and $I_{N,cut}$ have a very similar decreasing trend. Therefore, for this thesis, $I_{N,avg}$ is excluded as the best estimator. However, if the analysis is focused just on the different microplastic concentrations in the droplets, it can be a valid parameter regardless of the

latter dimension.

Since I_N and $I_{N,cut}$ are correlated, as evident from their common trend, it is reasonable to use only one of them as the best estimator. Thus, considering the goal of this thesis, I_N has been selected as the reference parameter for the analysis. An example of its effectiveness is presented in figure 2.12. It shows how I_N can clearly identify the presence of the MP particles PS-340 nm (figure 2.12a) and PS-2500 nm (figure 2.12b), with respect to the correspondent sequence of water droplets produced with the same combinations of fluxes. Moreover, comparing I_N values in the water-with-plastic droplets, it is proved that the I_N parameter is sensitive to the different particles' diameter. In fact I_N values differ when comparing PS-340nm to PS-2500 nm spheres solutions for more than 10% at a fixed Phi value and at similar sphere concentration.

(a)   (b)

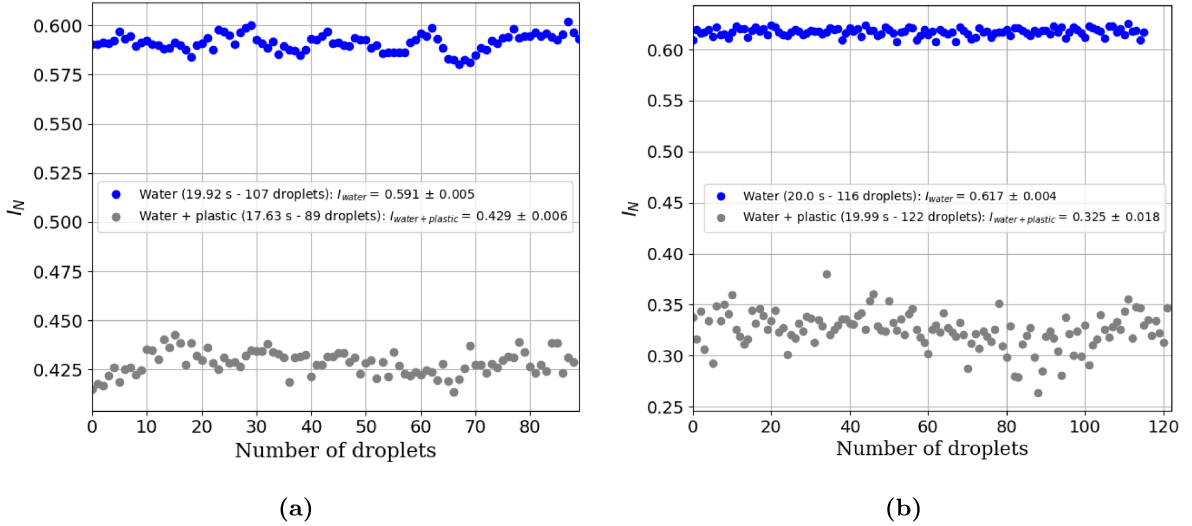**Figure 2.12:** Figure 2.12a illustrates I_N values of each droplet detected, comparing the signal generated by a sequence of droplets containing a concentration C=4.48±0.06 mg/g of PS-340 nm particles (in grey) with the one describing water droplets sequence (in blue); both signals have been acquired with the combination of fluxes Q_D=8 μL/min and Q_C=10 μL/min. The same holds for the PS-2500 nm particles represented in figure 2.12b that have been evaluated with a concentration C=4.51±0.03 mg/g.

Anyway, $I_{N,cut}$ has turned to be useful to compute, for each sequence of droplets sampled, the parameter

$$m = \frac{1}{n} \sum_{i=1}^{n} \frac{V_{max}^i - V_{min}^i}{V_{max}^i + V_{min}^i} \qquad (2.7)$$

that will be employed in section 3.1.2 and 3.2.2 as an alternative to $I_{N,avg}$ to evaluate, excluding possible diffraction effects, the hypothetical correlation between the fluctuations of the plateau of each droplet signal in presence of plastic, and the different content of the dispersed phase in dimension and concentration.

As far as the length of the droplets containing plastics is concerned (see table 2.1), their values range from 591±6 μm, for the combination of fluxes Q_D=4.8 μL/min and Q_C=6 μL/min, to 557±11 μm in the case of Q_D=16 μL/min and Q_C=20 μL/min, showing a decreasing trend with the increase of the droplet velocity. Moreover, the length of the water droplets generated by the same Q_c and Q_d is higher than the one of the droplets with PS particles except the case when Q_d=4.8 $\mu L/min$ and Q_c=6 $\mu L/min$ [3].

---

[3]The standard deviation σ_Q associated to each flow rate value is $\sigma_Q = 0.2 \frac{\mu L}{min}$. The two cases labelled with $*$ in the table 2.2 are affected by a significant fluctuations $\delta Q = \sigma_Q/Q$ ($\delta Q \geq 3$ %) which characterize flow rates' values less than 7 $\frac{\mu L}{min}$. This uncertainty leads to a dispersion in the droplet's length within the same sequence

$Q_d(\mu\mathrm{L/min})$	$Q_c(\mu\mathrm{L/min})$	$\bar{L}_w$ (μm)	$\bar{L}_{PS}$ (μm)	γ
$*$ 4.8	6	582 ± 12	591 ± 6	
$*$ 6.4	8	591 ± 36	575 ± 5	
8	10	578 ± 4	570 ± 4	1.4
8.8	11	574 ± 3	564 ± 5	1.7
10	12.5	571 ± 4	567 ± 8	0.4
12	15	572 ± 2	566 ± 4	1.3
14	17.5	565 ± 3	561 ± 2	1.1
16	20	561 ± 2	557 ± 11	0.4

Table 2.2: Combinations of the dispersed phase and continuous phase fluxes Q_d and Q_c, and comparison through the compatibility γ between the water droplets' length $\bar{L}_w$ and the one of the droplets containing the PS particles $\bar{L}_{PS}$.

The compatibility

$$\gamma = \frac{\left|\bar{L}_w - \bar{L}_{PS}\right|}{\sqrt{\sigma_w^2 + \sigma_{PS}^2}}$$

is $0.4 \leq \gamma \leq 1.7$ for all the measurements performed (table 2.2), where $\bar{L}_w$ and $\bar{L}_{PS}$ represent respectively the average length of pure water and water with microparticles droplets, with σ_w and σ_{PS} the corresponding standard deviations respectively. The systematic analysis carried out here allows to define a sensibility thresholds that is concentration dependent. In particular for high microplastic concentration such as C=0.65 mg/g, the presence of PS particles of any size is not detectable through a droplet's shape analysis.

This result doesn't represent a limiting factor since high concentrations can be easily detected by standard imaging approaches that have already reached a mature level of technology applications. Instead, lower microplastics concentrations are still a challenge in optical detection-based tools and our results suggest that the LiNbO$_3$ platform is highly sensitive a low concentrations. Finally, our results clearly indicate the best experimental conditions to maximize the opto-microfluidic platform in terms of optimal choice of the continuous/dispersed phase flux. Figure 2.11, shows that fluxes adopted for $\bar{v}_{avg}$ less than 6 μm/ms does not provide enough sensibility since I_N and I_N, cut are also almost constant. This result suggests the use of fluxes combination ensuring droplets velocity higher than that threshold.
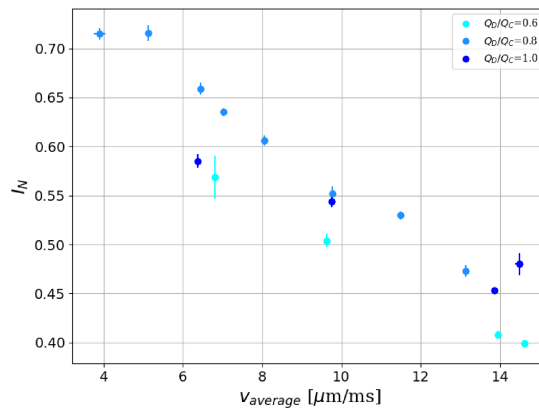
Figure 2.13: Comparison between I_N values, expressed as a function of the average droplets' speed $\bar{v}_{avg}$, that have been obtained employing combination of fluxes having three different ratio $\phi = Q_D/Q_C$: 0.6, 0.8 and 1.0. The dispersed phase was the same for every measurement: water with a fixed concentration C= 0.65 mg/g of PS-340 nm microspheres

In addition to the measurements at fixed $\phi = 0.8$, preliminary experiments have been made by varying

the ratio $\phi = Q_D/Q_C$.

In particular, figure 2.13 displays the dependence of I_N on the average droplets' speed, comparing values obtained with different ratios $\phi=Q_D/Q_C$: 0.6, 0.8 (reported also in the plot of figure 2.11) and 1.0. Data referred to ϕ=0.6 and ϕ=1.0, as in the case of ϕ=0.8, have been acquired adopting the PS particles with a 340 nm diameter, fixing the concentration C=0.65 mg/g as well.

Excluding the combination of fluxes Q_D=20 μL/min Q_C=20 μL/min, which seems to provide a squeezing-to-dripping transition in the droplets production regime, in the range $6 \leq \bar{v}_{avg} \leq 14$ μm/ms the behavior of the integral is similar, showing a decreasing trend. As displayed by the last ϕ=1.0 point at $\bar{v}_{avg}$=14.48 $\pm$ 0.01 μm/ms, in fact, the squeezing-to-dripping transition can be inferred because in this working condition the droplet break-up at the junction of the microfluidic channels starts to be dominated by the viscous shear stress. In this case the Capillary number Ca is higher, with values typical of a dripping regime. In fact, given the hexadecane viscosity μ_c=3 cP and an interfacial tension $\gamma \sim 4.11$ mNm^{-1}, Ca is ~ 0.011 which is close to $Ca^* \sim 0.015$ and higher than 0.0044, i.e. the values respectively suggested by De Menech et al. in 2008 [65] and, more recently (2020), by Arias et al. [66] to mark in a T-junction the squeezing mechanism transition into the dripping regime.

Therefore the choice of using the ratio ϕ=0.8, and in particular by fixing $Q_c = 10$ μL/min and $Q_d = 8$ μL/min, is mainly based on the results obtained in previous studies ([45][63]), concerning the characterization of an optofluidic device with MZI waveguides integrated in LN as droplets velocimeter. Such combination of fluxes, in the case of pure water droplets, provides an average length $\bar{L}_w$ =561 $\pm$ 9 μm and an average velocity $\bar{v}_{avg} = 6.21 \pm 0.04$ μm/ms [15], defining an experimental condition which is appropriate for the dimensional features of the device. Moreover, as verified in [14] and [16], this experimental condition is suitable to test the effect of a space-charge field, photo-induced on an iron-doped LiNbO$_3$ sample, on a single droplet with such lenght (see section 5.3). As a consequence, unless otherwise noted, every figure or result reported later in this thesis will refer to measurements that have been performed with the combination of fluxes $Q_C = 10$ μL/min and $Q_D = 8$ μL/min .

2.4   Power spectrum

The normalized integral I_N provides info on microplastics in the droplets at a macroscopic level by means of evaluating the area under the plateau of each droplet signal.

The signal of microplastics in water droplet exhibits a noisy shape with maxima to minima difference as large as 50% of the signal dynamics. Similar water droplets, instead, produce signals without these fast-in-time oscillations, as a consequence it is reasonable to attribute this noisy response to the presence of microplastics. To get more detailed information about the fluctuations in water with plastic signals a Fourier analysis was implemented. In particular, it relied on the computation of the Discrete Fourier Transform (DFT) of the sampled voltage signal describing the optical transmission at the output of the waveguide [67].

The optical signal acquired for each sequence of droplets generated brings information on the overall aqueous solution content, that is both water and the microplastics within it. As a consequence in this thesis we proposed to interpret $V_i(t)$, as expressed in 2.3, as

$$V_i(t) = V_i(t)_w * V_i(t)_P$$

i.e. a time convolution of the signal contribute coming from the water dispersed phase $(V_i(t)_w)$, and the contribute of the plastic particles transmitted light $(V_i(t)_P)$.

Exploiting the properties of the Fourier Transform (FT), it is possible to derive the frequency content $\widehat{V_i}(t)_P$ of each droplet produced in a sequence, since

$$\widehat{V_i}(\nu) = \widehat{V_i}(\nu)_w \cdot \widehat{V_i}(\nu)_P \tag{2.8}$$

$$\widehat{V_i}(\nu)_P = \frac{\widehat{V_i}(\nu)}{\widehat{V_i}(\nu)_w} \tag{2.9}$$

where $\widehat{V_i}(\nu)$, $\widehat{V_\nu}(\nu)_w$ and $\widehat{V_i}(\nu)_P$ are the DFT of the their respective time representations.

In order to compute $\widehat{V}_i(\nu)_P$, with $i = 1...n^{th}$ droplets, from a droplet-sequence signal collected both for the water and the water with microplastic dispersed phases (see the protocol in section 2.3), the following procedure was implemented:

a) point-by-point average voltage estimation of the plateaux of the water signal; it provides the sequence $V_{avg,w} = \{V_{avg,w}(t_j)\}_{t_j=0}^{\Delta t_w}$ with $V_{avg,w}(t_j) = \frac{1}{n}\sum_{i=0}^{n} V_i(t_j)_w$. The latter is obtained by averaging, on n droplets, the voltage level $V(t_j)_w$ of each droplet signal at the j-th instant of the time length $\Delta t_w = min\{\Delta t_i\}_{i=1}^{n}$, to whom every droplet plateau signal longer than Δt_w was truncated, ensuring equal length signals. In this way the average operation is allowed;

b) computation of the point-by-point DFT $\widehat{V}_{avg,w} = \{\widehat{V}_{avg,w}(\nu_j)\}$;

c) computation, each droplet produced by the water with plastic dispersed phase taken individually, of the point-by-point DFT $\widehat{V}_i = \{\widehat{V}_i(\nu_j)\}_{\nu_j=0}^{\nu_{sampling}}$ with $\nu_{sampling}$=50 kHz

d) evaluation of $\Delta t_{min} = min(\Delta t_w; \{\Delta t_i\}_{i=1}^{n})$ and computation of

$$\widehat{V}_i(\nu_j)_P = \frac{\widehat{V}_i(\nu_j)}{\widehat{V}_{avg,w}(\nu_j)} \quad \nu_j \in [0; \nu_{sampling}] \tag{2.10}$$

where the sequences $\widehat{V}_{avg,w}(\nu_j)$ and $\widehat{V}_i(\nu_j) \: \forall \: i = 1...n$ are truncated in the frequency domain, so that they have the same time length Δt_{min} (see figure 2.14) with a point-by-point correspondence in the evaluation of $\widehat{V}_i(\nu_j)_P$.

Hence, the Fourier transform $\widehat{V}_i(\nu)_P$ is given by the sequence $\{\widehat{V}_i(\nu_j)_P\}_{\nu_j=0}^{\nu_{sampling}}$

Finally, to describe the distribution of power into the frequency components composing the signal $V_i(t)_P$, its energy spectral density $\bar{S}_i(\nu)_P =\mid \widehat{V}_i(\nu)_P \mid^2 = \widehat{V}_i(\nu)_P \cdot \overline{\widehat{V}_i(\nu)_P}$ has been estimated.

It is important to point out that, in order to avoid boundary effects and limit possible artifacts in the power spectrum due to the truncation of either $\widehat{V}_{avg,w}(\nu_j)$ or $\widehat{V}_i(\nu_j)$ (or both), an epsilon parameter $0 \leq \epsilon \leq 20$ points (1 ms =50 points) has been introduced, so that each i-th power spectrum $\bar{S}_i(\nu)_P$ has been evaluated considering a truncation time $\Delta t'_{min} = \Delta t_{min} - \epsilon$ with ϵ selected such that $\bar{S}(\nu)_P = \{\bar{S}_i(\nu)_P\}_{i=0}^{n}$ is maximized. An example of power spectrum is illustrated in figure 2.15 .
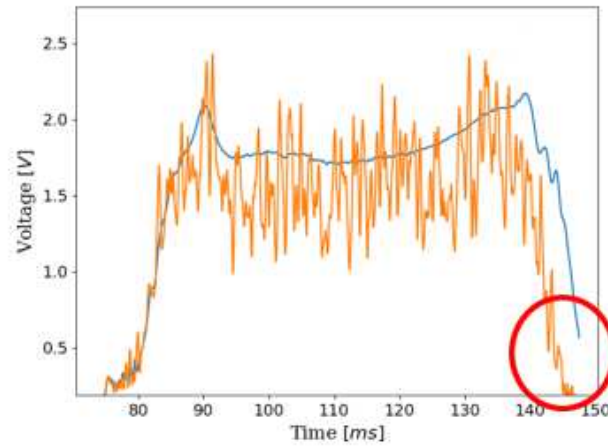
Figure 2.14: Superposition of $V_{avg,w}$ (in blue) obtained averaging point-by-point the plateau of each water droplet signal, composing the overall sequence acquired, with the first droplet signal (in orange) generated by a dispersed phase containing PS-617 nm particles (C=0.64 mg/g). The red circle spots the difference in time length between the two signals and the consequent truncation, described in section 2.4, which is applied on $(V_{avg,w})$, in this case.
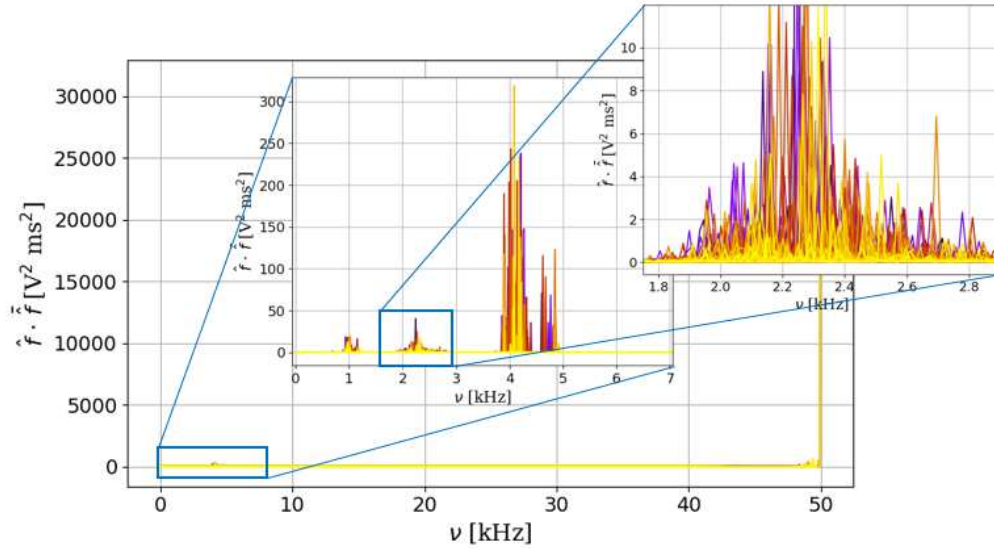
Figure 2.15: Power spectrum of a sequence of droplets containing PS-617 nm particles (C=0.64 mg/g). The focus is on the second peak present in a three-peaks-structure characterizing the region at lower frequencies. Each line that composes the peak represents the power spectrum $\bar{S}_i(\nu)_P$ of a single droplet.

In general, regardless of the concentration m_{PS}/m_w and the dimension of the particles considered, power spectra present a well-recognizable structure characterized by three main groups of peaks, as it is shown in figure 2.15, that are arranged in the frequency domain ν [kHz]=[0,50] where the upper limit coincides with the sampling frequency of the optical transmission.

However, the frequency position and intensity of the peaks vary according to the spheres' diameter and their concentration in such a way that it is not straightforward to extract unambiguous information about the content of the aqueous solution analyzed. For this reasons, the fine structure of the frequency oscillations has not been investigated, and we focused the attention on performing instead a qualitative analysis of power spectra. Great the attention has been paid to investigate their not trivial dependence on the water signal employed and derive an estimation of the microplastics' concentration (see appendix A).

Therefore, the analysis carried out in this thesis project relies on the results provided by the parameter I_N which proves to be very trustworthy.

PS particles comparison

This chapter concerns the comparison between the results produced by the different microparticles (PS-340 nm, PS-617 nm, PS-1050 nm, PS-2500 nm) diluted in MilliQ water solutions. In particular, section 3.1 investigates the normalized integral I_N as a function of the different concentrations of PS-340 nm and PS-2500 nm particles, expressed as mass of PS micro-spheres m_{PS} over the mass of water m_w (mg/g). Moreover the effects of the same concentrations on the parameter m, introduced in section 2.3, and the fluctuations in the droplet signal according to the diameter of the particles, are also presented. The same investigations are discussed for the PS-617 nm and PS-1050 nm MPs in section 3.2.

The data produced by the different PS spherical microparticles, acquired following the protocol described at the beginning of section 2.3, have been analyzed by comparing separately the PS-340 nm with the PS-2500 nm, and the PS-617 nm with the PS-1050 nm. As reported in table 3.1, PS-617 nm and PS-1050 nm have a diameter which is approximately an integer multiple of λ, unlike the PS-340 nm and PS-2500 nm ones. Therefore two different regimes in the intensity transmitted by the microparticles have been identified depending on the ratio $2R/\lambda$. As already known by the Mie Theory ([68][69][70]), the light scattering can strongly depend on the size of the particles illuminated by light. Consequently in the microplastic-water droplets, scattering effect of microplastics should be taken into account and it is expected to affect the behavior of the parameters I_N and m, varying the PS concentrations, according to the diameter of the particles.

d (nm)	340	617	1050	2500
d/λ	~ 0.6	~ 1.2	~ 2.0	~ 4.7

Table 3.1: Ratio between the diameter d of the particle and the wavelength λ of the laser beam

3.1 PS-340 nm and PS-2500 nm

3.1.1 I_N vs m_{PS}/m_w

The trend of the normalized integral I_N for the PS-340 nm particles, represented in figure 3.1a, resembles the one observed in the optical transmission of the PS-2500 nm microspheres (see figure 3.1b). In particular, taking as a reference the I_N of the water signal (point blue), measured at $(Q_C = 10\mu L/min, Q_D = 8\mu L/min)$, it is evident the growth of the integral values at the lower concentrations reported in the tables 3.2 and 3.3. In the case of the PS-2500 nm particles this growth is of $\sim 5\%$ for C2, which provided the highest integral value, while for the PS-340 nm microplastics is not possible to give an estimate since, due to systematic errors, all the integrals I_N are affected by an offset that makes the curve in figure 3.1a stand completely below the water integral. Nevertheless, its increase is straightforward.

Name	PS mass (mg)	Water mass (g)	m_{PS}/m_w (mg/g)
C0	0.5	3.8766	0.13 ± 0.03
C1	0.2	0.9184	0.2 ± 0.1
C2	0.6	1.2589	0.45 ± 0.08
C3	7.1	10.7705	0.65 ± 0.01
C4	1.6	0.9328	1.8 ± 0.1
C5	2.4	0.8524	2.8 ± 0.1
C6	10.1	2.5899	3.88 ± 0.04
C7	7.0	1.5580	4.48 ± 0.06
C8	5.0	0.6430	7.7 ± 0.2
C9	4.0	0.5060	7.9 ± 0.2
C10	13.0	0.9567	13.6 ± 0.1

Table 3.2: 340 nm PS microparticles concentrations. Masses with a standard deviation of 0.1 mg

Name	PS mass (mg)	Water mass (g)	m_{PS}/m_w (mg/g)
C0	0.5	3.8727	0.13 ± 0.03
C1	0.6	3.9124	0.15 ± 0.03
C2	0.5	2.1082	0.23 ± 0.05
C3	6.9	10.5609	0.65 ± 0.01
C4	3.2	2.9592	1.08 ± 0.03
C5	1.6	0.9437	1.7 ± 0.1
C6	2.3	0.9255	2.5 ± 0.1
C7	3.8	1.0742	3.55 ± 0.09
C8	14.0	3.0953	4.51 ± 0.03
C9	4.3	0.7564	5.7 ± 0.1
C10	8.0	1.0696	7.50 ± 0.09

Table 3.3: 2500 nm PS microparticles concentrations. Masses with a standard deviation of 0.1 mg

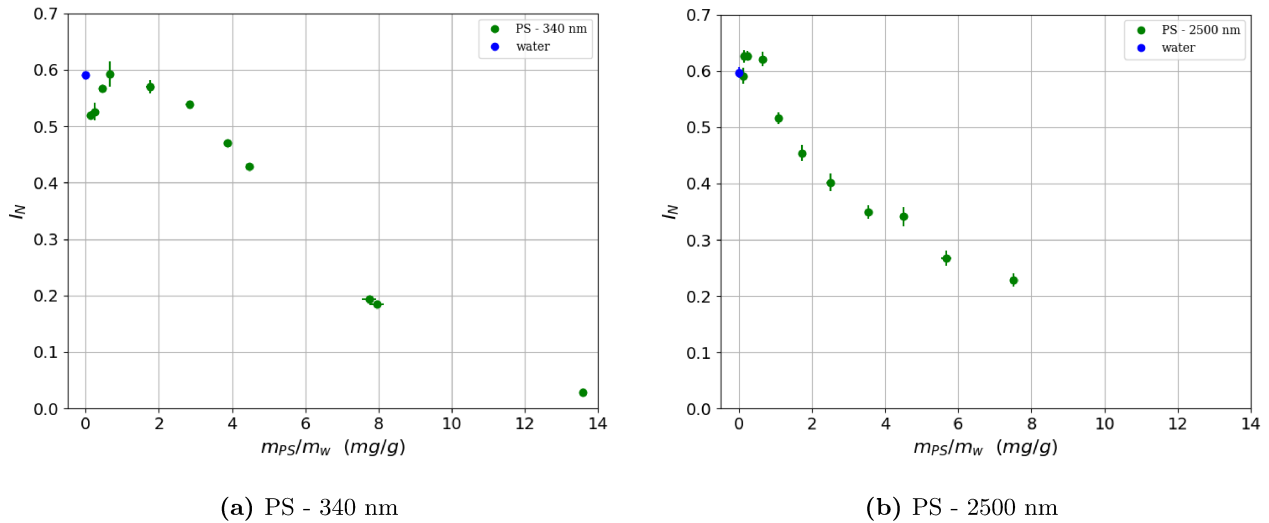(a) PS - 340 nm   (b) PS - 2500 nm

Figure 3.1: In figure 3.1a is reported the trend of I_N parameter by varying the concentration m_{PS}/m_w for the PS-340 nm particles, while figure 3.1b displays the correspondent I_N behavior for the PS-2500 nm spheres.

A significant decrease, $\sim$62% for the C10 PS-2500 nm concentration and $\sim$95% for the C10 PS-340 nm concentration (offset excluded) with respect to the correspondent water integrals, can be observed when approaching I_N=0, for more concentrated solutions. From the optical point of view these two opposite behaviors result respectively in an initial increase of the transmitted light followed by a dominance of extinctions effects (absorbance and scattering) that limit the intensity of the PS-OT signal compared to the water one.

It is worthy to underline that in the case of the PS-2500 nm the integral trend decrease is sharper than the correspondent PS-340 nm one ($\sim$+20 % by comparing the respective integrals at the same concentration). This is due to the larger diameter of the particles that, for the same concentration, produce a more consistent reduction of the transmitted light and, therefore, smaller I_N values.

3.1.2 m vs m_{PS}/m_w

(a)   (b)
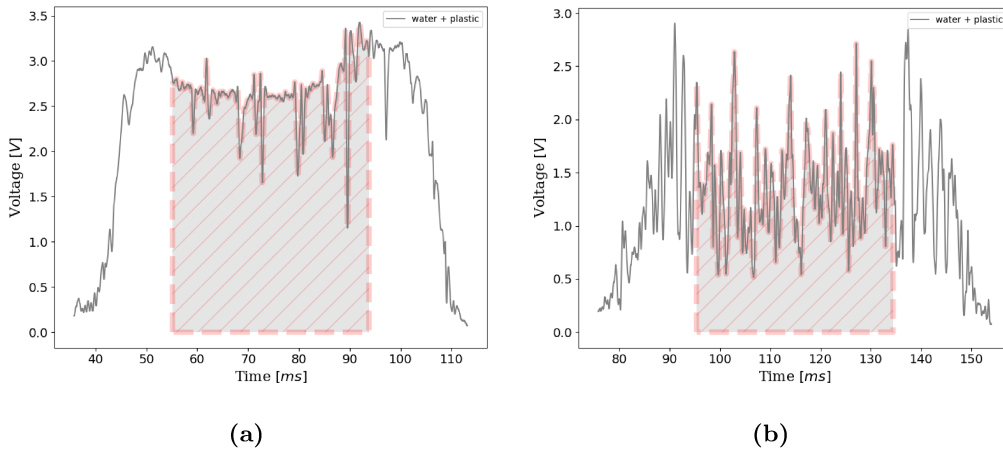
Figure 3.2: Figure 3.2a shows the plateau of the signal produced by a single droplet containing PS-2500 nm microplastics at C3=0.65 $\pm$ 0.01 mg/g. The same holds for figure 3.2b that displays the case at C8=4.51 $\pm$ 0.03 mg/g. The focus is on the 50% of the area under each signal to emphasize the effects of the different concentrations on the signals' fluctuations.

Figure 3.2a and figure 3.2b describe the dependence of the droplet signal fluctuations on the MP particle concentration. The higher the concentration is, the stronger the fluctuations and the lower the light collected, i.e the voltage level of the centroid of the droplet plateau.

To better investigate this correlation with the droplet content, the parameter m (see section 2.3), and its σ_m have been exploited.

It is important to point out that all m data evaluated in the current section, as well as in the following, will be plotted without the correspondent standard deviation σ_m. As a matter of fact, σ_m is, in some cases, of the same order of m, as already visible in figure 3.3a and figure 3.3b.

Comparing the PS-340nm particles with the PS-2500 nm ones, it can be noticed that m shows a monotonically increasing trend as a function of m_{PS}/m_w in both cases, confirming the previous considerations about the droplet content-fluctuations correlation. Once again, it is clear how the particle dimension plays a role in the distribution of the m values, and in the σ_m one as well. The fact that σ_m decreases as the plastic concentration grows, approaching a constant value at higher concentrations, results in a stabilization of the signal fluctuations. It clearly emerges that the quicker the fluctuations increase the fastest their stabilization is, both for PS-2500 nm and PS-340 nm particles.

The particular increasing trend followed by σ_m for $m_{PS}/m_w \to 0$ is reasonably related to a local enhancement of concentration due to particles patches formation, which is more probable at lower concentrations of microplastics ($m_{PS}/m_w < 1$). Therefore, sudden and stronger reductions of the transmitted light correspond to a smoother voltage signal for more diluted aqueous solutions (for instance, in the case of the concentration C0 both for the PS-340 nm and PS-2500 nm particles, the

correspondent droplet OT signals can exhibit sudden reductions of $\sim 17\%$ and $\sim 30\%$ with respect to the voltage level of the plateau centroid). This becomes evident when analysing the plateau of the droplet signal and quantifying the relative increase of σ_m.

It is possible to note that the PS-340 nm data do not follow a well-defined trend, as in the PS-2500nm case, since they show a more marked variability. This is due to the instabilities (fluxes instability, mechanical vibrations on the setup, etc...) that may happen and that show a greater contribute for the measurements performed when the PS-340 nm particles have been adopted.
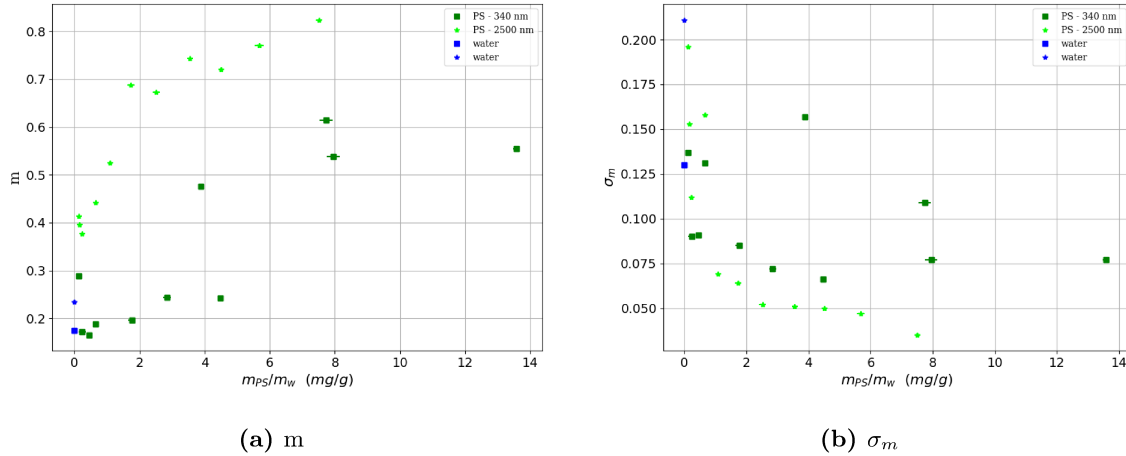

(a) m   (b) σ_m

Figure 3.3: Figure 3.3a shows the comparison between m parameters obtained from the analysis of PS-340 (green) nm and PS-2500 nm (light green) particles, while figure 3.3b the correspondent σ_m trends. The blue points represent the water base signals detected on the same day of the spheres data acquisition.

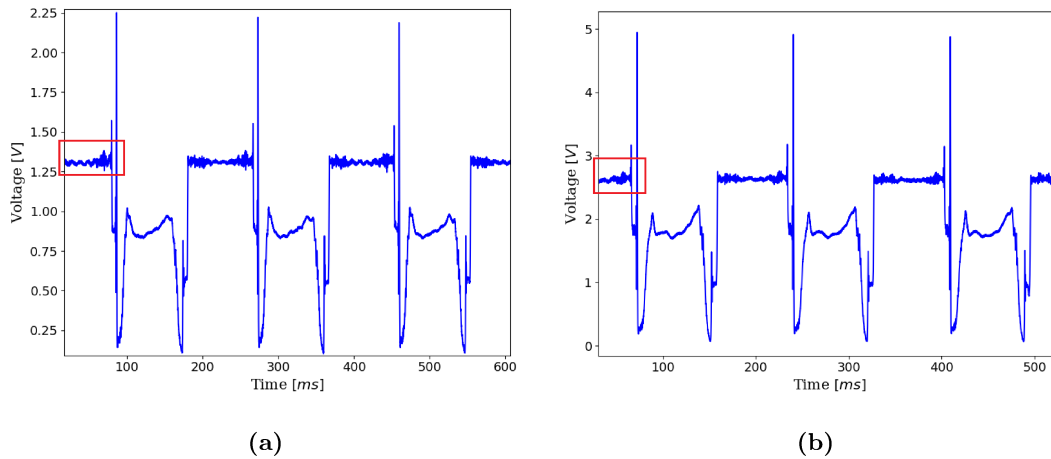(a)   (b)

Figure 3.4: Figure 3.4a illustrates the signal of a sequence of three water droplets detected on the day when the PS-340 nm particles were introduced in the dispersed phase, while figure 3.4b describes an analog signal but referred to the PS-2500 nm measurements day. The red boxes mean to spot the different coupling of the laser with the MZI guide between the two water signals.

It is important to stress that the parameter m is not independent of the optical coupling of the laser with the MZI guide. This is visible considering the blue points in the figures 3.3a and 3.3b referred to the water signals acquired with different couplings. By comparing figure 3.4a to figure 3.4b it is possible to quantify the impact of measures reproducibility when comparing, for instance, results achieved in two distinct days. Any uncertainty due to light coupling efficiency that may induce signals values dispersion can be easily removed when the light coupling is made by way of the pig-tailing technique. In this thesis it has been used a direct coupling approach to enhance the flexibility in the experiment

design, with special care to the droplets generation and microplastics inclusions. It is clear, in fact, that eventual unwanted microplastics deposit within the channel requires cleaning processes that are not compatible with fiber pigtailing. As a consequence, in this thesis the focus has been fixed on the determination of the best microfluidics condition to achieve the best microplastics detection and higher sensibility. When achieved this result, the optical optimization of the signal detection can be easily achieved by using the pigtailing coupling. [45][71][72].

3.2   PS-617 nm and PS-1050 nm

3.2.1 I_N vs m_{PS}/m_w

The calculation of the parameter I_N, relative to the PS-617 nm and the PS-1050 nm particles have been expressed as a function of the spheres concentrations (see tables 3.4 and 3.5). The relative trend is reported in figure 3.5a and figure 3.5b respectively.

Name	PS mass (mg)	Water mass (g)	m_{PS}/m_w (mg/g)
C0	0.5	3.5795	0.14 ± 0.03
C1	0.5	2.1328	0.23 ± 0.05
C2	0.5	1.1331	0.44 ± 0.09
C3	1.3	2.0797	0.64 ± 0.05
C4	1.5	1.3465	1.14 ± 0.07
C5	1.6	0.9391	1.7 ± 0.1
C6	2.4	0.8495	2.8 ± 0.1
C7	16.7	3.7354	4.47 ± 0.03
C8	7.5	1.3415	5.63 ± 0.07
C9	10.0	1.3560	7.39 ± 0.07

Table 3.4: 617 nm PS microparticles concentrations. Masses with a standard deviation of 0.1 mg

Name	PS mass (mg)	Water mass (g)	m_{PS}/m_w (mg/g)
C0	0.5	3.8693	0.13 ± 0.03
C1	0.5	2.0930	0.24 ± 0.05
C2	0.6	1.2568	0.45 ± 0.08
C3	7.1	10.7727	0.66 ± 0.01
C4	1.5	1.4675	1.04 ± 0.07
C5	1.6	0.9339	1.7 ± 0.1
C6	2.3	0.8636	2.7 ± 0.1

Table 3.5: 1050 nm PS microparticles concentrations. Masses with a standard deviation of 0.1 mg

Taking again the water signal as a reference, the decrease of the integral values, as m_{PS}/m_W increases, is around 90% for the PS-617 nm spheres and 88% for the 1050 nm ones, when the integrals of the respective highest concentration are considered. I_N curve seems to approach a constant value at the higher concentrations for both cases. In particular, it is very sharp for the PS-1050 nm particles which exhibit more intense extinctions effects in the interactions with the laser light than the PS-617 nm ones. For these reasons it has been limited the experimental investigation to solutions containing PS-1050 nm particles having $m_{PS}/m_w < C6$. For $m_{PS}/m_w > C6$ the acquisition system was not able to detect so low level of transmitted light.

The evidence that no increasing trend can be detected at lower concentrations confirms, as expected, the effects of the role of $2R/\lambda$ in the identification of two distinct regimes whereby particles interact

with the laser according to their diameter. These results are not in contradictions with those reported for microplastics with diameter equal to 340nm and 2500nm respectively (see section 3.1.1).
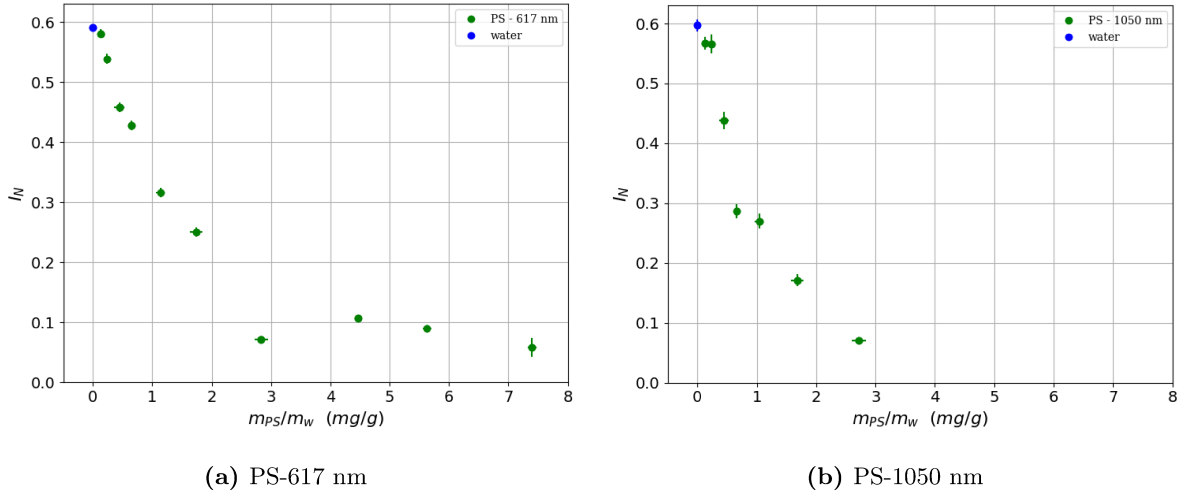

(a) PS-617 nm

(b) PS-1050 nm

Figure 3.5: Figure 3.5a represents the trend of I_N parameter by varying the concentration m_{PS}/m_w for the PS-617 nm particles, while figure 3.5b shows the correspondent I_N behavior for the PS-1050 nm spheres.

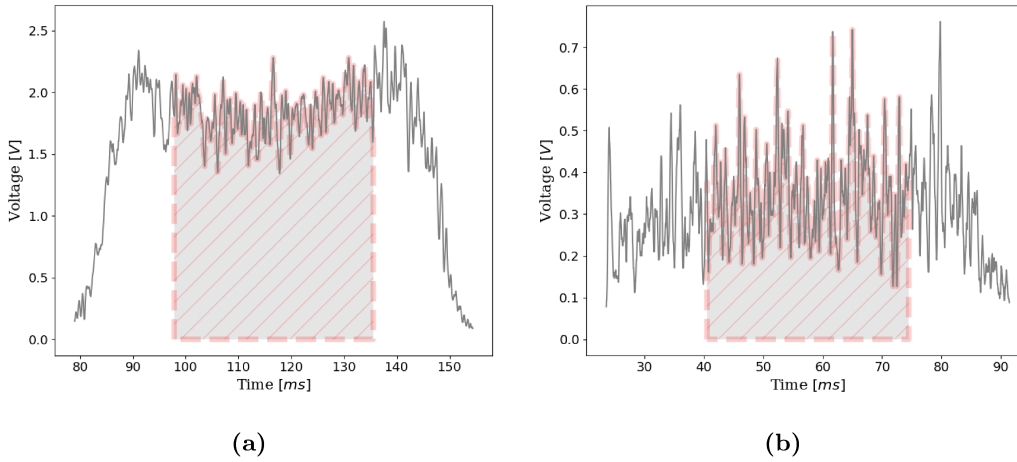### 3.2.2 m vs m_{PS}/m_w

(a)

(b)

Figure 3.6: Figure 3.6a illustrates the plateau of a signal produced by a single droplet containing PS-617 nm spheres at C1=0.23 $\pm$ 0.05 mg/g. The same holds for figure 3.6b but in the case of C7=4.47 $\pm$ 0.03 mg/g. The focus is on the 50% of the area under each signal to bring the effects of the different concentrations on the signals' fluctuations out.

The different effect of fluctuations on the signal of a droplet containing different concentrations of MP is, as expected, visible also on the PS-617 nm and PS-1050 nm particles. Analog observations about the voltage level of the droplet plateau and the amplitude of the fluctuations are reported in figure 3.6a and figure 3.6b when C7>C1 for the specific case PS-617 nm.
Similarly to what discussed in section 3.1.2 about the optical coupling and the differences between the two water signals acquired separately for the PS-340 nm and the PS-2500 nm measurements as well as what shown for the PS-617 nm and PS-1050 nm particles, figure 3.7a and figure 3.7b illustrate the dependence of the parameter m and the correspondent standard deviation σ_m on m_{PS}/m_w respectively,

evaluated for each droplet sequence signal, on m_{PS}/m_w.
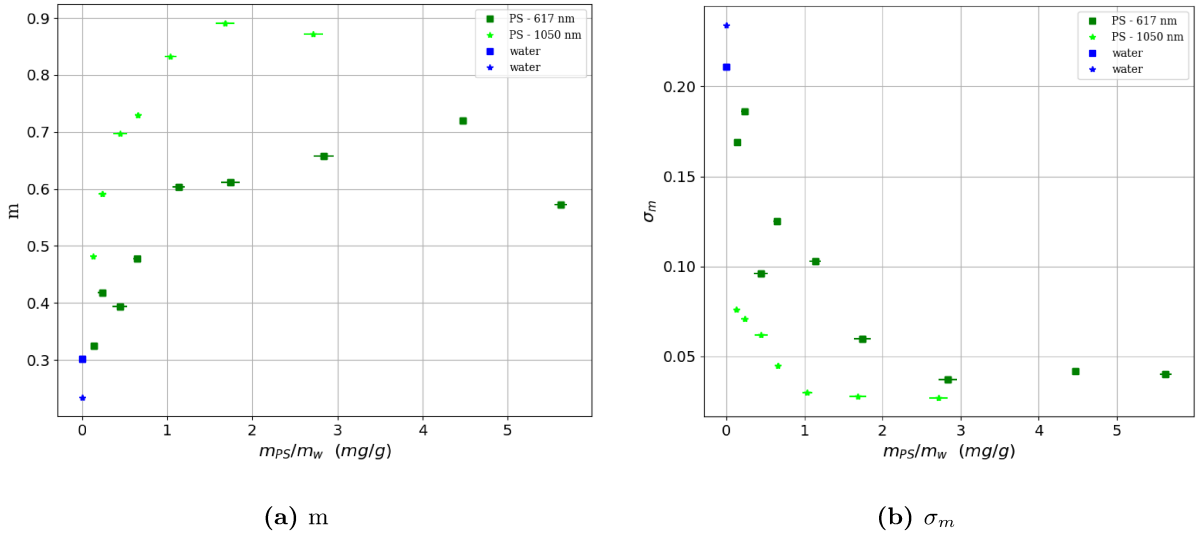

(a) m

(b) σ_m

Figure 3.7: Figure 3.7a shows the comparison between m parameters obtained from the analysis of PS-617 (green) nm and PS-1050 (light green) nm particles, while figure 3.7b the correspondent σ_m trends. The blue points represent the water base signals detected on the same day of the spheres data acquisition.
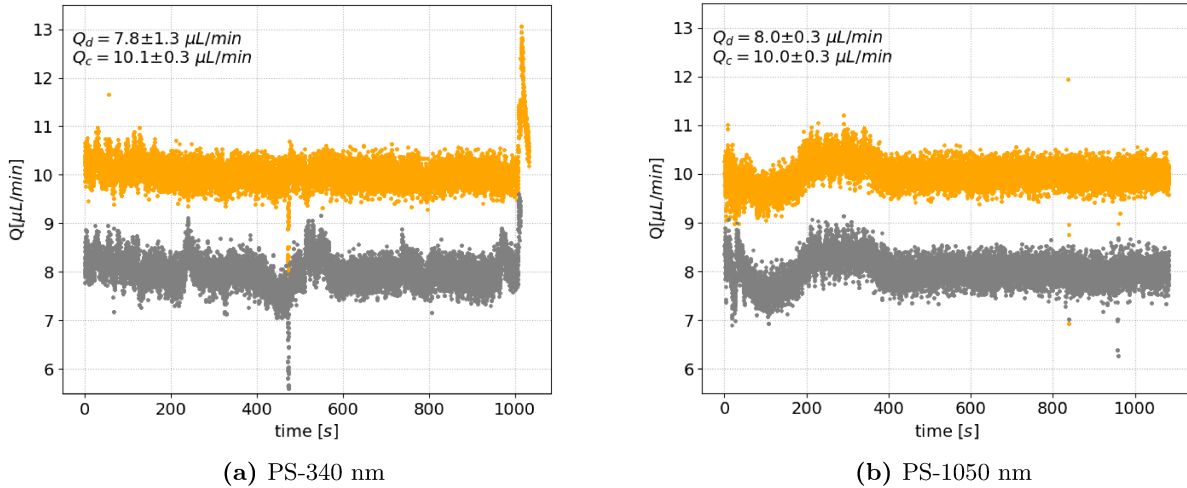

(a) PS-340 nm

(b) PS-1050 nm

Figure 3.8: Figure 3.8a shows, in a temporal interval of about 18 minutes, the fluxes trend of the continuous phase Q_c (in orange) and the dispersed phase Q_d (in grey) containing the PS-340 nm particles. The same holds for figure 3.8b in the case of PS-1050 nm spheres.

The trends of m and σ_m describe a well-defined curve both for the PS-617 nm and the PS-1050 spheres, showing a limited influence of the instabilities introduced by the experimental setup. Figure 3.8 presents a comparison between the flowmeters trends characterizing the PS-340 nm particles measurements (figure 3.8a), analyzed in section 3.1, and the PS-1050 nm ones (figure 3.8b). Focusing on the dispersed phase fluxes, it is evident the presence of strong instabilities affecting the PS-340 nm measurements, as can be seen in figure 3.3. As a matter of fact, PS-340 nm Q_d flux displays variations of $\sim$17% with respect to its mean value, while Q_d flux referred to the PS-1050 nm particles shows a more limited dispersion, quantified in $\sim$4%. An analog variability characterizes also the flux of the dispersed phase

containing the PS-617 nm MPs, justifying the well-defined trend of the curves depicted in figure 3.7. As it is shown in figure 3.3a and figure 3.3b, also in this case the increase of m with m_{PS}/m_W is associated to a decrease of the correspondent σ_m that tends to assume a constant value. Therefore these results prove, once again, that the the quicker the fluctuations increase the fastest their stabilization is. Moreover, such finding suggests a correlation with the dimension of the microspheres involved. As a matter of fact, these results and the previous one obtained for PS-340 nm and PS-2500 nm particles, show that particles with larger diameter exhibit a bigger m value at fixed m_{PS}/m_W. Moreover particles with larger diameter show a smaller correspondent σ_m than of the relative smaller particles ones respectively.

Finally, σ_m exhibits the same trend observed in section 3.1.2 when m_{PS}/m_W approaches 0, both for the PS-617 nm and PS-1050 nm. It is evident, therefore, that it is a matter of concentration since the dimension of the particles affects only the rate of the curve increase, as it is clear in figure 3.7b.

3.3   Variability in the droplet length

In this section an hypothesis justifying the observed large variability of the droplets' length is proposed by introducing the Pickering emulsion effect.

Regardless of the diameter of the PS spheres considered, the evaluation of the average length L_{avg} of a droplets' sequence containing MP was quite complex. Although L_{avg} can be evaluated by averaging the single droplet length L on the n droplets composing the sequence produced, a large dispersion was observed, with standard deviations $\sigma_{L_{avg}}$ even greater than 10% of L_{avg}. This evidence limited the precision in estimating the microplastics concentration in the diluted solutions and, consequently, the definition of a analytical trend of L_{avg} as a function of m_{PS}/m_w. This complexity cannot be attributed to the data acquisition procedures nor the chosen set-up configuration because all signals of MilliQ droplets signals allowed computing the average lengths with $\sigma_{L_{avg}} \leq 1.5\%$ (when no strong fluxes instabilities occurred). As a consequence, it is evident that the presence of microparticles in the droplet considerably contributes to the observed variations of L_{avg} values.

According to [15], by considering as a reference a MilliQ droplet average length of 566±7 μm, an approximated estimations of L_{avg} for the 4 types of PS particles have been determined at different concentrations:

- PS-340 nm: $550 \leq L_{avg} \leq 610$ μm

- PS-617 nm: $560 \leq L_{avg} \leq 591$ μm

- PS-1050 nm: $528 \leq L_{avg} \leq 605$ μm

- PS-2500 nm: $557 \leq L_{avg} \leq 573$ μm

The observed length dispersion cannot be justified by fluctuations introduced by the experimental setup because pure water droplets don't show this behaviour. In the case of microplastics enriched droplet, in order to explain this phenomenon, we suggest that the Pickering emulsion effect should be considered.

Pickering emulsions are particle-stabilized systems. Droplets dispersed in emulsions without emulsifiers, due to their high interfacial area, make these systems thermodynamically unstable. They are usually stabilized by including low molar mass surfactants or surface-active polymers in the formulations to decrease the interfacial tension between the phases. Studies carried out by Ramsden and Pickering revealed another way of stabilizing the droplets, i.e. by employing solid particles (usually micro- or nanoparticles) as a replacement for the surfactants [73].

Although the use of the latter to stabilize mixtures of oil and water in the form of emulsions is credited to Spencer Pickering, the first that investigated this mechanism, extending it also to bubbles in a foam, was Walter Ramsden. The British biochemist in fact worked intensively on the spontaneous formation (by agitation) of solid or highly viscous coatings on the free-surfaces (i.e. air-water) of protein solutions and of non-protein-containing colloidal dispersions, paving the way to a wide exploration of Pickering

emulsions in the biomedical field, in particular since the early 2000s [74]. The superior stability, low toxicity, and stimuli-responsiveness compared to classical emulsions treated with surfactants make the Pickering emulsions stabilization effect very attractive in biomedicine, especially for topical drug delivery [75] and bio-imaging [76], as well as in the area of biomass-based particles where it is exploited in the context of foods and topical creams [77].

The preparation of a Pickering mixture depends on the size and shape of the particles included in it, as well as their concentration and wettability properties.

Referring to the diameter of the MP particles adopted in this preliminary study, it is interesting to note that Bink et al. in [78] used spherical, monodisperse polystyrene latex particles of different sizes to explore the effect of particle dimension on the properties of oil-water emulsions. They found out that the sedimentation stability of the latter decreased if increasing the particle diameter in the 0.21 to 2.7 μm range. Moreover, other works, studying the influence of different particle shapes on a decane-water interface, proved the stabilizing effect of polystyrene spherical particles, although they resulted to be less effective than elliptical PS ones.

Focusing on concentration dependence[1] it is known that for most Pickering emulsion systems, the increase in particle concentration not only decreases the formed droplet size and improves surface coverage, but also leads to the formation of a network structure around the emulsion droplets, which further improves the emulsion stability [73]. Bink and co-workers analyzed SiO_2 particles in droplets of an oil-water emulsion system, and found that by increasing the concentration the droplet size of the emulsion decreases if the concentration is kept lower than 3%, and it remains instead unchanged above that threshold.
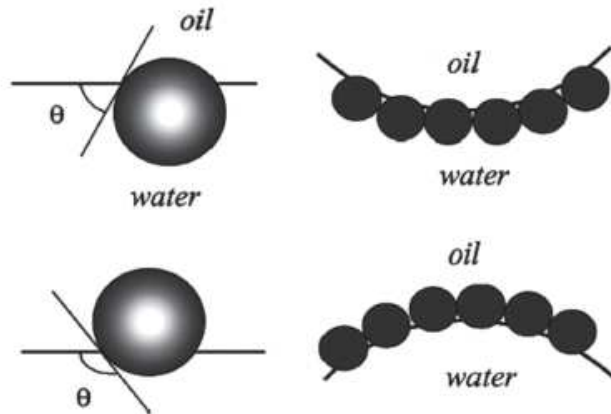

Figure 3.9: Sketch of the contact angle (left) and corresponding probable positioning (right) of particles at the oil-water interface, in the case of hydrophilic (top) and hydrophobic (bottom) spheres. The wettability of the particles, thus, induces the formation of an oil-in-water (o/w) emulsion, or of a water-in-oil (w/o) emulsion, depending on whether $\theta < 90°$ or $\theta > 90°$, respectively. The image is taken from [73]

On the basis of the experimental results presented in this thesis, on PS spherical particles with a diameter between 0.34 μm and 2.5 μm and at concentrations not exceeding $\sim 1.3\%$, it reasonable to suppose that microparticles included in the dispersed phase acted as surfactants, contributing at the reduction of the surface tension γ at the droplet interface. If so, this would induce a direct consequence on the droplet frequency production. In fact, according to equation 1.9, the lower γ the higher $\bar{f}$ is, thus promoting a larger number of generated droplets at higher particles concentration at fixed production time.

In conclusion, the Pickering emulsion stabilizing effect can be claimed as a potentially active when PS microspheres are dispersed in our water droplets but need further investigation that goes beyond the scope of this thesis. However, given the analogies between the aforementioned studies with the experimental framework here considered, further investigations and analysis on this hypothesis are

---

[1]rather than on wettability one, which is directly related to particles desorption energy at the interface.

going to be carried out in the next future.

Theoretical models describing I_N dependence on the particles concentration m_{PS}/m_W

In this chapter some models will be discussed to explain the results reported in Chapter 3 to fit the trends of I_N points obtained for different PS-particles. In section 4.1 a model based on the well-known Lambert-Beer is presented. Then, in section 4.2, an interesting approach involving Super-Poissonian fluctuations is employed to describe the data referred to PS-617 nm and PS-1050 nm particles. Moreover a transmittance-correction to the latter model is introduced in section 4.3 with the aim of fitting I_N values computed from PS-2500 nm signals. Finally, section 4.4 presents a model inspired to the scattering Mie theory and a correction of the Lamber-Beer law, in order to describe the results produced by PS-340 nm spheres.

4.1   Lambert-Beer model

The first approach to reproduce the trend of an optical transmission signal describing the physical interaction of a radiation with a medium of depth x is to apply the Lambert-Beer law.

Keeping in mind what reported in 3, if we observe the plots of I_N as a function of the solutions' concentration, data obtained from the PS-617 nm and the PS-1050 nm particles follow a decreasing exponential curve. On the contrary, it is evident how I_N values for PS-340 nm and PS-2500 nm do not fit such a curve.

Therefore, the data reproducing the dependence of I_N on the concentration m_{PS}/m_W for the PS-617 nm and the PS-1050 nm MP can be fitted with the exponential extinction law:

$$I_N(c) = a \cdot \exp^{-b \cdot c} \tag{4.1}$$

which describes the attenuation of the light as a function of the varying concentration $c = m_{PS}/m_W$ in the case that the medium thickness is constant.

Both fitting parameters, a and b,are reported in table 4.1 and table 4.2, while figure 4.1 and figure 4.2 show fitted data together with the correspondent normalized residuals plot, for the PS-617 nm and PS-1050 nm particles, respectively.

Residuals plot referred to the PS-617 nm suggests that their distribution is not random, with a sort of correlation between errors. In the case of the PS-1050 nm, although few points are considered, the normalized residuals seem not to follow a stochastic trend showing mutual dependence as well. These findings indicate that the Lamber-Beer model does not describe correctly these observations.
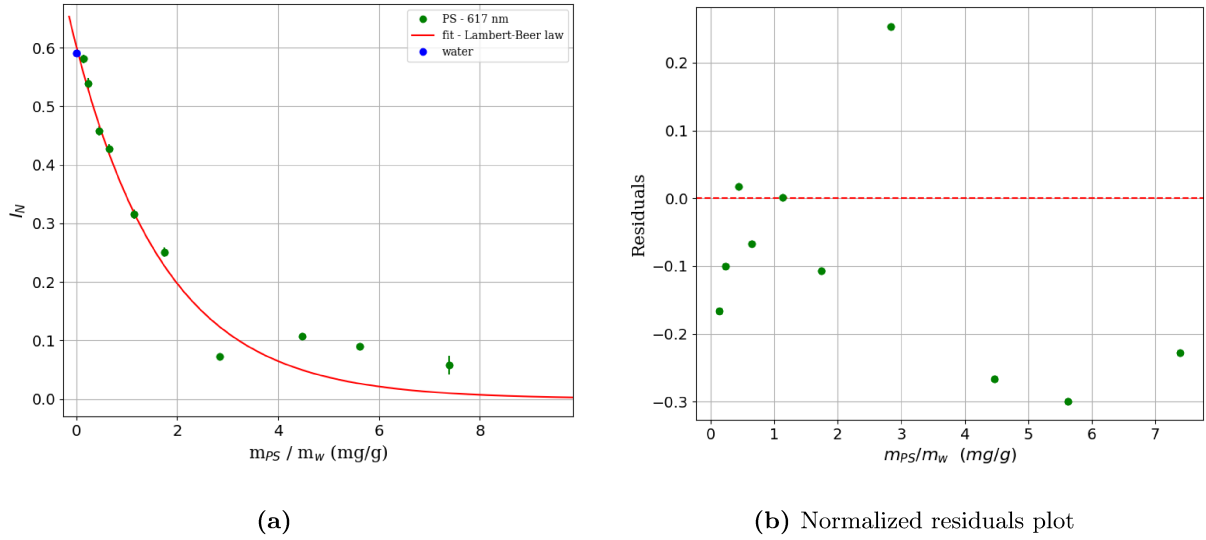
(a)

(b) Normalized residuals plot

Figure 4.1: Figure 4.1a represents the fit of I_N values computed from the PS-617 nm OT signals by using eq. 4.8, while figure 4.1b displays the correspondent normalized residuals.

a	$b \ (g/mg)$
0.59 ± 0.06	0.55 ± 0.09

Table 4.1: Parameters obtained by fitting the data of the PS-617 nm with equation 4.1.

(a)
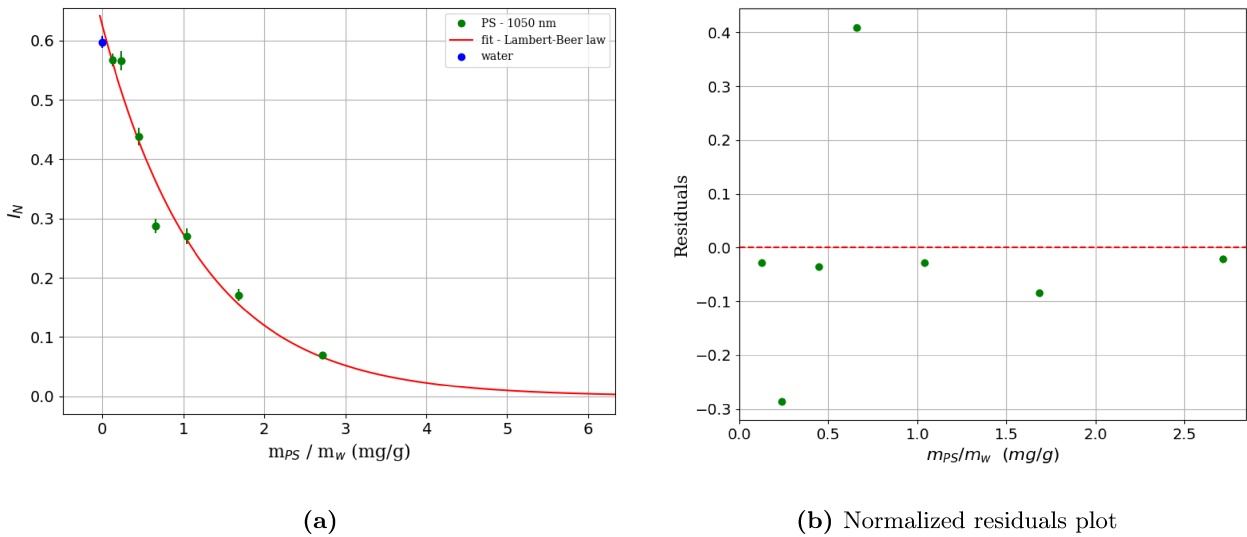

(b) Normalized residuals plot

Figure 4.2: Figure 4.2a shows the fit of I_N values computed from the PS-1050 nm OT signals by using eq. 4.1, while figure 4.2b displays the correspondent normalized residuals.

a	$b \ (g/mg)$
0.62 ± 0.03	0.83 ± 0.07

Table 4.2: Parameters obtained by fitting I_N values of the PS-1050 nm signals with equation 4.1.

4.2 Super-Poissonian model

Alexander B. Kostinski et al., in 2001, proposed an interesting approach to describe how, in presence of a medium containing a random collection of obstacles assumed to be not only statistically homogeneous but also spatially correlated, the attenuation with depth of incoherent radiation incident normally on the medium surface is often slower than exponential[79].

In a correlation-free medium, given well-precise assumptions defining a Poisson process (e.g. see [80][81]), a close connection exists between exponential extinction of photons (i.e. Lambert-Beer law) and Poissonian statistics. Relaxing the hypothesis of statistical independence between photon extinctions events, the spatial correlations among obstacles, that can be thought of as forming patches and voids throughout the medium, are introduced. Therefore, the distribution of absorbed photons deviates from the Poisson one, being characterized by *Super-Poissonian* fluctuations.

Given $p_n(x)$ the probability of having n photons absorbed in a given volume of a layer of depth x, the expression

$$p_n(x) = \frac{\overline{n(x)}^{\,n} \exp^{-\overline{n(x)}}}{n!},$$

(4.2)

where n is the random number of absorbed photons in the volume per unit time and $\overline{n(x)}$ is the mean count of extinction events over many realizations as a function of the depth x, describes a Poisson process that occurs in absence of spatial correlation of the obstacles in the medium.

In this case $\overline{n(x)}$ stays constant, meaning that the local mean concentration of obstacles c remains unchanged since $\overline{n(x)} = \beta x = \sigma c x$, with σ the extinction cross section per obstacle. However, when correlations are present the local mean number of absorbed photons $\overline{n(x)}$ must be regarded as a random variable. Therefore, to obtain the total distribution $p_n(x) = p(n)$, one must integrate over the distribution of local mean extinction rates $p(\bar{n})$, as follows

$$p(n) = \int_0^\infty p(n|\bar{n})p(\bar{n})d\bar{n} = \int_0^\infty \frac{\bar{n}^{\,n} \exp(n)}{n!} p(\bar{n})d\bar{n}$$

(4.3)

Setting [79]

$$p(\bar{n}) = \frac{1}{\beta x} \exp(-\frac{\bar{n}}{\beta x})$$

(4.4)

the result of eq. 4.3 is:

$$p(n) = p_n(x) = \frac{1}{1 + \beta x}\left(\frac{\beta x}{1 + \beta x}\right)^n.$$

(4.5)

To determine the probability of no extinction, the photon probability of transmission $p(0) = p_0(x)$ through a layer of depth x is required: it corresponds to

$$p_0(x) = \frac{N_{tr}}{N_{inc}} = \frac{1}{1 + \beta x}$$

(4.6)

with N_{tr} and N_{inc} stand for the number of incident and transmitted photons, respectively.

In the more general case, based on a Γ-distribution model, $p_0(x)$ is proportional to:

$$\frac{N_{tr}}{N_{inc}} \propto \frac{1}{(1 + \beta x)^q}$$

(4.7)

with q the parameter of Γ-function chosen as $p(\bar{n})$. This power-law attenuation of the incident radiation has a decreasing trend slower than the exponential one, predicted by applying the Lambert-Beer law $N_{tr}/N_{inc} = \exp(-\beta x)$. We therefore assumed to use a similar expression of I_N in function of c to interpolate the PS-617 nm and PS-1050 nm data according to the expression,

$$I_N(c) = \frac{a^{'}}{(1 + b^{'}c)^q}$$

(4.8)

with the idea that microparticles in the droplets, i.e. obstacles inside a medium, are spatially correlated and form patches and voids in the droplets. The fit parameters a' and b' are reported in table 4.3 and table 4.4, with correspondent fitted data and residuals plot illustrated in figure 4.3 and figure 4.4.

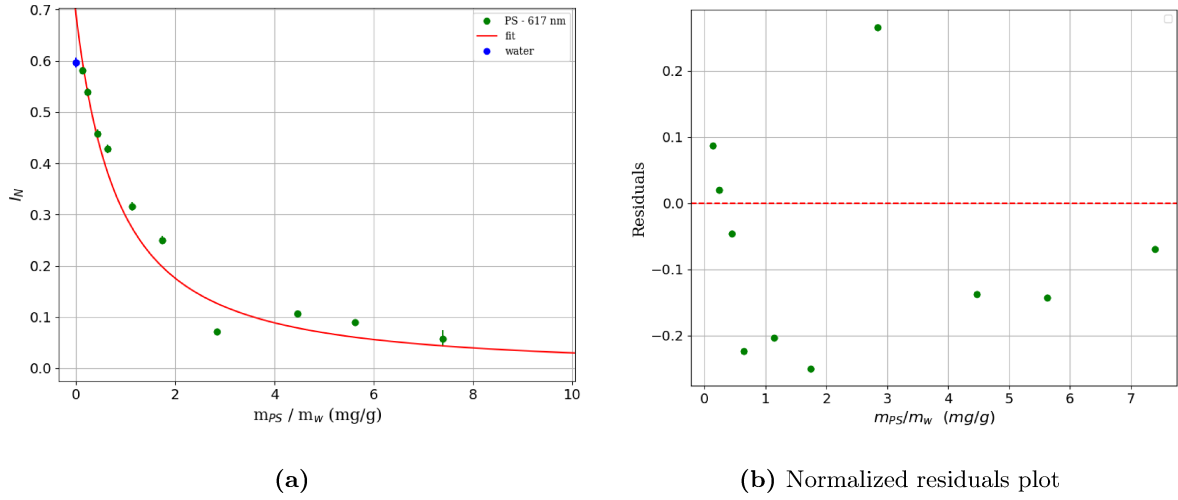**(a)**   **(b)** Normalized residuals plot

Figure 4.3: Figure 4.3a illustrates the fit of I_N values computed from the PS-617 nm OT signals by using eq. 4.8, while figure 4.3b represents the correspondent normalized residuals.

a'	b' (g/mg)	q
0.60 ± 0.03	0.4 ± 0.4	2 ± 2

Table 4.3: Parameters obtained by fitting I_N data of the PS-617 nm spheres with equation 4.8.

(a)   **(b)** Normalized residuals plot

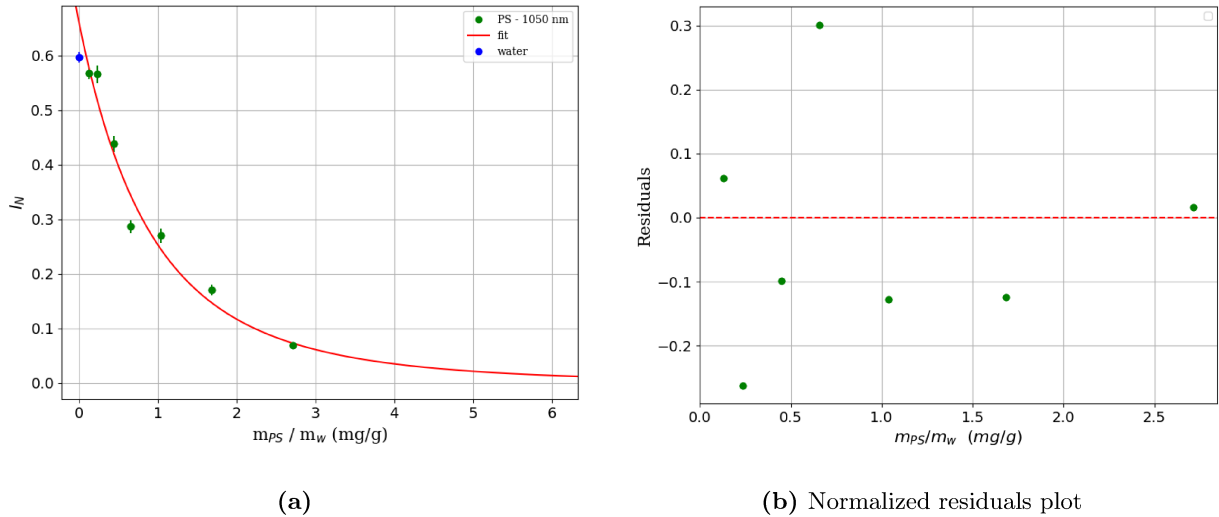**Figure 4.4:** Figure 4.4a illustrates the fit of I_N values computed from the PS-1050 nm OT signals by using eq. 4.8, while figure 4.4b represents the correspondent normalized residuals.

a'	b' (g/mg)	q
0.66 ± 0.06	0.3 ± 0.4	4 ± 4

Table 4.4: Parameters obtained by fitting I_N values of the PS-1050 nm particles with equation 4.8.

Applying this model (in the following: Super-Poissonian model), it is possible to see that residuals' plots do not display a clear trend. In the comparison with the Lambert-Beer model results, it seems that normalized residuals are more randomly distributed, suggesting a prevalence of stochastic errors and, consequently, a better description of the data acquired.

4.3 Super-Poissonian model corrected with a transmittance term

A far as the PS-340 nm and the PS-2500 nm microplastics are concerned, the points $I_N(m_{PS}/m_w)$ were interpolated introducing a correction to the Super-Poissonian model with the aim of describing its increasing trend at lower concentrations. This leads to the fitting curve expressed by:

$$I_N(c) = \frac{a'}{(1 + b'c)^q} \cdot X = \frac{a'}{(1 + b'c)^q} \frac{4e' \cdot (c - d') + 4k'}{(1 + e' \cdot (c - d') + k')^2} \tag{4.9}$$

The term X added in equation 4.9 to equation 4.8 has been obtained resorting to a sort of "refractive index matching condition" (see [82]) including either the lithium niobate crystal, i.e the substrate the opto-microfluidic platform is made of and the aqueous solution containing PS-particles. In this configuration it is possible to take into account the aforemenioned increase of the transmitted light realizing a sort of lens-effect.
In particular, given $R = [(1 - n_1/n_2)/(1 + n_1/n_2)]^2$ the equation that describes the backward reflection of light from the interaction of the laser with the droplets predicts that the transmittance is expressed as follows

$$T = 1 - R = (4n_2/n_1)/(1 + n_2/n_1)^2. \tag{4.10}$$

Under this hyphothesis and following the approach proposed in [82], it results that $n_1 = n_{LiNbO_3}$ while $n_2 = (c \cdot n_{PS} + (1 - c) \cdot n_w)$ can be interpreted as an effective refractive index of the overall aqueous solutions where $n_w = 1.33$ and $n_{PS} = 1.59$ are linearly combined with respect to concentration $c = m_{PS}/m_w$.
Including n_1 and n_2 in equation 4.10 and introducing the fit parameters $e' = 4/n_{LiNbO_3}(n_PS - n_w)$, $k' = n_w/n_{LiNbO_3}$ and d' to generalize the description of the data considered, X is thereby obtained.
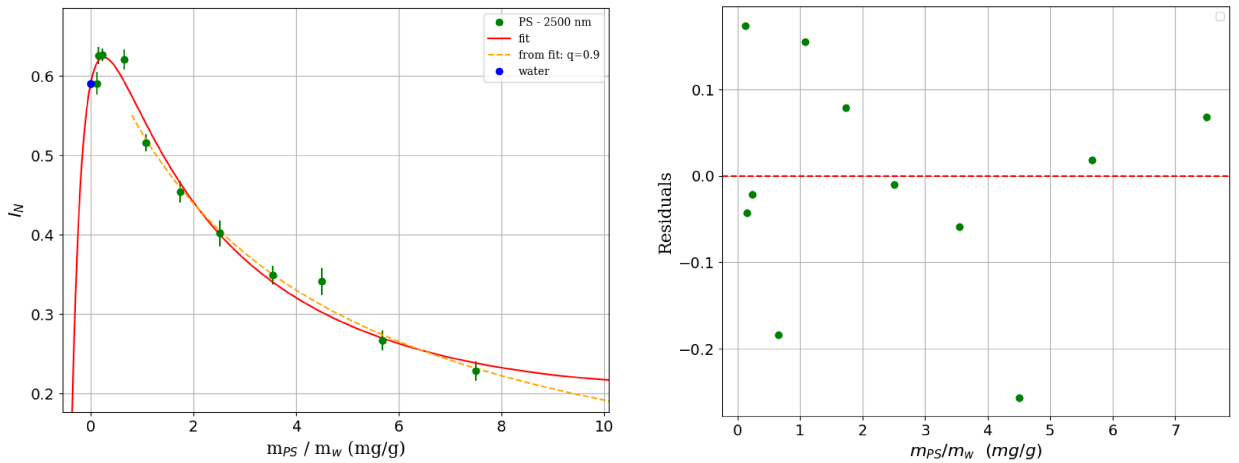
(a) Fit 2500nm   (b) Normalized residuals plot

Figure 4.5: Figure 4.5a shows the fit of I_N values computed from the PS-2500 nm OT signals by using eq. 4.9, while figure 4.5b displays the correspondent normalized residuals.

In figure 4.5a the fit (red curve) of I_N values obtained from PS-2500 nm particles with equation 4.9 is reported. The parameter q was formerly derived by interpolation of the points placed on the decreasing part of the distribution with the equation 4.8. It gives the orange dashed curve as best fit with $q = 0.9 \pm 0.2$. The latter value has been then used to compute the overall fit, giving as best parameters'

estimations those reported in table 4.5 as a result of a by least-squares minimization.

a'	b' (g/mg)	d (mg/g)	e' (g/mg)	k'
~ 0.63	$\sim$ -0.041	~ 0.50	~ 1.6	~ 1.4

Table 4.5: Parameters obtained by fitting I_N data of the PS-1050 nm with equation 4.9.

Although the number of parameters to estimate is large if compared to the amount of data available, it is worth mentioning that the distribution of normalized residuals seems to be stochastic as seen in figure 4.5b. The curve obtained is a promising description of the results provided by the interaction of the PS-2500 nm particles with laser light.

4.4 Modelling and discussions

The considerations just discussed for the PS-2500 nm particles cannot be applied directly to the case of PS-340 nm spheres. It is evident that in the fit illustrated in figure 4.6a, the Super-Poissonian model corrected with a transmittance term can not describe the trend of I_N values for the concentrations m_{PS}/m_w here employed.
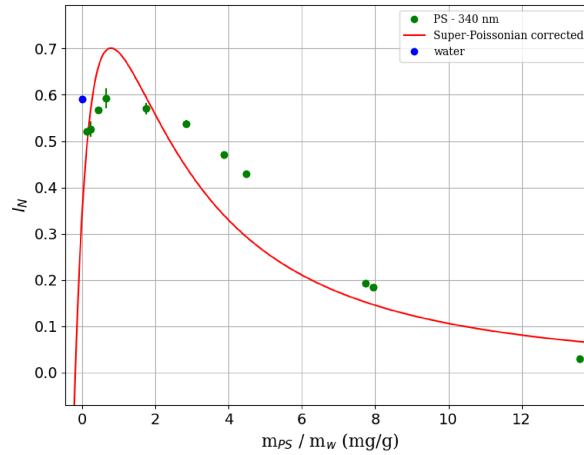
(a)

Figure 4.6: Evaluation of the curve given by equation 4.9 considering the I_N trend for PS-340 nm particles.

In the framework of an electromagnetic plane wave scattered by a homogeneous sphere can be explained by recalling the theory of Rayleigh scattering applied to small, dielectric (non-absorbing), spherical particles. [1]. According to this theory, the total extinction cross section is assumed to be equal to the scattering one that is, $\sigma_{ext} = \sigma_{scat}$. In particular, σ_{scat} scales as α^6 where α is the dimensionless size parameter given by the expression

$$\alpha = \frac{2\pi R}{\lambda},$$

where R is the spherical particle radius, and λ is the relative scattering wavelength defined as

$$\lambda = \frac{\lambda_0}{m_0},$$

---

[1]Mie scattering theory encompasses the general spherical scattering solution (absorbing or non-absorbing) without a particular bound on particle size.

where λ_0 is the incident wavelength with respect to vacuum, and m_0 represents the refractive index of the medium surrounding the particles [68].

The criteria for Rayleigh scattering is that $R/\lambda \leq 0.05$ [69]. In the case of PS-340 nm particles, dielectric and thus non-absorbing, $R/\lambda \sim 0.43$ with $R = 170\,nm$, $\lambda_0 = 532\,nm$ and $m_0 = n_{water} = 1.33$. Since the condition $R/\lambda \leq 0.05$ is not fulfilled, the more complex Mie scattering formulation has been used, resorting to the result that gives

$$\sigma_{scat} \approx \sum_{l=0} (\alpha)^{2(2l+1)}, \tag{4.11}$$

where the sum expresses an infinite series of multipole expansion of order l.[69][70].

As a consequence, when using the Lambert-Beer law, it results that

$$dI = -\rho \sigma_{scat} I ds, \tag{4.12}$$

with $\rho = N/V$ equal to the spheres volumetric density, that describes the attenuation of the light incident on a medium of depth s containing a collection of obstacles. In our case the medium is a water droplet with PS-340 nm particles, i.e. the factor $\rho \sigma_{scat}$ can been expressed as a function of the concentration $c = m_{PS}/m_w$. It results that starting from

$$\rho \sigma_{scat} \simeq \frac{N}{V}(\alpha^2 + \alpha^6 + \alpha^{10} + ...) = \frac{N}{V}\{(kR)^2 + (kR)^6 + (kR)^{10} + ...\}, \tag{4.13}$$

where N is the number of particles in the droplet, V the droplet volume and $k = 2\pi/\lambda$ the wave vector, since

$$c(N) = m_{PS}/m_w = \frac{\rho_{PS}}{V} N \frac{4}{3}\pi R^3, $$

and in the hypothesis that the dimension of the spheres interacting with light is dependent on N. Since $R \rightarrow R(N)$, equation 4.13 scales as:
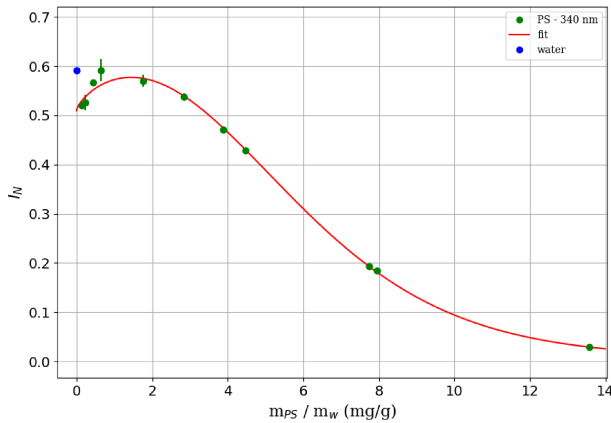
$$\rho \sigma_{scat} \propto Bc^{2/3} + Dc^2 + Ec^{10/3}, \tag{4.14}$$

consequently by assuming $R(N) \propto c^{1/3}(N)$ and absorbing all the constants in the parameter B, D and E.

Introducing equation 4.14 in 4.12 the solution of the differential equation is given by the expression:

$$I(c) = I_N(c) = A\exp(-Bc^{2/3} - Dc^2 - Ec^{10/3}), \tag{4.15}$$

where the intensity $I(c)$ can be evaluated by means the integral $I_N(c)$

(a)
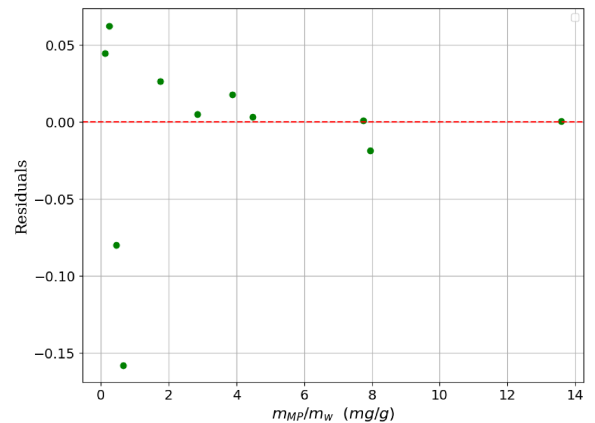
(b) Normalized residuals plot

Figure 4.7: Figure 4.7a displays the fit of I_N values computed from the PS-340 nm OT signals by using eq. 4.15, while figure 4.7b represents the correspondent normalized residuals.

A	B $[(g/mg)^{2/3}]$	D $[(g/mg)^2]$	E $[(g/mg)^{10/3}]$
0.509 ± 0.007	$- 0.15 \pm 0.01$	0.031 ± 0.002	$- 0.00034 \pm 0.00004$

Table 4.6: Parameters obtained by fitting I_N data of the PS-340 nm with equation 4.15.

Figure 4.7a illustrates the fit of $I_N(c)$ experimental values while table 4.6 reports the best estimations of the fit parameters, obtained by least-squares minimization. It is interesting to note how B and D, associated with $c^{2/3}$ and c^2 respectively, are the most relevant parameter of the exponential term, meaning the evaluation of the multipole expansion series at the second-order seems to be a reasonable approximation.

The distribution of the normalized residuals represented in figure 4.7b shows an absence of a clear trend, suggesting a prevalence of random errors; therefore, although the approximations applied in the calculations, the model here proposed provides an acceptable description of the data acquired.

Applications

The results of the analysis presented in chapter 3 are used in this Chapter to test the device with different material microplastics (PMMA).A Comparison between PMMA and PS particles (section 5.1) will be presented by introducing as dispersed phase a mixture of PS-340 nm and PS-1050 nm spheres solutions at the same concentration (section 5.2). Finally, by properly illuminating an iron-doped Fe:LN sample put on top of the opto-microfluidic device we were able to create an electric field induced by inhomogeneous space charges produced by the photovoltaic effect. We consequently explored the impact of this induced electric field on the moving droplets. In particular, we were able to measure its effect on droplets in terms of variation of the MP length and velocity (section 5.3)

5.1 PMMA particles

In order to evaluate the capability of optical apparatus to identify MP particles different from the PS ones, water droplets containing PMMA spheres with a diameter of 2500 nm (in the following: PMMA-2500 nm) have been produced and analyzed. Special care was devoted to evaluate their optical transmission signals with respect the PS-2500 nm ones.

(a) PS - C4.2.1   **(b)** PMMA-C4.2.1
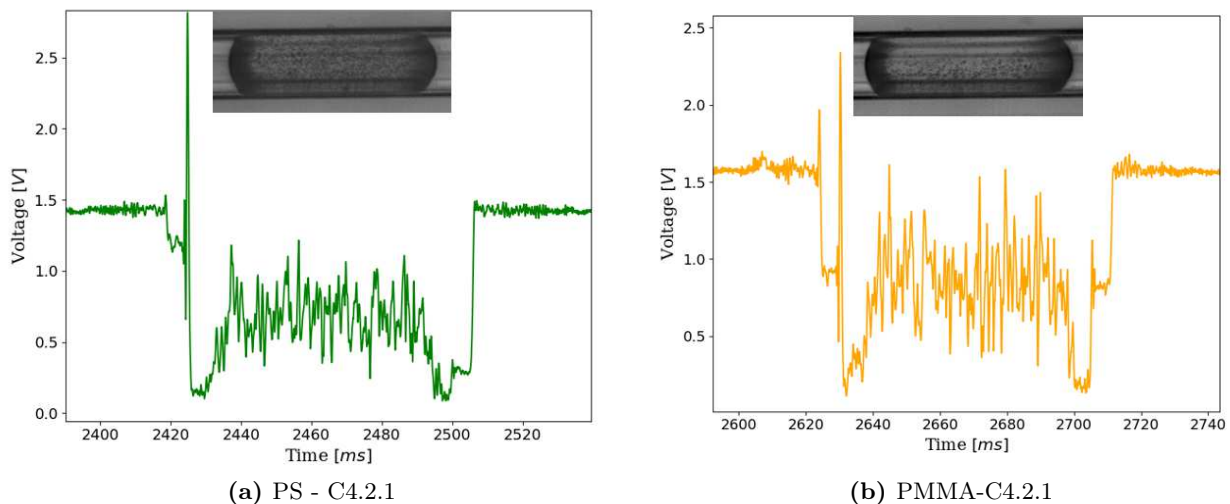
Figure 5.1: Comparison between the signal plateau produced by a droplet containing PS-2500 nm particles, at concentration C=2.5±0.1 mg/g, (5.1a) and the one detected by a droplet obtained flowing a PMMA-2500 nm solution at the same C=2.5±0.1 mg/g (5.1b). The different distribution of the spheres within the two solutions is visualized through the screenshots of a droplet part of the sequence generated by each of them.

A comparison between a droplet plateau signal from PS-2500 nm spheres measurement (figure 5.1a) and

one generated by PMMA-2500 nm particles is considered. In the latter, peaks intensity characterizing the plateau's fluctuations are more marked than PS case, in which, moreover, the growth of the signal starting from the first absolute minima appears smoother.

It is worth saying that PMMA dispersed phase seemed to be affected by inhomogeneity in microplastics concentration. This is reported in figure 5.1b, that shows an unbalanced particles distribution within the droplet.

The aforementioned inhomogeneity is especially visible at $m_{MP}/m_w > 5\,mg/g$, both in the initial phase of the droplets' production, when the dispersed phase just comes into the microchannel (see figure 5.2a), both when the solution is running out (see figure 5.2b).
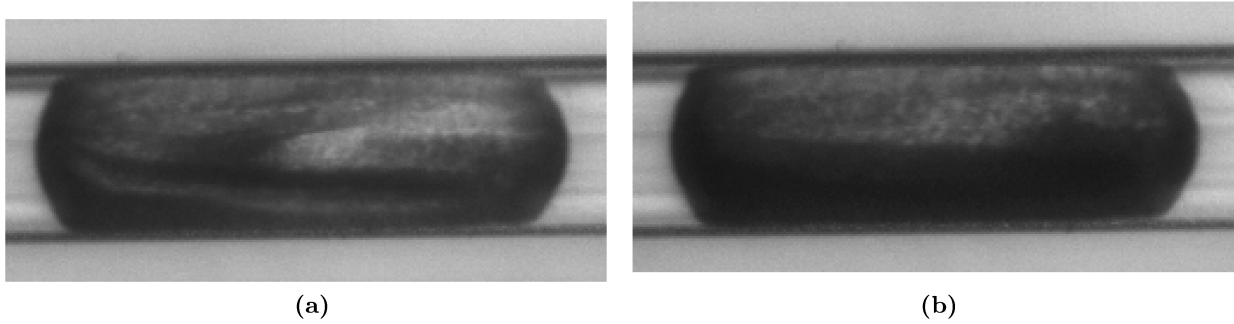

(a)   (b)

Figure 5.2: Representation of the particles concentration inhomogeneity that affects PMMA droplets. Figure 5.2a shows a droplet produced just after water with PMMA particles at C=7.55±0.08 mg/g came into the chip; figure 5.2b, instead, illustrates a droplet when the dispersed phase at that concentration is running out.

The measurements performed were then exploited to test the ability of the parameters I_N and m to sort and distinguish micro plastics of different materials.

Figure 5.3 illustrates the comparison between I_N values, as a function of the particles' concentration, obtained from PS-2500 nm and PMMA-2500 nm transmission signals.
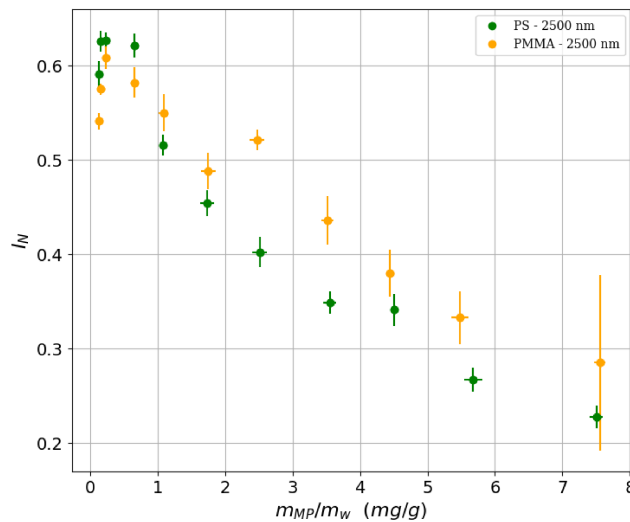
Figure 5.3: Comparison between I_N trends describing the transmitted light by the PS-2500 nm particles (in green) and the PMMA-2500 nm ones (in orange).

First of all, it is important to stress how the distribution of PMMA data, see figure 5.3 and figure 5.4, with the latter illustrating m and σ_m, traces that of the PS particles. These findings confirm the sensitivity of estimator I_N, as well as m and σ_m, to micro plastics' dimension, because both types of spheres have the same diameter.

Moreover it is possible to note that at lower concentrations (i.e. meaning below 2 mg/g) trends are undistinguishable. This means that the experimental setup is not sufficiently effcient to detect differences between the two OT signals produced by the materials, separately.

On the contrary, in the range of 2-4 mg/g the different response of droplets' content to light interaction is appreciable. The higher transparency of PMMA particles than PS ones should provide under the same experimental conditions, a more intense light signal, resulting in higher I_N values. This is confirmed as evident by observing the behavior of PMMA and PS curves at the same concentration. These promising results, if confirmed by further investigations, open a perspective in developing a new type of detection sensibility of the opto-microfluidic device that can focus either on the microplastic identification and quantification. In order to validate this study, a set of repeated measures under different experimental conditions should be carried out for both plastic types employed either with the same solutions analyzed in figure 5.3 as well as in wider composition range. As a matter of fact, data suggest that at higher concentrations, PMMA and PS I_N values are compatible and therefore possible systematic errors can be present.
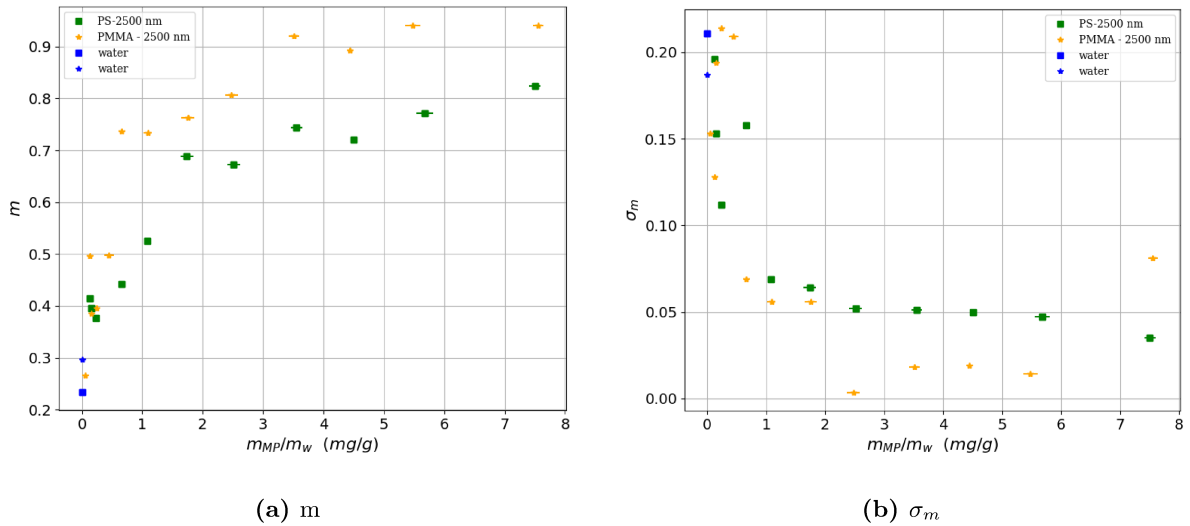

(a) m   (b) σ_m

Figure 5.4: Figure 5.4a shows the comparison between m parameters obtained from the analysis of PS-2500 nm and PMMA-2500 nm microplastics, while figure 5.4b the correspondent σ_m trends. The blue points represent the water base signals detected on the same day of the spheres data acquisition.

Similar considerations about the statistics of the results acquired are valid also evaluating the behaviors of the parameters m and standard deviations σ_m, reported in figure 5.4a and figure 5.4b respectively. Considering only the region $m_{MP}/m_w > 2$ mg/g, it is evident how the pair of curves, both for m and σ_m, are well distinguished. The droplets signals referred to PMMA particles are characterized by higher fluctuations and quicker decrease of σ_m as it emerges by observing the trends in figure 5.4b.

Once again, the hypothesis that, in more diluted aqueous solutions, local concentration increases due to particles patches formation affect the signal stability can be seen also for the PMMA-2500 nm, since σ_m values below 1 mg/g are very high.

5.1.1 Reproducibility test

To verify the performance of the optofluidic device to distinguish PS and PMMA microplastics, a test has been performed by detecting the OT signal generated by droplets produced with solutions having concentration C6, C7 and C8 (see table 3.3) respectively. They were prepared ex novo from scratch both for PS and PMMA 2500 nm particles. Limiting the analysis to the I_N parameter, the results generated by these new solutions are reported in figure 5.5, where a comparison with the integrals plotted in figure 5.3 is presented. In this case PS (figure 5.5a) and PMMA (figure 5.5b) curves have been separately reported for the sake of clearness.

As far as the PS-2500 nm microparticles are concerned, the results provided by the new solutions (light-green) follow a decreasing trend, confirming the already observed dependence on MP concentration. However, I_N values are higher than the correspondent ones at the same concentration analyzed in section 3.1.1. This evidence suggests that a possible upper limit of a tolerance range, bounded below by the dark green curve, could be present. As a consequence, the description of I_N dependence on m_{MP}/m_w>1 mg/g could not be simply modelled by a monotone decreasing trend, as previously supposed. The new C6 I_N value, in fact, suggests that I_N trend could follow a curve characterized by a possible enhancement around m_{MP}/m_w=2.5 mg/g.

Such behavior, given the distribution of the points in figure 5.5b, can not be excluded in the case of PMMA particles, either. Further repeated measurements for both materials, with the same solutions investigated in figures 5.5, could assist in identifying the curve better describing the decreasing part of the PS-2500 nm and PMMA-2500 nm integrals trend.

It is interesting to note that, for both plastic types, the integral values correspondent to the pair of points referred to concentration C8 are compatible, although obtained from solutions produced independently. This observation worth to be emphasized, since the new C8 solutions, as well as the original ones, have been produced, both for PS and PMMA plastic, by diluting the respective 2500 nm particles directly extracted from the vial delivered by the producer. On the contrary, C6 and C7 solutions have been realized by subsequent C8 dilution. Consequently, the possible introduction of further systematic errors due the preparation procedure of the solutions could have determined the marked difference between the original C6 and C7 I_N values and the correspondent new ones. This hypothesis, however, would suggest that the optical apparatus employed could be so sensitive to detect even small variations of concentration, ensuring in this way a considerable level of reproducibility.
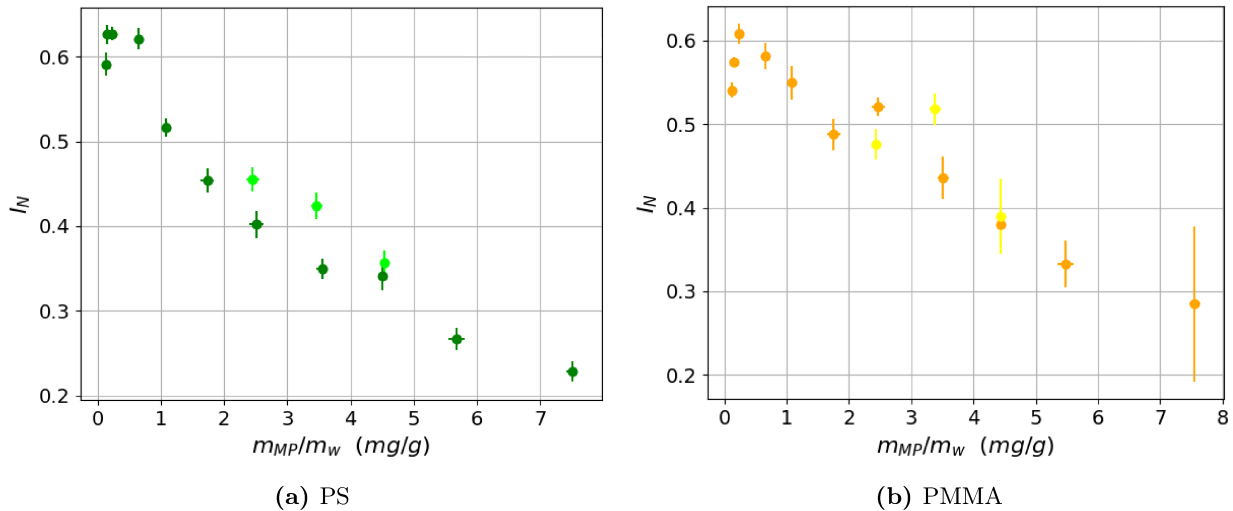

(a) PS   **(b)** PMMA

Figure 5.5: Figure 5.5a illustrates the comparison between the new PS-2500 nm solutions integral values (light green) and the PS-I_N trend described in figure 5.3. The same holds for figure 5.5b, where instead PMMA-2500 nm particles data are reported, with new I_N points depicted in yellow.

Figure 5.6 illustrates the direct comparison between the discussed new I_N values. The first important finding to point out is that (see figure 5.3) the results referred to PMMA particles describe, regardless of the concentration, an OT signal more intense than the one generated by PS microspheres, confirming the trend of the original measurements.

To better evaluate what is depicted in figure 5.6, table 5.1 is considered. It reports, for the nominal concentrations C6, C7 and C8, the differences ΔI_N and ΔI_N^{new} between the PMMA integral and the correspondent PS one for the original results, shown in figure 5.3, and the new ones, respectively.
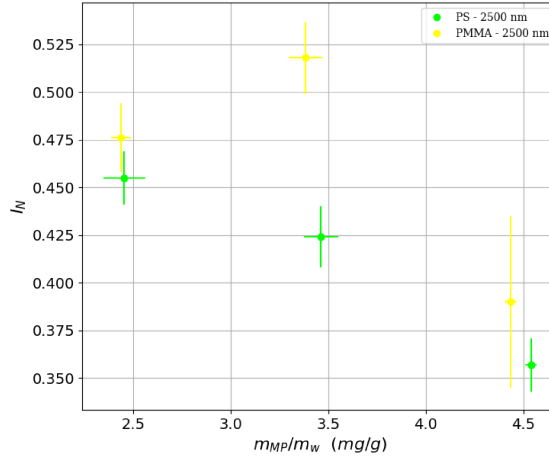
Figure 5.6: The graph provides the comparison between trends of I_N points derived by analyzing new PS-2500 nm solutions (green light) and new PMMA-2500 nm ones (yellow).

The finding that ΔI_N and ΔI_N^{new}, for C7 and C8, have extremely similar values proves the reproducibility of the estimation of the integral difference. This evidence could demonstrate the ability of the experimental apparatus to go beyond the aforementioned systematic errors introduced by the solutions production (in particular for the dispersions obtained by subsequent dilution, as in the C7 case).

C (mg/g)	ΔI_N	ΔI_N^{new}
C6	~ 0.119	~ 0.021
C7	~ 0.087	~ 0.094
C8	~ 0.039	~ 0.033

Table 5.1: Difference between PMMA and PS particles integral values, evaluated at the considered concentrations, in the case of previous data (ΔI_N) and new computed results (ΔI_N^{new})

	HTL pipette			VWR pipette	
Volume (mL)	Weight (g)	$\Delta\%$	Volume (mL)	Weight (g)	$\Delta\%$
	1.2345	23.45		0.1228	22.8
	1.1832	18.32		0.1232	23.2
1	1.1934	19.34	0.1	0.1305	30.5
	1.1949	19.49		0.1224	22.4
	1.1934	19.34		0.124	24.0

Table 5.2: Results of the test performed on the pipettes used to produce the microparticle solutions. HTL pipette has a range of 100-1000 μL, while VWR pipette, devoted to microplastic spheres extraction, allows taking a volume between 20 and 200 μL. Masses have a standard deviation of 0.1 mg while $\Delta\%$ varies of $\pm 0.01\%$ and $\pm 0.1\%$ for the HTL pipette and the VWR pipette respectively. Being the models series number of the latter not available, error on the MilliQ volume picked up has not been computed.

The reliability of the two micro-pipettes employed to produce all the PS solutions has been tested by taking and weighting multiple MilliQ water samples (density ρ=1 kg/dm^3): five of nominal volume 1 mL (HTL pipette) and 5 of nominal volume 0.1 mL (VWR pipette). Results are reported in table 5.2. The impact of the pipette on the real water volume extracted, compared to the nominal one, is evident. On average the HTL pipette have taken 20$\pm$2 % more of MilliQ while the VWR one an extra 24$\pm$3 %.

Since the latter pipette was devoted to microparticles, no controllable variations in the concentration values with respect to the expected ones have probably affected the actual dependence of some I_N on m_{MP}/m_w.

Although at the moment the reproducibility tests have been restricted to just three new solutions, the optical device provided anyway trends of the correspondent integral parameters. Especially in the case of PS particles the previously analyzed I_N dependencies have been confirmed (see figure 5.3). Moreover, the higher intensity of the OT signal generated by PMMA solutions with respect to the PS ones at the same concentration, is observed again thus representing a promising result.

5.2   Mixture of PS-340 nm and PS-1050 nm

A 1:1 mixture of PS-340 nm and PS-1050 nm solutions (in the following: mixture) with the same particles' concentration C=0.65 mg/g [1] has been produced and tested as dispersed phase through the optofluidic platform. The signals relative to the first sequence's droplet containing the mixture have been compared to the one produced individually by the PS-340nm and PS-1050nm. The same averaged water base signal $V_{avg,w}$ has been taken as a reference, as shown in figure 5.7.
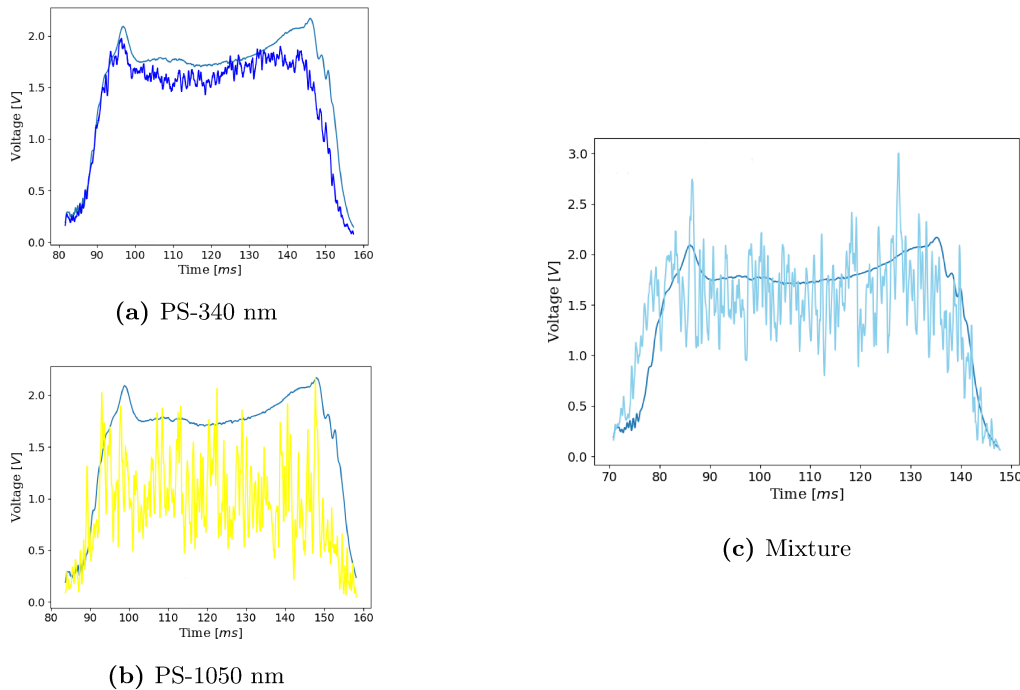

(a) PS-340 nm

(b) PS-1050 nm

(c) Mixture

Figure 5.7: Figure 5.7a illustrates the overlapping between the OT signal produced by the first sequence's droplet containing PS-340 nm microplastics with the averaged water base signal $V_{avg,w}$. The latter is represented also in figure 5.7b and figure 5.7c, where it is put into relation with the first sequence's droplet signal acquired from PS-1050 nm particles and mixture dispersed phases, respectively.

Figure 5.7c illustrates the signal of the droplet containing the mixture (see light blue label). It is possible to note that the fluctuations characterizing the droplet plateau are more similar to those present in figure 5.7b, referred to PS-1050 nm particles. Since the concentration of PS-340 nm and PS-1050 nm solutions are the same, most of the information driven by transmitted light is due to the larger diameter particles.

This evidence is clearer in figure 5.8 where a comparison between the power spectra is presented using the same water signal as a reference. It is interesting to see how the intensity and shape of the mixture's power spectrum peaks (in light blue) resemble the ones describing the frequency content of PS-1050 nm

---

[1]NdA: C3=0.65 ± 0.01 and C3=0.66 ± 0.01 for the PS-340nm and PS-1050 nm were used respectively

microplastics (in yellow). This result confirms the stronger dependence of mixture signal instabilities on 1050 nm particles than the 340 nm ones.
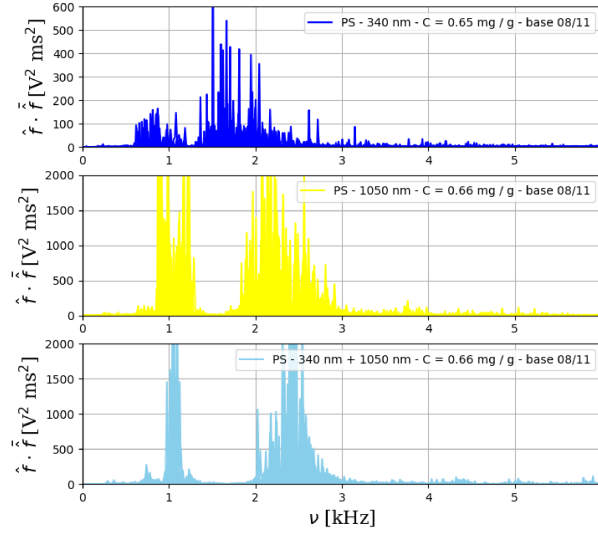

Figure 5.8: Representation of the power spectrum associated with the PS-340 nm particles (in blue) solution having C=0.65 mg/g, of the power spectrum computed from the signal generated by the PS-1050 nm spheres (in yellow) at C=0.66 mg/g and of the one of the correspondent mixture (in light blue) obtained mixing same quantities (2 ml) of the just mentioned PS-340 nm and PS-1050 nm solutions. All of them are derived employing the same water base signal $V_{avg,w}$, the same illustrated in figure 5.7

The different contribution to the mixture signal by the two types of spheres has been deeper investigated evaluating the integral I_N and the parameter m obtained separately from the three droplets sequence signals produced by PS-340 nm, PS-1050 nm and mixture dispersed phases respectively.
In particular, this analytical analysis passed through the solution of the following system of two equations:

$$\begin{cases} a \cdot I_{N,340} + b \cdot I_{N,1050} = I_{N,mixture} \\ a \cdot m_{340} + b \cdot m_{1050} = m_{mixture} \end{cases}$$

where the idea was to consider the mixture integral $I_{N,mixture}$ as a linear combination of the integral $I_{N,340}$ and $I_{N,1050}$, obtained analyzing the PS-340 nm and PS-1050 nm signals, weighted by the coefficients a and b respectively. The same holds for the parameter $m_{mixture}$ through m_{340} and m_{1050}.
The solution has provided $a \approx 0.27$ and $b \approx 0.74$. It is possible to note that $a + b \approx 1$, as if the 340 nm particles contributed $\sim 27\%$ to the mixture signal while 1050 nm spheres weighted for the $\sim 74\%$, justifying what was qualitatively observed in the power spectra.
This approach can be applied when components in mixtures are not interacting. In this case, in fact, each component contributes separately depending on its relative abundance. This approximation does not exclude the existence of interrelation between particles having different dimensions combined in a mixture. Work is in progress to quantify nonlinear effects that may occur when particles interactions arise.

In order to further improve the microplastics detection we carried out a feasibility study to integrate a stage able to apply a local electric field to the flowing droplets. We exploited the so-called virtual electrodes approach, i.e. the realization of electrodes by suitable illumination so that an electric field is generated with the proper geometry to interact with the droplets. In the next section we will describe how these virtual electrodes have been designed by exploiting the photovoltaic effect of $LiNbO_3$ and how we integrated this stage with the opto-microfluidics one already discussed in section 1.2. Microplastics can show a dipole moment, either due to the plastic composition or stressed induced effect.

As a consequence, an electric field is expected to align or interact with them and affect the relative detection. No data ara available in the literature about this aspect. As a consequence in this work a preliminary study has been carried out to see whether the presence of an external electric field can be exploited to enhance the micro-plastics detection and identification

5.3   Effects of a space-charge electric field on droplets of MP solution

The photovoltaic properties of lithium niobate (see section 1.2.1) can be used to create a local electric field. It can be significantly enhanced by local doping of the material, especially in the case of an iron-doped lithium niobate (Fe:LiNbO$_3$, Fe:LN) sample. In fact, considering a pure LiNbO$_3$ substrate, the space-charge electric field E_{sc} induced by a uniform light illumination ranges from 0 to 10^4-10^5 V/m, while in presence of a 0.01% mol Fe:LN z-cut crystal it increases up to 10^6 V/m. In [15] the effects of E_{sc}, generated by illuminating a z-cut Fe:LiNbO$_3$ sample (reduction degree R= $\frac{N_{Fe2+}}{N_{Fe3+}}$ = 0.05±0.01) properly integrated in the same optofluidic platform employed in this work, are evaluated on the length and velocity of MilliQ droplets.

The same analysis was performed in this study on droplets produced by injecting in the microfluidic circuit solutions of water and microspheres as dispersed phase. The optofluidic platform adopted for the measurements is the same illustrated in figure 1.14, but with the integration of the aforementioned Fe:LN sample. As shown in figure 5.9a, it was appropriately fixed to the top cover of the chip orienting the +z face toward the glass. The light illumination of the Fe:LN sample is provided by a solid state laser ($\lambda = 532\,nm$) with a power $P = 65.0$ mW measured in close proximity to the chip with a semiconductor power sensor connected to FieldMaxII-TO power meter (Coherent Inc., Santa Clara, CA, USA). The scheme of the Fe:LN cover illumination setup is reported in figure 5.9b).

All the details about the generation of the photo-induced space-charge field and its dependence on Fe:LiNbO$_3$ crystal characteristics (e.g., N_{Fe2+}, N_{Fe3+}) and orientation can be found in [15] and [83]. Moreover, in the former a brief feasibility test on the not-complete-screening of the induced field due to the glass cover is also presented while in the latter a detailed study on dielectro- and electrophoresis effects on the trapping of microparticles due to the Fe:LiNbO$_3$ evanescent photo-induced field is reported.

The photo-induced field E_{sc} is generated by illuminating the Fe:LN cover at the level of the microfluidic channel with the spot aligned with the employed MZI waveguide.

(a)   (b)
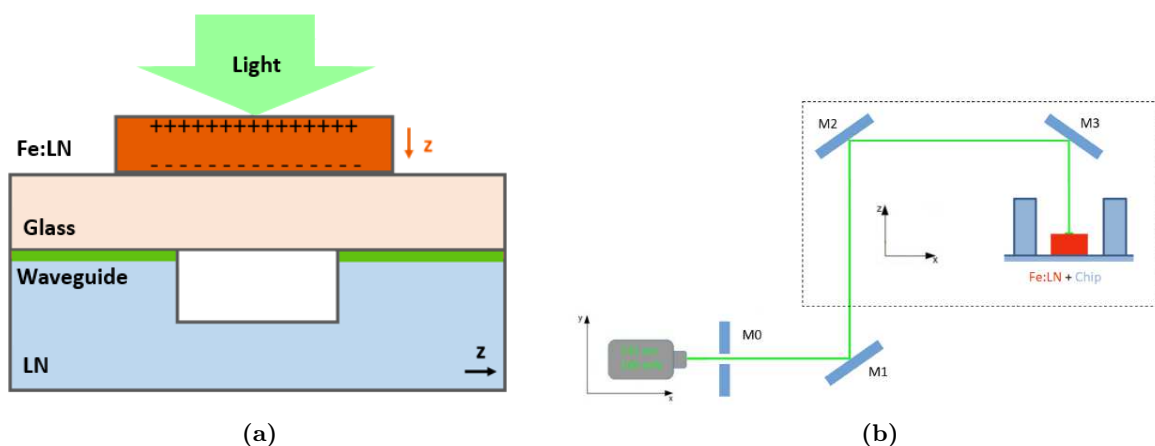
Figure 5.9: Figure 5.9a illustrates a schematic representation of the integration on the optofluidic chip, that is represented in a section perpendicular to the main microchannel and hence to droplets flowing, of the iron-doped Fe:LN sample; the latter is illuminated by the optical apparatus sketched in figure 5.9b, where M0, M1, M2 and M3 are mirrors.

In order to verify the actual presence of the photo-induced field, MilliQ droplets have been initially produced and their lengths and velocities have been measured before switching on the photovoltaic

effect (in this configuration the E_{SC} is therefore zero because no illumination of Fe:LN crystals has been started. The acquisition at $t = 0$ minutes is in fig. 5.10a). The chosen fluxes were $Q_c = 10\,\mu\text{L}$ / min and $Q_d = 8\,\mu\text{L}$ / min. We switched on the photovolatic effect by starting to illuminate the sample, and lengths and velocities measurements were performed at time instants $t_i = 5, 10, 15, 20, 25, 30, 35, 40, 45$ minutes. Following the same protocol used in [15], each acquisition at time t_i has a time duration Δt_i such that at least 100 droplets are detected. Each time instant t_i corresponds to the middle point of Δt_i and is used to label the i-th acquisition.

The droplets average length of each acquisition was computed and the obtained results as a function of time are reported in the plot shown in figure 5.10a, in which the chosen fitting function is in the form of:

$$L = L_0 + \Delta L \left(1 - e^{-t/\tau}\right), \tag{5.1}$$

where L_0 is the base average length at $t = 0$ minutes, when no laser beam is impinging on the iron-doped sample and therefore no electric field is present, and ΔL is the elongation established in the typical time τ. The fit parameters are reported in table 5.3, while figure 5.10b shows the correspondent residuals plot.

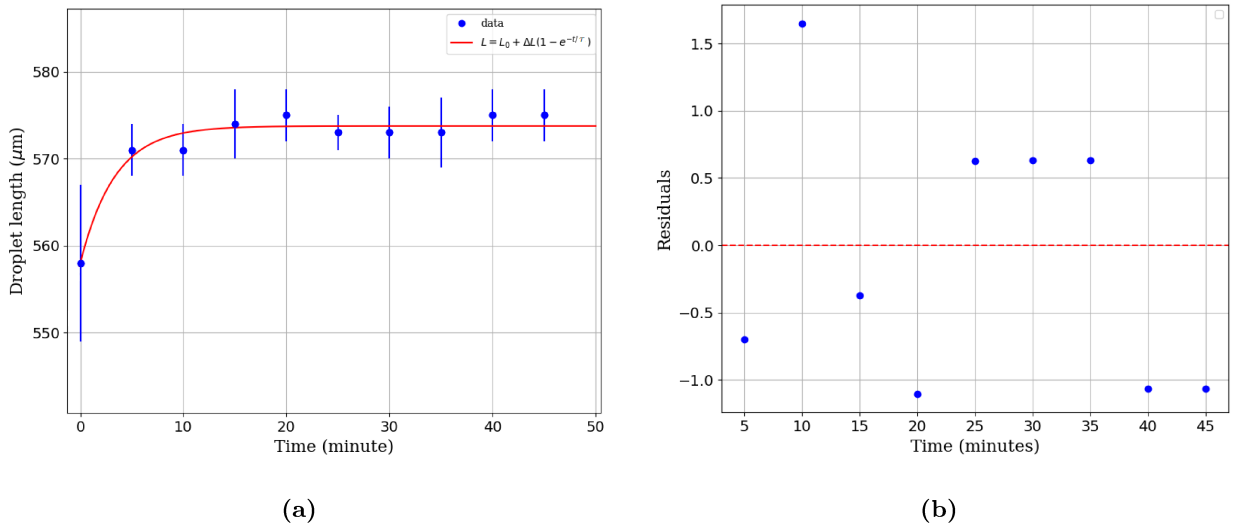(a)   (b)

Figure 5.10: Fitting of the average lengths by using equation 5.1 is presented in 5.10a, while the plot in 5.10b shows the correspondent residuals.

L_0 (μm)	ΔL (μm)	τ (minutes)
558 ± 9	15.7 ± 0.4	3.33 ± 0.05

Table 5.3: Parameters obtained by fitting the data with equation 5.1

The trend represented by eq. 5.1 has a time dependence similar to the one observed in E_{sc} and the obtained elongation ΔL is compatible with the results in [16] and [15], suggesting the establishment of the photo-induced field acting on the droplets [2]. Although the normalized residuals at time $t \geq 25$ minutes seem not to follow a random behaviour, the very low dispersion affecting the aforementioned lengths for $t \geq 5$ minutes further confirms the establishment of E_{sc}.

After 45 minutes from the beginning of the laser illumination, the dispersed phase was changed from pure MilliQ water to a solution of PS-617 nm particles and MilliQ water: the two tested solutions were C3=0.64±0.05 mg/g and C4=1.14±0.07 mg/g. Two additional acquisitions for the two different solutions were then performed with the laser light still impinging on the Fe:LN sample.

A comparison between the average length and velocity of droplets produced by employing the same

---

[2]L_0 value's dispersion may depend on flux instabilities.

solutions in the presence and in absence of the photo-induced field is presented both in figure 5.11 and in table 5.4. The acquisitions without the cover illumination were performed on different days.
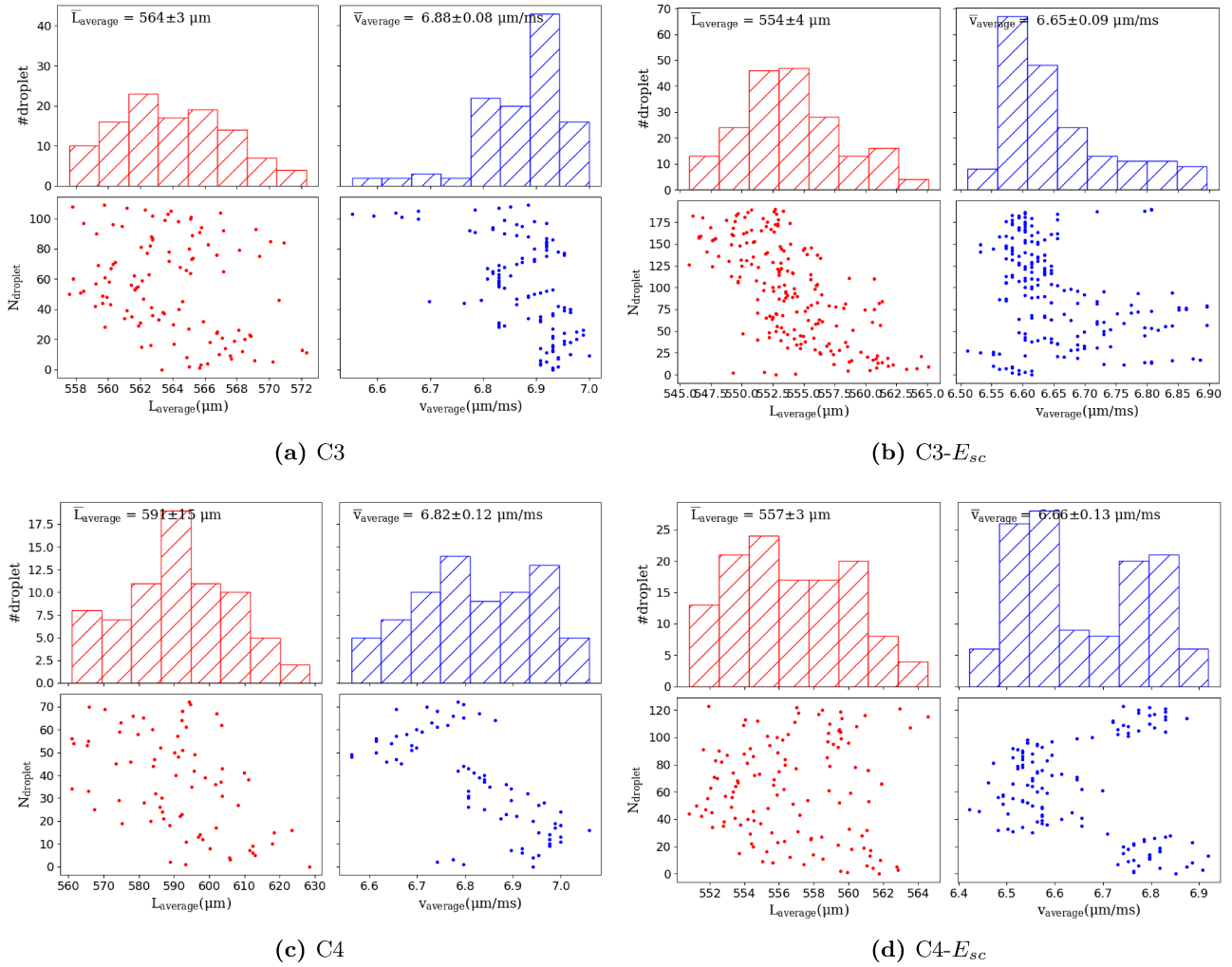

(a) C3

(b) C3-E_{sc}

(c) C4

(d) C4-E_{sc}

Figure 5.11: Plots of droplets' lengths and velocities measured for PS-617 nm solutions with concentration C3 (top) and C4 (bottom) in absence of E_{sc} (left) and after its establishment (right)

C (mg/g)	L (μm)	$L^{E_{sc}}$ (μm)	γ_L	v (μm/ms)	$v^{E_{sc}}$ (μm/ms)	γ_v
C3	564±3	554±4	2	6.88±0.08	6.65±0.09	1.9
C4	591±15	557±3	2.2	6.9±0.1	6.7±0.1	0.7

Table 5.4: Compatibilities γ_L and γ_v between the average droplets' length and velocity obtained without illumination and with illumination, after the establishment of the photo-induced field E_{sc}

The results reported in table 5.4 for C3 and C4 solutions show how E_{sc} seems to reduce the average droplet length without affecting too much the respective velocity when compared to the case without space-charge field. Moreover, both the average length obtained in the case of C3 and C4 with space-charge field are compatible with L_0 reported in table 5.3. Clearly, in the case of C4 solution the correspondent L without field is highly dispersed and reasonably overestimated, probably due to fluxes instabilities as can be seen from figure 5.11c. Regardless of the concentration considered, every droplets sequence of PS-617 nm particles previously investigated provided an average length $560 \leq L \leq 570$ μm. It is also interesting to note that in the case with the field, the two average lengths obtained for the two solutions are lower then $L(t = 45\text{min.})$ reported in fig. 5.10a.

This reduction effect induced by E_{sc} can be explained by taking into account the Pickering emulsion effect, introduced in section 3.3: the dielectric plastic microparticles, affected by the electric field, could be polarized and hence starting to behave as dipoles. The microparticles acquired electric moment would be directed towards the top glass cover, due to the presence of negative charges in the +z face of the iron-doped LN sample. As a consequence, it is reasonable to assume that the microspheres are attracted to the droplet interface (in the direction of the Fe:LN sample), as depicted in figure 3.9, acting as a surfactant and leading to a droplet length shrinking due to a reduction of the surface tension of the dispersed phase. Of course, further investigation is needed to better understand this observed dynamics.

As far as the normalized integral is concerned, figure 5.12 illustrates the behavior of the two I_N obtained with laser illumination of the cover (in the following: $I_N^{E_{sc}}$) compared to the correspondent I_N obtained with the same concentrations without field and reported in figure 3.5a.
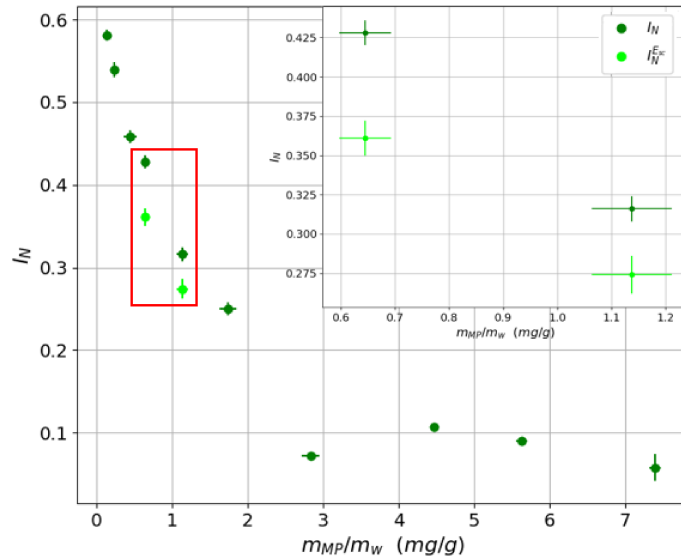

Figure 5.12: I_N integral points derived testing the solutions with E_{sc} (light green) compared with the ones of the same solutions obtained in the usual conditions (dark green).

C (mg/g)	I_N	$I_N^{E_{sc}}$	γ	ΔI_N (%)
C3	0.428±0.008	0.36±0.01	5.3	16±2 %
C4	0.316±0.008	0.27±0.01	3.6	15±3 %

Table 5.5: Values of the integrals plotted in figure 5.12, compatibilities and percentage difference with respect to I_N.

It is evident that the space-charge field affects the value of the normalized integral. The effects of E_{sc} are clearly visible in the graph but also when comparing the results in table 5.5: both $I_N^{E_{sc}}$ values are lower than the correspondent I_N ones and clearly not compatible. The variation is more remarkable in the case of C3 with a 16% decrease of the integral with respect to I_N. This could suggest that the lower the concentration of particles, the higher the influence of E_{sc} on the droplet content, at least in a certain range of concentrations. As a consequence, it would be reasonable that less diluted solutions partially screen the electric field reducing its effect on the normalized integral parameter.

Clearly, these hypothesis should be further investigated by, first of all, completing the PS-617nm $I_N^{E_{sc}}$ curve represented in figure 5.12 and then by analyzing microparticles with different diameters in order to examine the dependence of $I_N^{E_{sc}}$ on MP dimension, in particular in terms of screening of the field.

Conclusions

This thesis is the result of a preliminary study that aims at the investigation and development of new approaches for the identification of micrometer sized plastics, in order to overcome the limitations of the current technologies available, based on spectroscopic analysis (Raman spectroscopy, FTIR spectroscopy) or optical as well as scanning electron microscopy, which are suitable to track millimeter-sized plastics particles at most.

An optofluidic platform integrated in lithium niobate has been exploited to generate droplets containing microplastics. Each droplet was detected employing the optical stage integrated in the $LiNbO_3$ substrate and consisting of a Ti in-diffused optical waveguide in Mach-Zehnder interferometer (MZI) configuration. The passage of the droplet in front of the two MZI arms was monitored collecting an optical transmission (OT) signal. Such a signal is provided by the coupling of a $\lambda = 532\,nm$ laser beam with the optical guide, crossed orthogonally by the main channel of a microfluidic circuit, designed for the droplets formation, engraved in the same device with a cross-junction geometry.

PS-Research spherical particles with a nominal diameter of 340 nm, 617 nm, 1050 nm and 2500 nm have been diluted in MilliQ water, realizing solutions of different concentration. These aqueous mixtures, playing the role of dispersed phases, have been injected into the optofluidic device, with the purpose of exploiting the reproducibility of the correspondent droplets sequence flowing in the hexadecane continuous phase, to characterize and differentiate the solution content as a function of the concentration and dimension of the microparticles, by fixing the latter and the former respectively.

A presentation of the microfluidic regime and dynamic supporting the droplet generation, in addition to a description of the process followed for the optofluidic platform fabrication, introduced by briefly reviewing the literature concerning microchannels engraving and optical waveguides integration in LN, has been provided to explain the experimental conditions that have been used in this thesis.

We demonstrated the capability of the detector to recognize the presence of PS plastic particles, comparing the plateau of the signal produced by a single MilliQ droplet with the one related to a droplet containing microspheres. In order to optimize the device performance, a measurement and analysis protocol has been developed and here presented in Chapter 2. On the basis also of the results obtained from previous works carried out by the UNIPD group, the combination of fluxes Q_c=10 μL/min and Q_d=8 μL/min, corresponding to a ratio ϕ=0.8, has been selected as the reference one for all the acquisitions performed in this experimental activity. The normalized integral I_N, computed by averaging the areas delimited by the plateau and the two absolute minima characterizing the OT signal of each droplet belonging to a sequence, has been identified as the best estimator for the data analysis, especially in relation to its independence on the not permanent coupling of the laser to the MZI guide. This dimensionless quantity has been considered together with the m parameter which, instead, has been designed for the evaluation of the fluctuations affecting the droplet plateau and varying according to the concentration and dimension of the particles considered. The frequency content of the voltage oscillations defining such fluctuations was analyzed by computing their power spectrum. Given the difficulty to extract not ambiguous information from them, in appendix A qualitative results of the study of the power spectrum are summarised. As a perspective study, further investigations are required to dig on the dependence of the position of some peaks on the geometry as well as the dimension of the microparticles and, probably, on the material they are made of.

It is important to stress again that the results here derived are the consequence of a preliminary study, as innovative as ambitious. Both experimental and theoretical findings reported represent a very solid starting point for the definition of a protocol and, consequently, the realization of a device suitable

for the detection of micrometrical plastic particles. From the analysis of the behaviour of the integral I_N as a function of the particles' concentration, presented in chapter 3, it was found an interesting dependence on the ratio d/λ, where d is the diameter of the particles taken into account and λ the wavelength of the laser beam employed. In fact, both PS-340 nm and PS-2500 nm spheres, that have a fractional d/λ ratio, show a I_N plot characterized by an initial increase at the lower concentrations (below $\mathrm{m}_{PS}/\mathrm{m}_w < 1$ mg/g), followed by a decrease due to the prevalence of extinctions effects induced by higher $\mathrm{m}_{PS}/\mathrm{m}_w$ values and reducing the light transmitted. This trend is not reproduced by the PS-617 nm and PS-1050 nm microparticles, which have a diameter d approximately integer multiple of λ, since their signals generate just a decreasing I_N curve. This thesis showed that m and σ_m provide a useful tool since the analysis of the trends at varying the concentration pointed out an influence due to the particle diameter, rather than a dependence on d/λ. As a matter of fact, keeping separate the evaluation of the pair PS-340 nm and PS-2500 nm from the PS-617 nm and PS-1050 nm one, the particles with the higher diameter between the two considered display more intense fluctuations and a quicker stabilization. At the same concentration, in fact, m values follow a quicker increasing trend while σ_m distribution decreases more rapidly.

The influence of microplastics dimension is also crucial and some hypothetical models are proposed to fit the different I_N trends. An interesting approach based on Super-Poissonian fluctuations has been exploited to interpolate PS-617 nm and PS-1050 nm data. In the case of the PS-2500 nm spheres, instead, the introduction of a transmittance term to correct the fitting equation deduced by the just mentioned Super-Poissonian model was needed to describe the initial integral rise. Since the interaction of an electromagnetic wave with the PS-340 nm particles induces a different light extinction regime, the distribution of the normalized integrals associated with their solutions has been described by resorting to an approximation of the Lambert-Beer law. In this case, it was obtained by defining the scattering cross-section according to the Mie scattering formulation and expressing $\rho\sigma_{scat}$ as a function of c$=m_{PS}/m_w$. The fitting curves that have been tested reproduce the arrangement of all the I_N data, regardless of the type of particle examined.

The findings gradually derived have been finally explored in three different applications, presented in chapter 5. PMMA-2500 nm microparticles have been diluted in MilliQ solutions and employed as dispersed phases to test the capability of the optical device to identify plastics of a different material. Comparing the plateau of the signals produced by two single droplets containing PS-2500 nm and PMMA-2500 nm particles respectively, we found a clear difference in the intensity of fluctuations characterizing the OT signal collected. This is supposed to be related to an inhomogeneity in microplastics concentration affecting PMMA dispersed phase. The discrepancy between the two normalized integrals plots referred to PS and PMMA plastics respectively seems to suggest that, in the concentration range m_MP/m_w 2÷5 mg/g, our experimental setup is able to distinguish the two materials. Our results prove that the higher transparency of PMMA-microparticles, given the more light transmission provided by solutions including them, induced different optical response. The observed difference is visible in the same concentration range also in the m and σ_m distributions. Confirming the aforementioned considerations on the different voltage signal fluctuations, they show respectively a quicker increase and a quicker decrease of the PMMA values with respect to the PS ones.

The second application concerned the generation of a droplet sequence by flowing in the microfluidic circuit a dispersed phase realized by mixing the same quantity of PS-340 nm and PS-1050 nm solutions, both at concentration C=0.65 mg/g. The analysis of the results obtained from this test was essentially qualitative but it provides an interesting finding. In fact, by comparing the plateau produced by a droplet containing the mixture with the two describing a PS-340 nm and PS-1050 nm signal separately, it turned out that the voltage fluctuations due to the mixture are more similar to those induced by 1050 nm particles. The same evidence has been found by evaluating the three power spectra, since the arrangement of the peaks characterizing the frequency content of the mixture plateau oscillations seems to look more like the PS-1050 nm one.

Finally, the effects of a space charge electric field E_{sc}, induced by illuminating an iron-doped lithium niobate (Fe:LiNbO$_3$, Fe:LN) sample properly integrated in the same optofluidic platform, were investigated on two PS-617 nm solutions (C3 and C4). Although the field created seems to be weak, according to the elongation ΔL explored by MilliQ water droplets, a shrinking of the droplets' length in the pres-

ence of microplastics was noted for both the concentration of 617 nm particles employed. The action of E_{sc} was also visible on I_N. In fact, the normalized integrals describing the transmitted light of the two solutions with the illumination are lower than the correspondent obtained in absence of the field. The impact of the latter appears to be more intense for more diluted MP aqueous solutions, since C3 integral experienced a reduction higher than C4 one. In perspective, these hypotheses could be verified by implementing the current microfluidic stage with an additional external PDMS microchannel circuit, designed to generate subsequent dilutions of the dispersed phase initially introduced in the lithium niobate platform. In this configuration, the optical setup should detect a negative ΔL variation as long as the particles' concentration is so low to make the dispersed phase undistinguishable from pure water. From the theoretical point of view, to justify both the L contraction of microplastics-solution droplets due to E_{sc} and the length variability characterizing all the PS-droplet sequences, regardless of the diameter and concentration of the particles, we invoked the so called Pickering emulsion effect. Further measurements by including a surfactant in a MilliQ-dispersed phase could lead to interesting results since it would produce, acting on the surface tension at the water-hexadecane interface, the stabilizing effect which is supposed to be realized by the plastic solid particles.

To conclude, the optofluidic platform employed in this thesis project proved to be really effective in the detection of microplastics. As a matter of fact, the flowing of a droplets sequence containing any of the PS spheres types available provides, in terms of an optical signal, a fingerprint of its passage, showing to be distinguishable from a MilliQ water droplet signal in a not ambiguous way. The device has demonstrated, by means of the estimator I_N, to be able to identify different particles' concentrations as well as to make visible, as a function of the latter, the dependence of I_N on the diameter of the spheres employed. Last but not least, the results derived from PMMA microplastics, even though preliminary, allow the author to be confident that the detector has also the capability, in a specific concentration range at least, to distinguish diverse plastic materials.

In perspective, the employment of plastic microparticles of different materials and dimensions, in addition to realizing the optical trigger by coupling the MZI waveguide to a laser with a different wavelength, could pave the way for future improvements of the exploited opto-fluidic configuration in microplastics identification and quantification.

Power spectra qualitative analysis

In this section, some results of the qualitative analysis of the frequency spectrum of the signal fast fluctuations observed in microplastics in water droplets are presented. As already shown in Sec. 2.1 (Fig. 2.6), the signal corresponding to the central part of the droplet presents fast amplitude variations when microplastics are added in water and instead a smooth plateau in pure water droplets. These features are extremely reproducible and cannot therefore be attributed to experimental artifacts.

In particular, the focus of this section will be on the two main dependencies that affect the structure of a power spectrum, fixing either the diameter of the particles or the concentration of the solution or both. These dependencies are:

- dependence on the water base signal employed to extract the FT and the associated power spectrum describing the frequency behavior of the PS particles contained in the solution;

- dependence on the different concentrations m_{PS}/m_w considered for the same particles' diameter.

A.1 Water base signal dependence

(a) Power spectra 50th droplet

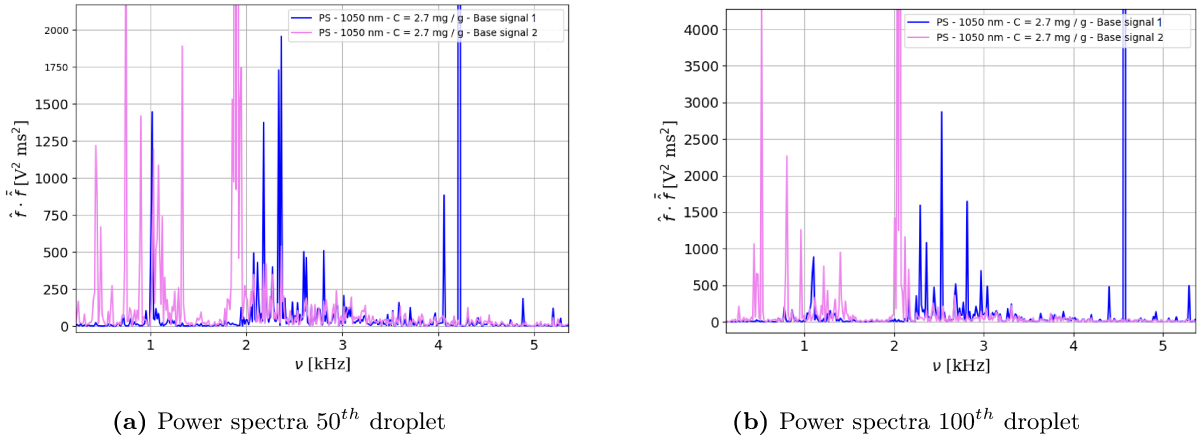**(b)** Power spectra 100th droplet

Figure A.1: Figure A.1a represents two power spectra that have been calculated with two different water base signals; they describe the frequency content of the same signal, the one produced by the 50th droplet of a sequence of droplets containing PS-1050 nm spheres with a concentration C=2.7 mg/g. The same two water signals have been employed to derive the power spectra of the 100th droplet, reported in figure A.1b

To show the dependence on the water base signal $\widehat{V}_{avg,\,w}(\nu_j)$, in figure A.1 a comparison between two energy spectral densities computed exploiting two different water signals, acquired in two different

days, is represented. Both have been obtained by analyzing the signal generated by a sequence of 107 droplets containing PS-1050 nm with a concentration of C=2.7 mg/g.

Figure A.1a illustrates the superposition of the power spectra describing the frequency content of the 50th droplet of the sequence sampled. It is visible the different structures of the peaks, both in intensity and frequency.

Moreover, observing figure A.1b, it is noticeable how the two $\bar{S}_{i=100}(\nu)_P$, referred to the 100th droplet, show an arrangement of peaks pretty similar to the correspondent $\bar{S}_{i=50}(\nu)_P$ obtained with the same base of water. However, it is complicated to find out a precise correspondence between the peaks since they not only have different intensities but also, in some cases, completely different frequencies.
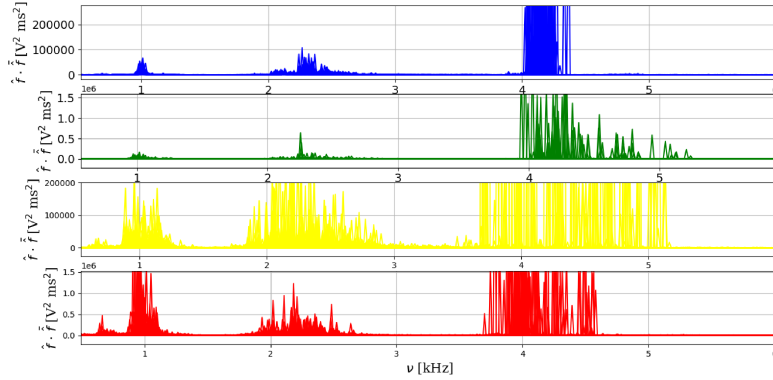
(a) Same water base signal
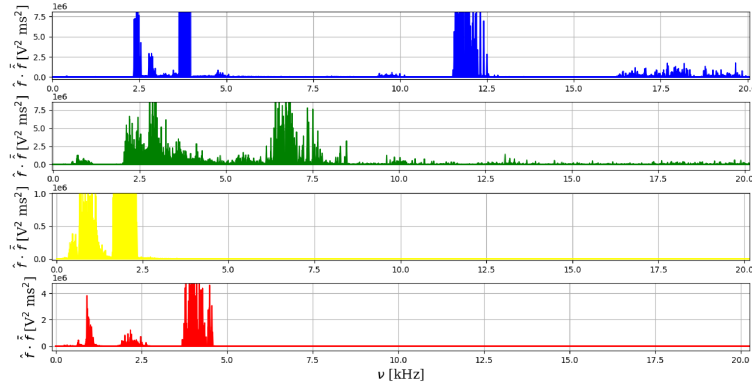
(b) Different water base signals

Figure A.2: Figure A.2a shows the power spectra derived from the PS-340 nm (in blue), PS-617 nm (in green), PS-1050 nm (in yellow) and PS-2500 nm (in red) particles' signals $V(t)$; they have been computed exploiting the same water base signal. Figure A.2b, instead, illustrates the same power spectra but obtained with a different water base for each of them.

To further investigate this water-base dependence, the power spectrum of each of the PS particles available has been taken into account. In particular, figure A.2a shows the four complete energy spectral density $\bar{S}(\nu)_P = \{\bar{S}_i(\nu)_P\}_{i=0}^{n}$, restricted at the lower values of the frequency domain, computed for the PS-340 nm (in blue), PS-617 nm (in green), PS-1050 nm (in yellow) and PS-2500 nm (in red) spheres, exploiting the voltage signal produced separately by each type of particle and the same water base signal.

Since these results have been derived by fixing the concentration, it is interesting to note that the shape of each spectrum presents some common features regardless of the particles' diameter, such as three well-distinguishable groups of peaks, arranged in the frequency domain considered. At first sight, this experimental observation would suggest a dependence of the spectrum either on the material or on the geometry - spherical in this case - of the microplastics. The microplastlcs size, instead, seems

to affect the intensity and the dispersion of the peaks.

In order to verify if it were the case, we repeated the same data analysis using a different water signal as reference, and results are summarised in figure A.2b, where the same power spectra aforementioned have been in this situation derived employing a different base signal for each PS-spheres considered. It is evident that both position and intensity of the peaks vary when comparing each spectrum illustrated in figure A.2b with the correspondent one reported in figure A.2a. Data Analysis of PS-2500 nm is the same in both figures because referred to the same water base.

All observations considered, it is possible to note how strong the dependence of the spectral content on the water signal used to evaluate it is. In particular, the latter seems to mostly affect the frequency position of the group of peaks (the third) distributed at the highest frequencies in the domain considered, which is difficult to identify both in the PS-617 nm and PS-340 nm spectrum and even absent in that of the PS-1050 nm particles, represented in figure A.2b.

By observing these eight power spectra, only the group of peaks located around 2.5 kHz - since also the one at the lowest frequencies is absent or translated by varying the water base - seems to remain stable, suggesting again a possible relation with the material or the geometry of the microplastics contained in the droplets.

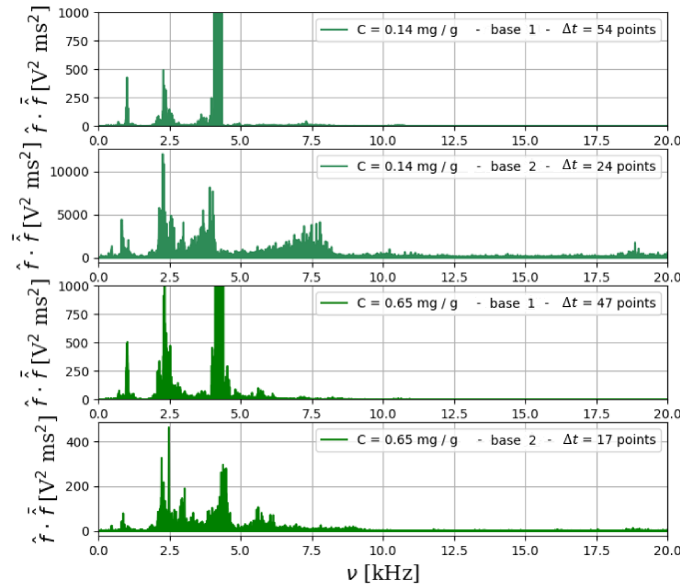## A.2   Concentration $\boldsymbol{m_{PS}/m_w}$ dependence

Figure A.3: Power spectra describing the fluctuations introduced by the PS-617 nm particles evaluated in different conditions: the first pair of graphs (in dark green) provides information on the concentration C=0.14 mg/g, while the second one (in light green) is referred to C=0.65 mg/g. Two different water base signals, identified as *base* 1 and *base* 2, have been exploited to realize these energy spectral densities: the former is associated to the first and third $\bar{S}(\nu)_P$, the latter to the second and fourth ones. Δt indicates the difference in points between the water signal $V_{avg,w}(t)$ and the signal $V_{avg}(t)$.

To analyze the dependence of plastic energy spectral density $\bar{S}(\nu)_P$ on the concentration of spheres in the solution, figure A.3 is used. Here, the four power spectra represented are all referred to signals generated by PS-617 nm particles.

It is worth noting how the spectra associated to the same concentration[1] are very similar in the shape and the arrangement of the peaks, even though computed with two different base water signals. In fact, if we express the difference in time length in each graph in terms of points (1 ms=50 points), and we consider the water signal $V_{avg,w}(t)$ and the signal $V_{avg}(t)$ as the point-by-point average of each

---

[1]considering thus the first pair of graphs separately from the second one

droplet-with-plastic signal acquired, it results that the time length is $\Delta t \sim 1\text{ms}$ and the dependence of power spectrum on $V_{avg,w}$ is attenuated.

Comparing then the first graph with the third, and the second with the fourth, we can evaluate instead the frequency content brought by the PS-617 nm particles at different concentrations but for the same water base employed. It emerges that the group of peaks centered around 7.5 kHz (in the first power spectra its intensity is very low) seems to move towards lower frequencies the higher is the concentration taken into account. On the contrary, the first two major peaks, those located around 1.25 kHZ and 2.5 kHz, maintain a pretty stable position. In particular, the latter looks like to be a constant in the power spectra, since it is present by varying both the particles' diameter and concentration, and the water base adopted as well. This finding encourages its possible dependence either on the material or on a shape factor, as already discussed in section A.1.

Bibliography

[1] Plasticseurope. Plastics - the facts 2022, 2022. `https://plasticseurope.org/wp-content/uploads/2022/10/PE-PLASTICS-THE-FACTS_V7-Tue_19-10-1.pdf`.

[2] Walter Leal Filho, Julian Hunt, and Marina Kovaleva. Garbage patches and their environmental implications in a plastisphere. *Journal of Marine Science and Engineering*, 9(11):1289, 2021.

[3] Ahmet H Iri, Malek HA Shahrah, Ali M Ali, Sayed A Qadri, Talha Erdem, Ibrahim T Ozdur, and Kutay Icoz. Optical detection of microplastics in water. *Environmental Science and Pollution Research*, pages 1–7, 2021.

[4] Baljit Singh and Nisha Sharma. Mechanistic implications of plastic degradation. *Polymer degradation and stability*, 93(3):561–584, 2008.

[5] Julien Boucher and Damien Friot. *Primary microplastics in the oceans: a global evaluation of sources*, volume 10. Iucn Gland, Switzerland, 2017.

[6] PJ Kershaw and CM Rochman. Sources, fate and effects of microplastics in the marine environment: part 2 of a global assessment. *Reports and Studies-IMO/FAO/Unesco-IOC/WMO/IAEA/UN/UNEP Joint Group of Experts on the Scientific Aspects of Marine Environmental Protection (GESAMP) Eng No. 93*, 2015.

[7] HORIBA Scientific. Microplasitcs - second edition. `https://www.horiba.com/int/scientific/applications/environment/pages/microplastics/?utm_source=uhw&utm_medium=301&utm_campaign=uhw-redirect`.

[8] Dounia Elkhatib and Vinka Oyanedel-Craver. A critical review of extraction and identification methods of microplastics in wastewater and drinking water. *Environmental Science & Technology*, 54(12):7037–7049, 2020.

[9] Joana Correia Prata, João P da Costa, Isabel Lopes, Armando C Duarte, and Teresa Rocha-Santos. Environmental exposure to microplastics: An overview on possible human health effects. *Science of the total environment*, 702:134455, 2020.

[10] Luís Fernando Amato-Lourenço, Regiani Carvalho-Oliveira, Gabriel Ribeiro Júnior, Luciana dos Santos Galvão, Rômulo Augusto Ando, and Thais Mauad. Presence of airborne microplastics in human lung tissue. *Journal of Hazardous Materials*, 416:126124, 2021.

[11] Fernando Barbosa, Joseph A Adeyemi, Mariana Zuccherato Bocato, Ahmed Comas, and Andres Campiglia. A critical viewpoint on current issues, limitations, and future research needs on micro-and nanoplastic studies: From the detection to the toxicological assessment. *Environmental Research*, 182:109089, 2020.

[12] Kai Zhao, Yunman Wei, Jianhong Dong, Penglu Zhao, Yuezhu Wang, Xinxiang Pan, and Junsheng Wang. Separation and characterization of microplastic and nanoplastic particles in marine environment. *Environmental Pollution*, page 118773, 2021.

[13] Natalia P Ivleva, Alexandra C Wiesheu, and Reinhard Niessner. Microplastic in aquatic ecosystems. *Angewandte Chemie International Edition*, 56(7):1720–1739, 2017.

[14] Simone Marchetti. Light based sensing di microplastiche disperse in soluzioni acquose.

[15] Giovanni Bragato. Study of light-driven phenomena for opto-microfluidic sensing on multifunctional lithium niobate platforms. 2021.

[16] Michele Zanaradi. Fenomeni foto-indotti su gocce generate in piattaforme opto-microfluidiche.

[17] Patrick Tabeling. *Introduction to microfluidics*. Oxford University Press on Demand, 2005.

[18] Nam-Trung Nguyen, Steven T Wereley, and Seyed Ali Mousavi Shaegh. *Fundamentals and applications of microfluidics*. Artech house, 2019.

[19] George M Whitesides. The origins and the future of microfluidics. *nature*, 442(7101):368–373, 2006.

[20] Hamed Amini, Wonhee Lee, and Dino Di Carlo. Inertial microfluidic physics. *Lab on a Chip*, 14(15):2739–2761, 2014.

[21] Pijush K Kundu, Ira M Cohen, and David R Dowling. *Fluid mechanics*. Academic press, 2015.

[22] Xavier Casadevall i Solvas and Andrew DeMello. Droplet microfluidics: recent developments and future applications. *Chemical Communications*, 47(7):1936–1942, 2011.

[23] Pingan Zhu and Liqiu Wang. Passive and active droplet generation with microfluidics: a review. *Lab on a Chip*, 17(1):34–75, 2017.

[24] Carlo Montevecchi. Integrated opto-microfluidic lab-on-a-chip in lithium niobate for sensing applications. 2016.

[25] Piotr Garstecki, Michael J Fuerstman, Howard A Stone, and George M Whitesides. Formation of droplets and bubbles in a microfluidic t-junction—scaling and mechanism of break-up. *Lab on a Chip*, 6(3):437–446, 2006.

[26] Todd Thorsen, Richard W Roberts, Frances H Arnold, and Stephen R Quake. Dynamic pattern formation in a vesicle-generating microfluidic device. *Physical review letters*, 86(18):4163, 2001.

[27] Gordon F Christopher, N Nadia Noharuddin, Joshua A Taylor, and Shelley L Anna. Experimental observations of the squeezing-to-dripping transition in t-shaped microfluidic junctions. *Physical review E*, 78(3):036317, 2008.

[28] Howard A Stone. On lubrication flows in geometries with zero local curvature. *Chemical engineering science*, 60(17):4838–4845, 2005.

[29] G Bettella, Riccardo Zamboni, G Pozza, A Zaltron, C Montevecchi, M Pierno, G Mistura, C Sada, L Gauthier-Manuel, and Mathieu Chauvet. Linbo3 integrated system for opto-microfluidic sensing. *Sensors and Actuators B: Chemical*, 282:391–398, 2019.

[30] Annamaria Zaltron, Giacomo Bettella, Gianluca Pozza, R Zamboni, M Ciampolillo, N Argiolas, C Sada, Sebastian Kroesen, Michael Esseling, and Cornelia Denz. Integrated optics on lithium niobate for sensing applications. In *Optical Sensors 2015*, volume 9506, pages 50–59. SPIE, 2015.

[31] Tatyana Volk and Manfred Wöhlecke. *Lithium niobate: defects, photorefraction and ferroelectric switching*, volume 115. Springer Science & Business Media, 2008.

[32] Ed L Wooten, Karl M Kissa, Alfredo Yi-Yan, Edmond J Murphy, Donald A Lafaw, Peter F Hallemeier, David Maack, Daniel V Attanasio, Daniel J Fritz, Gregory J McBrien, et al. A review of lithium niobate modulators for fiber-optic communications systems. *IEEE Journal of selected topics in Quantum Electronics*, 6(1):69–82, 2000.

[33] Olivier Alibart, Virginia D'Auria, Marc De Micheli, Florent Doutre, Florian Kaiser, Laurent Labonté, Tommaso Lunghi, Éric Picholle, and Sébastien Tanzilli. Quantum photonics at telecom wavelengths based on lithium niobate waveguides. *Journal of Optics*, 18(10):104001, 2016.

[34] Luis Arizmendi. Photonic applications of lithium niobate crystals. *physica status solidi (a)*, 201(2):253–283, 2004.

[35] RS Weis and TK Gaylord. Lithium niobate: Summary of physical properties and crystal structure. *Applied Physics A*, 37:191–203, 1985.

[36] Chihiro Koyama, Jun Nozawa, Kozo Fujiwara, and Satoshi Uda. Effect of point defects on curie temperature of lithium niobate. *Journal of the American Ceramic Society*, 100(3):1118–1124, 2017.

[37] M Wöhlecke, G Corradi, and K Betzler. Optical methods to characterise the composition and homogeneity of lithium niobate single crystals. *Applied physics B*, 63:323–330, 1996.

[38] AM Glass, D Von der Linde, and TJ Negran. High-voltage bulk photovoltaic effect and the photorefractive process in linbo3. *Applied Physics Letters*, 25(4):233–235, 1974.

[39] Giacomo Bettella. Integrated opto-microfluidic lab-on-a-chip in lithium niobate for droplet generation and sensing. *PhD thesis, PhD School of Physics, University of Padova*, 2021.

[40] Hong Ma, AK-Y Jen, and Larry R Dalton. Polymer-based optical waveguides: materials, processing, and devices. *Advanced materials*, 14(19):1339–1365, 2002.

[41] H Kogelnik. Theory of optical waveguides. *Guided-wave optoelectronics*, pages 7–88, 1988.

[42] Marco Bazzan and Cinzia Sada. Optical waveguides in lithium niobate: Recent developments and applications. *Applied Physics Reviews*, 2(4):040603, 2015.

[43] Ovidio Peña-Rodríguez, José Olivares, Mercedes Carrascosa, Ángel García-Cabañes, Antonio Rivera, and Fernando Agulló-López. *Optical waveguides fabricated by ion implantation/irradiation: A review*. InTech Rijeka, Croatia, 2012.

[44] Jonas Burghoff, Christian Grebing, Stefan Nolte, and Andreas Tünnermann. Waveguides in lithium niobate fabricated by focused ultrashort laser pulses. *Applied surface science*, 253(19):7899–7902, 2007.

[45] Riccardo Zamboni. *Study of light driven phenomena for optofluidic applications in Lab-on-a-chip platforms in lithium niobate*. PhD thesis, Tesi di dottorato, Universita degli studi di Padova, Padova (XXXII ciclo), 2019.

[46] Masaharu Fukuma, Juichi Noda, and Hiroshi Iwasaki. Optical properties in titanium-diffused linbo3 strip waveguides. *Journal of Applied Physics*, 49(7):3693–3698, 1978.

[47] F Caccavale, C Sada, F Segato, and F Cavuoti. Secondary ion mass spectrometry and optical characterization of ti: Linbo3 optical waveguides. *Applied surface science*, 150(1-4):195–201, 1999.

[48] G Singh, RP Yadav, and V Janyani. Ti indiffused lithium niobate (ti: Linbo3) mach-zehnder interferometer all optical switches: a review. *New Advanced Technologies*, 2010.

[49] Riccardo Zamboni. Optofluidic application of a mach-zehnder interferometer integrated in lithium niobate for droplet sensing. 2016.

[50] Shashi Prakash and Subrata Kumar. Fabrication of microchannels: a review. *Proceedings of the Institution of Mechanical Engineers, Part B: Journal of Engineering Manufacture*, 229(8):1273–1288, 2015.

[51] Gwenn Ulliac, V Calero, Abdoulaye Ndao, FI Baida, and M-P Bernal. Argon plasma inductively coupled plasma reactive ion etching study for smooth sidewall thin film lithium niobate waveguide application. *Optical Materials*, 53:1–5, 2016.

[52] Masashi Tamura and Shinzo Yoshikado. Etching characteristics of linbo3 crystal by fluorine gas plasma reactive ion etching. *Surface and Coatings Technology*, 169:203–207, 2003.

[53] Manoj Sridhar, Devendra K Maurya, James R Friend, and Leslie Y Yeo. Focused ion beam milling of microchannels in lithium niobate. *Biomicrofluidics*, 6(1):012819, 2012.

[54] Minni Qu, Yunliang Shen, Liying Wu, Xuecheng Fu, Xiulan Cheng, and Ying Wang. Homogenous and ultra-shallow lithium niobate etching by focused ion beam. *Precision Engineering*, 62:10–15, 2020.

[55] Giacomo Bettella, Gianluca Pozza, Sebastian Kroesen, Riccardo Zamboni, Enrico Baggio, Carlo Montevecchi, Annamaria Zaltron, Ludovic Gauthier-Manuel, Giampaolo Mistura, Claudio Furlan, et al. Lithium niobate micromachining for the fabrication of microfluidic droplet generators. *Micromachines*, 8(6):185, 2017.

[56] Jintian Lin, Yingxin Xu, Zhiwei Fang, Min Wang, Jiangxin Song, Nengwen Wang, Lingling Qiao, Wei Fang, and Ya Cheng. Fabrication of high-q lithium niobate microresonators using femtosecond laser micromachining. *Scientific reports*, 5(1):8072, 2015.

[57] Sean M Langelier, Leslie Y Yeo, and James Friend. Uv epoxy bonding for enhanced saw transmission and microscale acoustofluidic integration. *Lab on a Chip*, 12(16):2970–2976, 2012.

[58] Gordon F Christopher and Shelly L Anna. Microfluidic methods for generating continuous droplet streams. *Journal of Physics D: Applied Physics*, 40(19):R319, 2007.

[59] Jonathan Bennès, Sylvain Ballandras, and Frederic Cherioux. Easy and versatile functionalization of lithium niobate wafers by hydrophobic trichlorosilanes. *Applied Surface Science*, 255(5):1796–1800, 2008.

[60] Touraj Manifar, Asad Rezaee, Mehdi Sheikhzadeh, and Silvia Mittler. Formation of uniform self-assembly monolayers by choosing the right solvent: Ots on silicon wafer, a case study. *Applied Surface Science*, 254(15):4611–4619, 2008.

[61] Mark E McGovern, Krishna MR Kallury, and Michael Thompson. Role of solvent on the silanization of glass with octadecyltrichlorosilane. *Langmuir*, 10(10):3607–3614, 1994.

[62] Leonardo Zanini. Phd thesis. For more information: leonardo.zanini.2@phd.unipd.it.

[63] Giovanni Bragato. Velocimetro per gocce microfluidiche basato su di un interferometro fotonico integrato in niobato di litio.

[64] Leonardo Zanini. Droplet-induced optical effects in an opto-microfluidic cross-configuration system. For more information: leonardo.zanini.2@phd.unipd.it.

[65] M De Menech, Piotr Garstecki, F Jousse, and Howard A Stone. Transition from squeezing to dripping in a microfluidic t-shaped junction. *journal of fluid mechanics*, 595:141–161, 2008.

[66] S Arias and A Montlaur. Numerical and experimental study of the squeezing-to-dripping transition in a t-junction. *Microgravity Science and Technology*, 32(4):687–697, 2020.

[67] James H McClellan, Ronald W Schafer, and Mark A Yoder. *Dsp first*. Pearson Education, 2017.

[68] David W Hahn. Light scattering theory. *Department of Mechanical and Aerospace Engineering, University of Florida*, 2009.

[69] Milton Kerker. *The scattering of light and other electromagnetic radiation*. Elsevier, 2016.

[70] Craig F Bohren and Donald R Huffman. *Absorption and scattering of light by small particles.* John Wiley & Sons, 2008.

[71] R Alferness, V Ramaswamy, S Korotky, M Divino, and L Buhl. Efficient single-mode fiber to titanium diffused lithium niobate waveguide coupling for λ= 1.32 μm. *IEEE Journal of Quantum Electronics*, 18(10):1807–1813, 1982.

[72] E Murphy, T Rice, Leon McCaughan, G Harvey, and P Read. Permanent attachment of single-mode fiber arrays to waveguides. *Journal of lightwave technology*, 3(4):795–799, 1985.

[73] Jie Wu and Guang-Hui Ma. Recent studies of pickering emulsions: particles make the difference. *Small*, 12(34):4633–4648, 2016.

[74] Bernard P Binks and Tommy S Horozov. *Colloidal particles at liquid interfaces.* Cambridge University Press, 2006.

[75] Marie Wahlgren, Johan Engblom, Malin Sjoo, and Marilyn Rayner. The use of micro-and nanoparticles in the stabilisation of pickering-type emulsions for topical delivery. *Current pharmaceutical biotechnology*, 14(15):1222–1234, 2013.

[76] Bastien Arnal, Camilo Perez, Chen-Wei Wei, Jinjun Xia, Michael Lombardo, Ivan Pelivanov, Thomas J Matula, Lilo D Pozzo, and Matthew O'Donnell. Sono-photoacoustic imaging of gold nanoemulsions: Part i. exposure thresholds. *Photoacoustics*, 3(1):3–10, 2015.

[77] Marilyn Rayner, Diana Marku, Madeleine Eriksson, Malin Sjöö, Petr Dejmek, and Marie Wahlgren. Biomass-based particles for the formulation of pickering type emulsions in food and topical applications. *Colloids and Surfaces A: Physicochemical and Engineering Aspects*, 458:48–62, 2014.

[78] BP Binks and SO Lumsdon. Pickering emulsions stabilized by monodisperse latex particles: effects of particle size. *Langmuir*, 17(15):4540–4547, 2001.

[79] Alexander B Kostinski. On the extinction of radiation by a homogeneous but spatially correlated random medium. *JOSA A*, 18(8):1929–1933, 2001.

[80] J. W. Goodman. *Statistical Optics.* Wiley, New York., 1985.

[81] A. Burshtein. *Introduction to Thermodynamics and Kinetic Theory of Matter.* Wiley, New York, 1995.

[82] Ralph Budwig. Refractive index matching methods for liquid flow investigations. *Experiments in fluids*, 17(5):350–355, 1994.

[83] Rita Scolaro. Studio dei fenomeni di intrappolamento di sistemi microscopici indotti dalla luce in cristalli di niobato di litio.